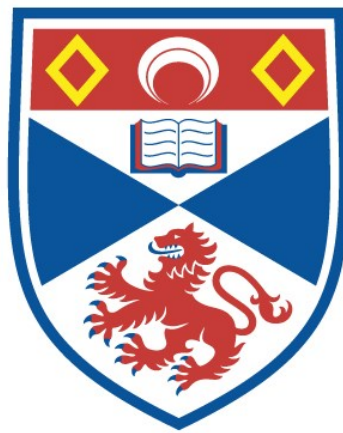# INTERPLAY OF SPIN-ORBIT COUPLING AND CRYSTAL SYMMETRIES IN THE ELECTRONIC STRUCTURES OF NbGeSb AND $Ca_3Ru_2O_7$

Igor Marković

A Thesis Submitted for the Degree of PhD
at the
University of St Andrews

2020

Interplay of spin-orbit coupling and crystal symmetries in the electronic structures of $NbGeSb$ and $Ca_3Ru_2O_7$

Igor Marković

University of
St Andrews

This thesis is submitted in partial fulfillment for the degree of
Doctor of Philosophy (PhD) at the University of St Andrews

April, 2020

| Declarations

Candidate's declaration

I, Igor Marković, do hereby certify that this thesis, submitted for the degree of PhD, which is approximately 34,000 words in length, has been written by me, and that it is the record of work carried out by me, or principally by myself in collaboration with others as acknowledged, and that it has not been submitted in any previous application for any degree.
I was admitted as a research student at the University of St Andrews in May 2016.
I received funding from an organisation or institution and have acknowledged the funder(s) in the full text of my thesis.

Date: 12.05.2020   Signature of candidate:

Supervisor's declaration

I hereby certify that the candidate has fulfilled the conditions of the Resolution and Regulations appropriate for the degree of PhD in the University of St Andrews and that the candidate is qualified to submit this thesis in application for that degree.

Date: 12.05.2020   Signature of supervisor:

Date: 12.05.2020   Signature of supervisor:

Permission for publication

In submitting this thesis to the University of St Andrews we understand that we are giving permission for it to be made available for use in accordance with the regulations of the University Library for the time being in force, subject to any copyright vested in the work not being affected thereby. We also understand, unless exempt by an award of an embargo as requested below, that the title and the abstract will be published, and that a copy of the work may be made and supplied to any bona fide library or research worker, that this thesis will be electronically accessible for personal or research use and that the library has the right to migrate this thesis into new electronic forms as required to ensure continued access to the thesis.

I, Igor Marković, confirm that my thesis does not contain any third-party material that requires copyright clearance.

The following is an agreed request by candidate and supervisor regarding the publication of this thesis:

Printed copy

Embargo on all of **print** copy for a period of 2 years on the following ground(s):
- Publication would preclude future publication

Supporting statement for printed embargo request

My thesis contains research which is yet to be published in a peer-review journal.

Electronic copy

Embargo on all of **electronic** copy for a period of 2 years on the following ground(s):
- Publication would preclude future publication

Supporting statement for printed embargo request

My thesis contains research which is yet to be published in a peer-review journal.

Title and Abstract

- I agree to the title and abstract being published.

Date: 12.05.2020   Signature of candidate:

Date: 12.05.2020   Signature of supervisor:

Date: 12.05.2020   Signature of supervisor:

Underpinning Research Data or Digital Outputs

Candidate's declaration

I, Igor Marković, understand that by declaring that I have original research data or digital outputs, I should make every effort in meeting the University's and research funders' requirements on the deposit and sharing of research data or research digital outputs.

Date: 12.05.2020   Signature of candidate:

Permission for publication of underpinning research data or digital outputs

We understand that for any original research data or digital outputs which are deposited, we are giving permission for them to be made available for use in accordance with the requirements of the University and research funders, for the time being in force.

We also understand that the title and the description will be published, and that the underpinning research data or digital outputs will be electronically accessible for use in accordance with the license specified at the point of deposit, unless exempt by award of an embargo as requested below.

The following is an agreed request by candidate and supervisor regarding the publication of underpinning research data or digital outputs:

Embargo on all of electronic files for a period of 2 years on the following ground(s):
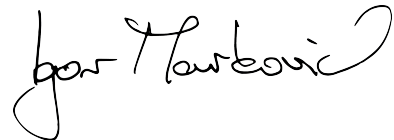- Publication would preclude future publication

Supporting statement for printed embargo request

My thesis contains research which is yet to be published in a peer-review journal.

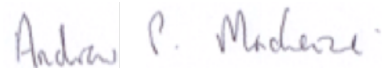Date: 12.05.2020   Signature of candidate:

Date: 12.05.2020   Signature of supervisor:

Date: 12.05.2020   Signature of supervisor:

Abstract

This thesis presents the study of electronic structure of two materials with strong spin-orbit coupling using angle-resolved photoemission spectroscopy (ARPES) experiments and density-functional theory (DFT) band calculations. The two materials are NbGeSb and $Ca_3Ru_2O_7$, which host weak and strong electronic interactions, respectively. While at first glance they seem rather disparate, I will show in both cases how novel phenomena emerge from the interplay of spin-orbit coupling and the crystal symmetries.

In NbGeSb, I combine insights from spin-integrated and spin-resolved ARPES measurements with DFT slab calculations to reveal how band inversion of two pairs of spin-orbit coupled surface states along the edge of the Brillouin zone results in a peculiar crossing structure with two protected and two asymmetrically gapped crossing points. I show how this is caused by the presence of a mirror symmetry line assigning definite mirror parity to orbital and spin angular momentum of the bands. This leads to a low-energy description of the crossing points equivalent to a two-dimensional Weyl equation, establishing them as 2D analogues of Weyl points.

In $Ca_3Ru_2O_7$, on the other hand, spin-orbit coupling provides a link between the electronic structure, the underlying antiferromagnetic order and the inherent antipolar distortion in the crystal structure. Our results reveal that a known structural and spin reorientation transition is caused by a spin-orbit derived gapping of a large Fermi surface. The hybridisation term couples the magnetic moment direction with the antipolar distortion of the crystal structure, and is only unlocked when the resulting electronic energy gain becomes enough to overcome the cost of spin reorientations.

These findings together highlight the abundance of possibilities for novel phenomena arising from the interplay of spin-orbit coupling and crystal symmetries in quantum materials.

| Acknowledgements

The research presented in this thesis was performed in the course of my doctoral studies which were shared between the University of St Andrews, where I have spent most of my time, and the Max Planck Institute for Chemical Physics of Solids in Dresden. It is highly collaborative in nature, and I have benefited from the help and insights of colleagues and collaborators both internal and external, whom I would like to acknowledge here.

First and foremost, I need to thank my two supervisors, Phil King and Andy Mackenzie. Their guidance and support has been invaluable over the past years, and the many discussions I have had with them have been both a great source of both knowledge and fun.

The particular, team nature in which we conduct synchrotron-based ARPES experiments means that there are many members of the King group with whom I have spend many days and nights on beamtime shifts, collecting the measurements for these, but also many other projects: Oliver Clark, Federico Mazzola, Matthew Watson, Veronika Sunko, Jonathan Riley, Lewis Bawden, Edgar Abarca Morales, Klara Volckaert, Kaycee Underwood. I owe thanks particularly to Oliver, Federico, Lewis and Matt who, alongside Phil, have introduced me to the field of angle-resolved photoemission and taught me the nuts and bolts of performing the experiments.

Aside from our own team, I would like to acknowledge the beamline scientists who maintain and help with the experiments at all the facilities where these measurements were performed: François Bertran and Patrick Le Fèvre at the Soleil synchrotron, Timur Kim, Pavel Dudin and Céphise Cacho at the Diamond Light Source synchrotron, Craig Polley and Thiagarajan Balasubramanian at the Max IV synchrotron, Ivana Vobornik and Jun Fujii at the Elettra synchrotron, Taichi Okuda at HiSOR synchrotron and Ming Shi at the Swiss Light Source synchrotron.

Of course, none of the experiments would have been possible without the high-quality single crystals made by our collaborators working in synthesis. The samples I used were made and kindly provided by Jonathan Alaria and his student Keiron Murphy from the University of Liverpool, and Dmitry Sokolov from the MPI CPfS in Dresden.

Even though this thesis is based mainly on experimental work, the understanding and results I present also come from theoretical calculations and modeling. This primarily refers to *ab initio* calculations using density-functional theory, for which I must thank Matthew Dyer and his student Phil Murgatroyd from the University of Liverpool, and Helge Rosner from the MPI CPfS in Dresden for their patience with my requests for ever more detailed calculations. I also have to mention Matt Watson here again, who has introduced me to DFT, and helped me start doing my own calculations which ended up featuring heavily in the thesis. Special thanks goes to Chris Hooley, who has done most of the tight-binding modelling, but also much more than that. Discussions with him have been a constant source of advice and understanding and good fun throughout my PhD.

Along with the work presented in this thesis, I have also worked on several other projects which sadly did not yield results which would merit being included in the thesis. However, I would still like to acknowledge people who have helped me with two of those projects which are particularly worth mentioning. First is the growth of thin films of complex oxides using molecular-beam epitaxy in St Andrews, on which I have worked closely with Gordon Kentish and Martin McLaren, and later, Yoshiko Nanao. Martin, the lab technician, whose understanding of all the ins and outs of the lab systems and his friendly nature make him an indispensible part of the group, deserves a particular mention here. Second is my three-month visit to the University of Kyoto as part of the Topological Materials Science Junior Research Exchange Program, where I worked on single crystal growth of antiperovskite oxide materials in the group of Yoshiteru Maeno. I am very greatful for the kind welcome I was shown in Kyoto by the members of the group, in particular to Mohamed Oudah who was a great help both with the scientific and the social aspects of living in Japan.

In the end, I want to thank people from the St Andrews physics department whom I have not mentioned yet above, but whose friendship and personal support have meant the world throughout these past few years: Stephanie Matern, Philippa McGuinness, Rhea Stewart, Maja Bachman, and many others...

Finally, I would like to acknowledge the financial support of the International Max Planck Research School for Chemistry and Physics of Quantum Materials, and the University of St Andrews.

| Publications

○ The work presented in this thesis has resulted in the following two publications:

· *Electronically driven spin-reorientation transition of the correlated polar metal $Ca_3Ru_2O_7$*, I. Marković, M. D. Watson, O. J. Clark, F. Mazzola, E. Abarca Morales, C. A. Hooley, H. Rosner, C. M. Polley, T. Balasubramanian, S. Mukherjee, N. Kikugawa, D. Sokolov, A. P. Mackenzie, P. D. C. King, *arXiv*:2001.09499 (2020)

· *Weyl-like points from band inversion of surface states in NbGeSb*, I. Marković, C. A. Hooley, O. J. Clark, F. Mazzola, M. D. Watson, J. M. Riley, K. Volckaert, K. Underwood, M. S. Dyer, P. A. E. Murgatroyd, K. J. Murphy, P. Le Fèvre, F. Bertran, J. Fujii, I. Vobornik, S. Wu, T. Okuda, J. Alaria, P. D. C. King, *Nature Communications* 10, 5485 (2019)

○ During the course of my PhD I have also been involved in other projects, resulting in the following publications:

· *Band hybridisation at the semimetal-semiconductor transition of Ta_2NiSe_5 enabled by mirror-symmetry breaking*, M. D. Watson, I. Marković, E. Abarca Morales, P. Le Fèvre, M. Merz, A. A. Haghighirad, P. D. C. King, *Phys. Rev. Research* 2, 013236 (2020)

· *Direct observation of the energy gain underpinning ferromagnetic superexchange in the electronic structure of $CrGeTe_3$*, M. D. Watson, I. Marković, F. Mazzola, A. Rajan, E. A. Morales, D. M. Burn, T. Hesjedal, G. van der Laan, S. Mukherjee, T. K. Kim, C. Bigi, I. Vobornik, M. C. Hatnean, G. Balakrishnan, P. D. C. King, *arXiv*:1912.11314 (2019)

· *Probing spin correlations using angle resolved photoemission in a coupled metallic/Mott insulator system*, V. Sunko, F. Mazzola, S. Kitamura, S. Khim, P. Kushwaha, O. J. Clark, M. Watson, <u>I. Marković</u>, D. Biswas, L. Pourovskii, T. K. Kim, T.-L. Lee, P. K. Thakur, H. Rosner, A. Georges, R. Moessner, T. Oka, A. P. Mackenzie, P. D. C. King, *Sci. Adv.* 6, eaaz0611 (2020)

· *Momentum-resolved linear dichroism in bilayer MoS_2*, K. Volckaert, H. Rostami, D. Biswas, <u>I. Marković</u>, F. Andreatta, C. E. Sanders, P. Majchrzak, C. Cacho, R. T. Chapman, A. Wyatt, E. Springate, D. Lizzit, L. Bignardi, S. Lizzit, S. K. Mahatha, M. Bianchi, N. Lanata, P. D. C. King, Jill A. Miwa, A. V. Balatsky, P. Hofmann, S. Ulstrup, *Phys. Rev. B* 100, 241406(R) (2019)

· *Direct Observation of a Uniaxial Stress-driven Lifshitz Transition in Sr_2RuO_4*, V. Sunko, E. Abarca Morales, <u>I. Marković</u>, M. E. Barber, D. Milosavljević, F. Mazzola, D. A. Sokolov, N. Kikugawa, C. Cacho, P. Dudin, H. Rosner, C. W. Hicks, P. D. C. King, A. P. Mackenzie, *npj Quantum Materials* 4, 46 (2019)

· *A general route to form topologically-protected surface and bulk Dirac fermions along high-symmetry lines*, O. J. Clark, F. Mazzola, <u>I. Marković</u>, J. M. Riley, J. Feng, B.-J. Yang, K. Sumida, T. Okuda, J. Fujii, I. Vobornik, T. Kim, K. Okawa, T. Sasagawa, M. S. Bahramy, P. D. C. King, *Electronic Structure* 1, 014002 (2019)

· *Orbital- and k_z-selective hybridisation of Se 4p and Ti 3d states in the charge density wave phase of $TiSe_2$*, M. D. Watson, O. J. Clark, F. Mazzola, <u>I. Marković</u>, V. Sunko, T. K. Kim, K. Rossnagel, P. D. C. King, *Phys. Rev. Lett.* 122, 076404 (2019)

· *Dual quantum confinement and anisotropic spin splitting in the multi-valley semimetal $PtSe_2$*, O. J. Clark, F. Mazzola, J. Feng, V. Sunko, <u>I. Marković</u>, L. Bawden, T. K. Kim, P. D. C. King, M. S. Bahramy, *Phys. Rev. B* 99, 045438 (2019)

· *Itinerant ferromagnetism of the Pd-terminated polar surface of $PdCoO_2$*, F. Mazzola, V. Sunko, S. Khim, H. Rosner, P. Kushwaha, O. J. Clark, L. Baw-

den, I. Marković, T. K. Kim, M. Hoesch, A. P. Mackenzie, P. D. C. King, *Proc. Natl. Acad. Sci. U.S.A.* 115, 12956 (2018)

· *Electronic structure and enhanced charge-density wave order of monolayer VSe_2*, J. Feng, D. Biswas, A. Rajan, M. D. Watson, F. Mazzola, O. J. Clark, K. Underwood, I. Marković, M. McLaren, A. Hunter, D. M. Burn, L. B. Duffy, S. Barua, G. Balakrishnan, F. Bertran, P. Le Fèvre, T. K. Kim, G. van der Laan, T. Hesjedal, P. Wahl, P. D. C. King, *Nano Lett.* 18, 4493 (2018)

· *Fermiology and superconductivity of topological surface states in $PdTe_2$*, O. J. Clark, M. J. Neat, K. Okawa, L. Bawden, I. Marković, F. Mazzola, J. Feng, V. Sunko, J. M. Riley, W. Meevasana, J. Fujii, I. Vobornik, T. K. Kim, M. Hoesch, T. Sasagawa, P. Wahl, M. S. Bahramy, P. D. C. King, *Phys. Rev. Lett.* 120, 156401 (2018)

· *Ubiquitous formation of bulk Dirac cones and topological surface states from a single orbital manifold in transition-metal dichalcogenides*, M. S. Bahramy, O. J. Clark, B.-J. Yang, J. Feng, L. Bawden, J. M. Riley, I. Marković, F. Mazzola, V. Sunko, D. Biswas, S. P. Cooil, M. Jorge, J. W. Wells, M. Leandersson, T. Balasubramanian, J. Fujii, I. Vobornik, J. Rault, T. K. Kim, M. Hoesch, K. Okawa, M. Asakawa, T. Sasagawa, T. Eknapakul, W. Meevasana, P. D. C. King, *Nature Materials* 17, 21 (2018)

| Table of Contents

1 | Introduction

Much of the research in condensed matter physics in the recent years is being done under the umbrella term of quantum materials [1–5], which have captured the interest of the community both from the point of view of fundamental understanding of the cornucopia of emergent phenomena in condensed matter, as well as the potential technological applications. New quantum phases of matter are being discovered and studied that are a result of the topology and entanglement properties of the electronic wavefunctions of the system in question, and some well known examples include: superconductors [6–8], where the electronic wavefunction becomes a macroscopic object; topological insulators and semimetals [9–11], in which the wavefunction develops non-trivial topology which differs from that of an atomic insulator; predictions of topological superconductors [10, 12], which combine these two properties and are expected to generate a condensed matter realisation of Majorana fermions, long predicted and sought after in high-energy physics; non-collinear magnets [13, 14], where the spins are entangled even into topologically non-trivial textures such as skyrmion lattices [15, 16]; two-dimensional magnetism recently discovered in van der Waals materials [17–19], contrary to conventional expectations; quantum spin-liquids [20] and spin-ice [21] materials, and many more... As these effects concern the electronic wavefunctions in the materials, the potential applications of the quantum phenomena in materials is mostly oriented towards improvements of the performance of electronic devices. They extend our utilisation of the electron's degrees of freedom in spintronics [22, 23], valleytronics [24] and twistronics [25], or even rebuild our approach to electronics and computation from the ground up, in the quest for quantum computation [26].

A very important aspect dictating the properties of the electronic behaviour in materials is spin-orbit coupling. It is a relativistic effect connecting the electron's spin and orbital angular momenta in an atom, and is typically treated as a weak perturbation in light elements. However, it's strength increases with the size of the atom, and can have considerable influence on the electronic structure where heavy elements are involved [27, 28].

Spin polarisation of 2D electronic states at surfaces and interfaces mediated by spin-orbit coupling has opened a large field of research [29–31]. A number of spin-orbit related phenomena have been studied in the f-electron systems [32], and the majority of work done in the field of topological insulators [9, 10] relies on strong spin-orbit coupling as one of the key tuning parameters. The way spin-orbit coupling acts is closely related to the symmetry of the environment, and often involves the breaking of inversion symmetry [33–38]. The details of how spin-orbit coupling is inter-related to crystal symmetries will be the central theme of this thesis.

A wide variety of the phenomena in quantum materials also arises as a result of electronic correlations, from formation of local moments and magnetism, to correlated metallic states, quantum criticality and unconventional superconductivity [39, 40]. The correlated behaviour is particularly pronounced in d-electron systems, and typically represented in the Mott mechanism of metal-insulator transitions [39, 41]. The strength of interactions there is set by the on-site Hubbard repulsion term for electrons in the same orbital, U. However, it has been shown that Hund's on-site interaction, J_{H}, between electrons in different orbitals, can also provide a route to strong correlation effects [40]. When these potential terms are larger than the kinetic term, given by the bandwidth, W, strong correlation effects are expected to manifest. The strength of the interaction, U/W, is generally observed to decrease with increased number of shells in the electronic structure of the constituent elements, as the valence orbitals become more extended. However, at the same time the spin-orbit interaction shows a strong increase, and it has been shown that this can offset the reduction in interaction strength, allowing strong correlations to develop in the strongly spin-orbit coupled regime [27, 28, 42, 43].

The majority of phenomena which are of either fundamental or technological interest in quantum materials are closely related to their electronic structure. As a method which allows direct insight into the electronic structure of crystalline materials, angle-resolved photoemission spectroscopy has been established as one of the foremost techniques in the investigation quantum materials [6, 44–47]. The combination with theoretical approaches for modelling and *ab initio* calculations of the electronic structure provides an indispensable route to exploration and understanding of quantum materials. In this thesis, I use this approach to study two materials hosting strong spin-orbit coupling and different degrees of electronic interactions, and seek

to uncover the roles these, and their interplay with crystal symmetries, have in shaping the underlying electronic structures.

My thesis is structured as follows. In Chapter 2, I outline the relevant principles of electronic structure theory in crystalline solids. I describe the construction of electronic band theory from the nearly free electron, and the tight-binding perspectives in Section 2.1, before first describing the effects that crystal symmetries and spin-orbit coupling can have on the band structure in Section 2.2, and introducing electronic interactions via Landau's Fermi liquid theory in Section 2.3. In Section 2.4 I show how most common types of interactions, including the electron-electron Fermi liquid model, modify the electronic structure of materials. Chapter 3 is dedicated to the two main methods I have used in this thesis. The theory and the experimental realisation of spin- and angle-resolved photoemission spectroscopy is described in Section 3.1, along with a comment on the most common data analysis techniques. A brief overview of density-functional theory calculations is given in Section 3.2, focused on band structure calculations. Chapters 4 and 5 outline the studies of NbGeSb and $Ca_3Ru_2O_7$, respectively. In both Chapters I include an introduction specific to the material studied, before describing and discussing the results. I conclude the Chapters with a brief outlook on the potential implications of these results within the broader context of quantum materials. Finally, in Chapter 6 I provide an overview of the presented results and some general concluding remarks.

2 | Electrons in solids

2.1   Band structure

The main principle of the behaviour of electrons in crystalline solids is the formation of bands [48–50]. This is a direct consequence of the periodic nature of crystals, and can be demonstrated by two models which construct the band structure of solids from opposite extremes of electronic localisation: the nearly free electron (NFE) model and the tight-binding (TB) model, covered in detail elsewhere. I will give a brief introduction to the problem, and highlight the points particularly relevant to my thesis.

The NFE model [48–50] takes as a starting point a completely free electron, with the parabolic dispersion given by $E = \dfrac{\hbar^2 k^2}{2m_e}$, where $\hbar$ is the reduced Planck constant, m_e is the free electron mass, and E and k are the energy and the momentum of the electron, respectively. Introduction of a weak periodic potential in real space mimics the electric potential of the crystal lattice. The plane-wave states scatter from it in Bragg reflections
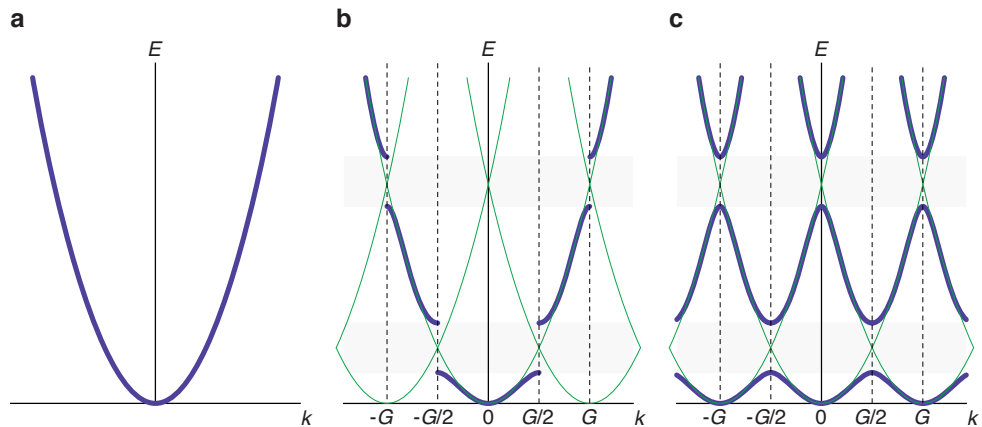
Figure 2.1: **Nearly free electron model. a** Dispersion of a completely free 1D electron. **b,c** Weak periodic potential leads to the formation of Brillouin zones (dashed lines), and I represent the copies of the original free electron parabola, translated by reciprocal lattice vectors **G**, by the thin green lines. The allowed bands (purple dispersion lines) and forbidden gaps in energy (grey) are shown in the extended (**b**), and repeated (**c**) Brillouin zone schemes.

which create standing wave solutions at half-integer multiples of the reciprocal lattice vector, $n\mathbf{G}/2$, in- and out-of-phase with the underlying weak potential. The energies of the standing waves are therefore split by the strength of the periodic potential, creating forbidden gaps in energy, where there are no electronic states. The original free electron parabola is then modified as illustrated in the extended zone scheme in Figure 2.1b. However, by Bloch's theorem, all electronic properties are periodic in momentum space as well, best illustrated in the repeated zone scheme in Figure 2.1c, where the formation of allowed bands and forbidden gaps in the electronic band structure is most obvious. Because of the periodicity, all information in momentum space is contained within any single Brillouin zone, and so we can restrict ourselves to considering only the first zone, $\langle -\mathbf{G}/2, \mathbf{G}/2 \rangle$, in Figure 2.1c, which defines the reduced zone scheme. Despite the difference in their appearance, these pictures are equivalent, and one just needs to be mindful of the counting of the electronic states. Done correctly, the count is always exactly one electron per real-space unit cell for each singly degenerate band in a Brillouin zone, or two electrons for each spin-degenerate band.

The tight-binding model [48–50], on the other hand, takes as a starting point an electron fully localised at an isolated atom in space. We can then bring many such atoms together one by one, arranging them into the periodic lattice and allowing for electrons to hop between atoms due to finite spatial overlap of the original atomic orbitals. This process is parametrised by a hopping integral t as depicted in Figure 2.2a for a one-dimensional chain. We can think of the whole crystal as a large molecule [51], where the electronic states separate in energy from their atomic level, ε_0, with varying degrees of bonding and anti-bonding character. The separation of the most bonding and the most anti-bonding state will not vary much with the number of atoms, and is given by the extent of the orbital overlap as $W = 4t$ in terms of the hopping parameter (Figure 2.2b). In the limit of thermodynamically many atoms in the crystal, the electronic states form quasi-continuous bands of states of width W, showing a cosine dispersion illustrated in Figure 2.2c. We again observe the simple state-counting rule, that one singly degenerate atomic state per unit cell corresponds to one fully filled singly degenerate band in a Brillouin zone.

Beyond this basic introduction to band theory, the tight-binding method provides an extremely powerful framework for intuitive insight into elec-
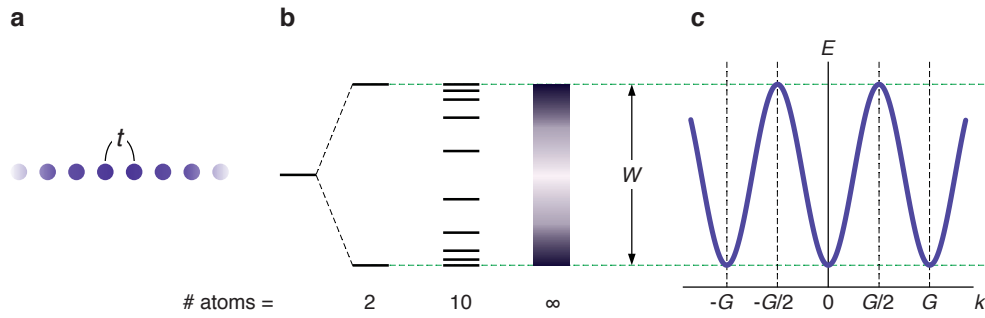
Figure 2.2: **Tight-binding model. a** A model for 1D periodic chain of atoms with nearest neighbour hopping. **b** The energy levels of the generated delocalised states are modified due to the hopping. In the limit of ∞-many atoms in the chain, they form a continuous band of states with a cosine dispersion. The total separation of the highest and lowest energy states, i.e. the degree of bonding or bandwidth, does not depend on the number of atoms in the chain, just on the hopping integral, $W = 4t$. **c** In momentum space these states are distributed in a cosine dispersion.

tronic structure [52, 53]. Setting up an appropriate arrangement of orbitals and hopping parameters between them [54, 55], we can in principle model any real system to an arbitrary degree of complexity/simplicity. Taking multiple orbitals per lattice site results in that number of bands. Their relative positions in energy (given by their respective atomic energy levels ε_0) and their bandwidths (W, given by the atomic orbital overlap, i.e. the hopping strength) determine whether there will be forbidden energy gaps between them, or if the bands will overlap. By allowing hopping between different types of orbitals, the model can develop hybridisations and mixing of orbital characters in the resulting bands.

In the nearly free electron limit, the bands are broad and the eigenstates resemble plane waves since the electrons are highly delocalised, while in the tight-binding limit the bandwidths are relatively modest, and the eigenstates have considerable atomic-orbital character [48–50]. However, these two pictures are adiabatically connected by tuning the degree of electron localisation, or equivalently, the width of the bands. Both approaches have found uses and applicability in real quantum materials: e.g. the nearly free electrons in metallic delafossite oxides [56], or the tight-binding approach in modelling the bands from structural clusters [51, 53, 57].

These basic principles underpin the general band nature of the electronic states in solids, and are sufficient to describe many systems in condensed matter. However, other phenomena will impose restrictions and determine

the relationships between the parameters of these models. Crystal symmetries, spin-orbit coupling and electronic interactions will be of particular importance to the results presented in this thesis.

2.2   Spin-orbit coupling and crystal symmetries

The atomic spin-orbit effect is a relativistic correction to the energies of the electronic states of an atom which comes from the coupling between spin and orbital angular momenta of a state [58]. In a simple picture, it is a phenomenon whereby electron's spin couples to the effective magnetic field in its rest frame, as it moves in the electric potential of the nucleus. This effective magnetic field can be written in terms of the electron's orbital angular momentum, $\mathbf{L}$, and the gradient of the potential of the nucleus, ∇V. Zeeman coupling with the spin $\mathbf{S}$ of the electron then gives rise to a Hamiltonian term proportional to $\mathbf{L} \cdot \mathbf{S}$. With this term, L_z and S_z are no longer good quantum numbers, and instead the total angular momentum is defined as $\mathbf{J} = \mathbf{L} + \mathbf{S}$. The Hamiltonian is then diagonalised by $\mathbf{L} \cdot \mathbf{S} = \frac{1}{2} \left(\mathbf{J}^2 - \mathbf{L}^2 - \mathbf{S}^2 \right)$, and the total energy shift written in terms of the respective eigenvalues is $\Delta E_{\text{SO}} \propto \left(j(j+1) - l(l+1) - s(s+1) \right)$ [58, 59]. The proportionality constant contains a factor of Z^4, where Z is the atomic number, making spin-orbit coupling a much more noticeable effect the bigger the nucleus of the atom. In reality, there is a more structured dependence on orbital n and l quantum numbers, using which detailed atomic properties, including the spin-orbit splitting of electronic levels, can be calculated analytically [60].

The spin-orbit interaction can also affect the band structure of solids. One way its influence can be seen is directly inherited from the atomic case, in the shifting and splitting of the on-site energies of orbitals which would otherwise be degenerate [48, 61]. Perhaps more interestingly though, it can assign different energies to the spin-up and spin-down partners of the same orbital state [60, 62]. However, in a generic situation the orbital states tend to be degenerate in spin due to the simultaneous presence of both time-reversal (T) and inversion (P) symmetries [62, 63].

In a time-reversal invariant system, any state at wavevector k has to have a counterpart at $-k$ with the same energy, but with opposite spin σ:

$$E\left(k, \sigma\right) = E\left(-k, -\sigma\right).$$
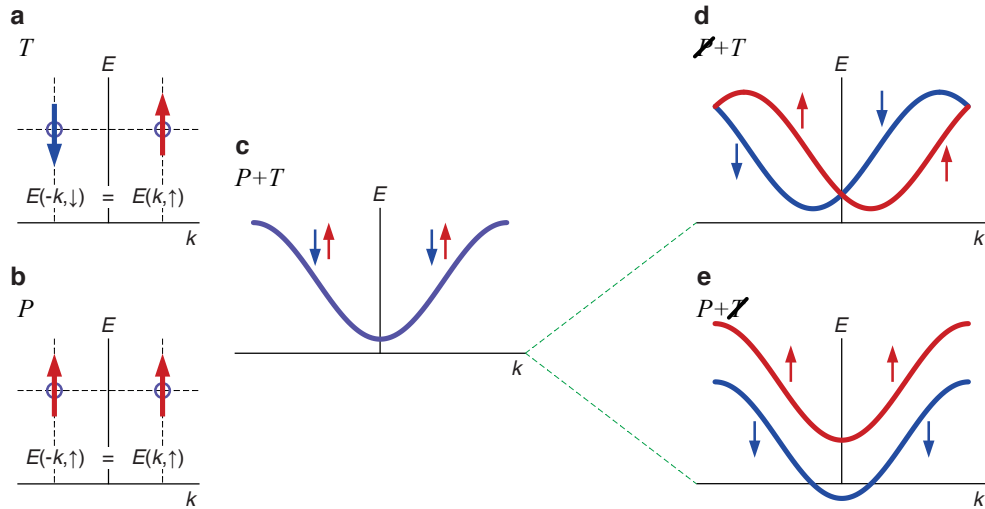
Figure 2.3: **Spin-polarisation of electronic bands.** Illustration of conditions which are imposed on spins in band structures by: **a** time-reversal (T), and **b** inversion (P) symmetries. This results in **c** strict spin degeneracy when both are present in solids. The bands split into spin-up and spin-down copies in different ways when either: **d** inversion, or **e** time-reversal is broken. The nature of the developed spin-splitting preserves the remaining symmetry.

In an inversion invariant system, however, any state at wavevector k has to have a counterpart at $-k$ with the same energy, and with the same spin σ:

$$E\left(k,\sigma\right) = E\left(-k,\sigma\right).$$

Therefore, in any system in which both T and P are present, there can be no spin polarisation of the bands:

$$E\left(k,\sigma\right) = E\left(k,-\sigma\right).$$

Breaking one of these symmetries however, lifts the protection, allowing the spin-up and spin-down bands to separate in a way that still obeys the remaining symmetry [63], as illustrated in Figure 2.3. Removing time-reversal, the bands split "vertically", by a k-independent gap, such as in the case of magnetic exchange splitting [64]. Removing inversion symmetry, on the other hand, spin-orbit coupling leads to an energy gap linear in k, which gives the appearance of a "lateral" splitting of the bands [65–67].

An important example of the influence of SOC in inversion-broken environments is the Rashba effect [33, 35, 68]. It is a spin-orbit coupling

Figure 2.4: **Rashba effect on 2D free electrons. a** Band structure of a two-dimensional free electron gas with Rashba spin-orbit coupling. **b** Spin texture of the constant energy contours of Rashba split bands from **a**.

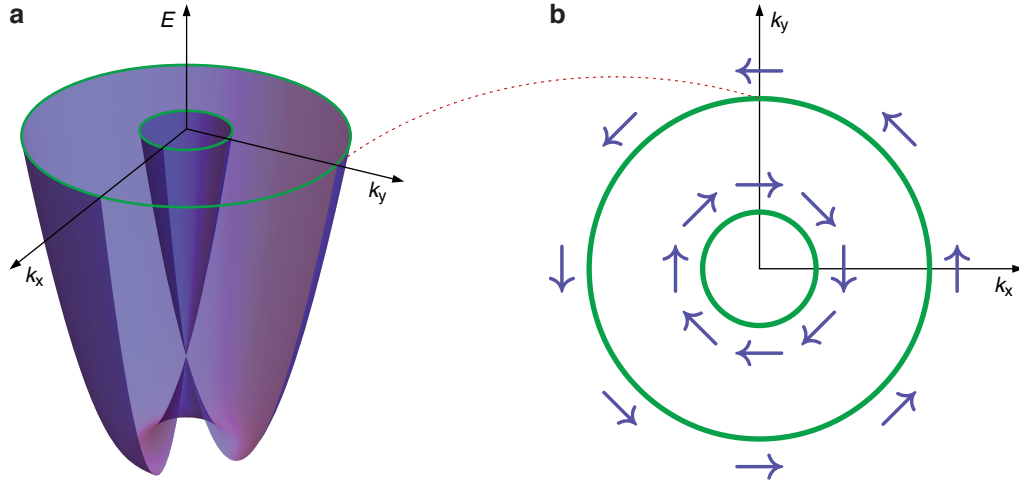term which appears as a result of polar structural environments in solids, e.g. as a bulk effect in wurzite structures [33] or perovskites [69], and as a two-dimensional effect on surfaces, interfaces and heterostructures [30, 35], where a symmetry breaking field develops perpendicular to the plane. Derivation of the Rashba Hamiltonian commonly follows an inaccurate, but intuitive, toy model similar to the derivation of the atomic spin-orbit effect [30, 63]. Relativistic electrons moving within the symmetry-breaking field feel an effective magnetic field in their rest frame. This effective magnetic field can be expressed in terms of the electron's momentum, $\mathbf{p}$, and the direction of the symmetry-breaking field, $\hat{\mathbf{z}}$, giving the well known expression for the Rashba Hamiltonian:

$$H_{\mathrm{R}} = -\alpha_{\mathrm{R}} \left(\boldsymbol{\sigma} \times \mathbf{p} \right) \cdot \hat{\mathbf{z}},$$

where $\boldsymbol{\sigma}$ is the electron spin and α_{R} is the so-called Rashba coefficient.

We can see that the obtained Rashba Hamiltonian indeed provides an energy contribution which is linear in the electron momentum, and changes sign with the spin orientation, as mentioned above. The effect on the band structure in the typical case of a 2D free electron gas with Rashba coupling [65–67] is demonstrated in Figure 2.4. The free electron paraboloid splits radially by spin, as seen in Figure 2.4a, giving two concentric circular pockets in constant energy contours. Furthermore, the form $\boldsymbol{\sigma} \times \mathbf{p}$ locks the spin orientation relative to the direction of the crystal momentum, leading to counter-rotating spin textures on the two pockets, both with winding

number +1, as shown in Figure 2.4b.

More accurate derivations via $\mathbf{k} \cdot \mathbf{p}$ or tight-binding approaches are considerably more tedious and less transparent [63, 70–72]. They do, however, provide some valuable insights [73]. They are capable of quantitative, not only qualitative predictions of the effect, and more importantly for us, they demonstrate that a macroscopic electric field is not strictly required for the Rashba effect to take place, only the corresponding asymmetry in the hopping parameters.

In bulk solids where inversion symmetry breaking is not unidirectional (e.g. in the zincblende structure), a similar phenomenon takes place, known as the Dresselhaus effect [34]. In systems of localised spin which fulfil a set of symmetry conditions determined by Moriya [38], the spin-orbit interaction can manifest by favouring spin canting via an antisymmetric exchange term, known also as the Dzyaloshinskii-Moriya interaction [37, 38]. All these different spin-orbit phenomena always trace back to the atomic $\mathbf{L} \cdot \mathbf{S}$ Hamiltonian, which is reduced to their specific forms by the details of the symmetry environment.

As mentioned above, the spin degeneracy of the electronic bands is lifted in non-centrosymmetric crystal environments [33, 34, 62]. In the bulk, this condition does not actually refer to the bulk space group symmetry, but rather to the point groups of all the sites. If at least one site group is non-centrosymmetric, spin polarisation will develop via: the Rashba effect if there is a net site dipole field, or the Dresselhaus effect if there is only site inversion asymmetry [36]. A crystal can exhibit antipolar ordering of intrinsically non-centrosymmetric structural elements within the unit cell, leading to global restoration of inversion symmetry. Electrons behave according to their local environment, and so the bands develop spin-polarisation within each non-centrosymmetric structural element. This results in bands with opposite spin polarisation, coming from structural elements of opposite polarity, overlapping in energy and thus removing spin polarisation form the global band structure of the centrosymmetric unit cell. Nevertheless, individual bands still hold hidden spin character [36, 74, 75].

This demonstrated the influence of inversion symmetry on overall existence of spin polarisation. However, other crystal symmetries, and their combinations, can have similar effects on particular components of the spin [76, 77]. For example, the combination of time-reversal (T) and any even rotational (C_{2n}) symmetry prevents the development of spin polarisa-

tion parallel to the rotation axis [59]. Symmetry effects can also be more localised in reciprocal space, applying only at certain crystal momenta, **k**. Since the electronic Hamiltonian inherits the full symmetry of the structure, its solutions, the bands, do as well [49, 76, 77]. That means that along the points in reciprocal space which are invariant to a symmetry element such as a mirror plane, rotation axis, or a nonsymmorphic glide plane and screw axis, the bands carry a definite eigenvalue of that symmetry and cannot hybridise with bands of orthogonal eigenvalues. As another example of restricting spin polarisation, imagine a singly degenerate band dispersing along a mirror plane of the Brillouin zone. All of the properties of that band can either have even or odd parity under that mirror symmetry, and therefore the only allowed spin polarisation component is that perpendicular to the mirror (i.e. along the coordinate which the mirror flips).

Such symmetry considerations, of course, apply to all of the properties of the bands, not just the spin. In particular, all consideration for the spin will similarly apply to orbital angular momentum, since both transform as axial vectors under the relevant symmetries [59, 76, 77]. Related to that, as it will prove important later in the thesis, the symmetry restrictions apply to the orbital decomposition of the individual bands, based on how each of the basis orbitals transforms under the given symmetry.

2.3   Interactions: Fermi liquid theory

So far, I have not considered any interactions between the electrons in a material. At a glance, this seems like an unreasonable assumption considering the fact that electrons are charged and interact via the Coulomb potential. The fact that the Coulomb potential is long range, i.e. has a singularity at wavevector $\mathbf{q} = 0$, destabilises the Fermi sea by creating a cascade of electron-hole pairs [78–80]. However, precisely due to the presence of the many conduction electrons, the Coulomb potential is screened in metals, making it short range in the Thomas-Fermi theory [48, 50]. This screening removes the singular part of the interaction, but the rest remains, and in such an environment bare electrons are no longer eigenstates of the system. A generic framework for incorporating the remnant interactions into descriptions of metals was given by Landau in his Fermi liquid theory [81–83], of which a short description is given here following Refs. [78–80].

We can imagine constructing the new eigenstates of the interacting system from the non-interacting bare electrons by introducing the screened

Coulomb interaction. The crucial assumption is that this needs to be done adiabatically, so that no phase transitions occur, and that the eigenstates of the system are adiabatic modifications of the original bare electrons. The interactions induce a cascade of electron-hole pair formation, such that the Fermi sea deforms as shown in Figure 2.5b, depleting states deep below the Fermi level, and occupying states far above it. However, there remains a finite sharp step at the Fermi level, called the Migdal discontinuity, but now only a fraction Z of its size in the non-interacting case. The Migdal step is a signature that the interaction is not singular, as the Fermi sea is not completely destabilised, and it ensures that there exists an adiabatically continuous construction of quasiparticle states from bare electron states. These Landau quasiparticles carry the same quantum numbers as the bare electrons, and therefore also form a Fermi sea, but for which the Fermi step is preserved in full, as in Figure 2.5a.

The quasiparticles are constructed as a superposition of a bare electron, a bare electron with one electron-hole pair excitation, a bare electron with two electron-hole pair excitations, and so on... essentially representing an electron that generates a cascade of electron-hole pairs as it moves around the material. This can be represented with the creation and annihilation operators for the quasiparticles ($\hat{q}$) and for the bare electrons ($\hat{c}$) as:

$$\hat{q}^\dagger = \sqrt{Z}\hat{c}^\dagger + \sum a_{i,j}\hat{c}^\dagger\hat{c}_i^\dagger\hat{c}_j + \sum a_{i,j,m,n}\hat{c}^\dagger\hat{c}_i^\dagger\hat{c}_j\hat{c}_m^\dagger\hat{c}_n + ... \qquad (2.1)$$

The bare electron part comes with a weight factor of $\sqrt{Z}$, where Z is the size of the Migdal discontinuity step, also known as the quasiparticle weight. This relationship shows that as long as the quasiparticles have this direct coherent link to the original bare electron state, the Landau's Fermi liquid construction is stable [80].

Only the part of the electron-electron interaction which destabilises the Fermi sea has been removed by the construction of the Landau quasiparticles. The rest is inherited as the interactions between the quasiparticles which can therefore scatter, meaning they are not exact eigenstates of the system and will have a finite decay rate. However, since the quasiparticle Fermi sea is stable, Pauli's exclusion principle provides very strong phase space restrictions on scattering for quasiparticles near the Fermi level, suppressing their decay rate. A short calculation will give us the parameter space in which the quasiparticles live long enough that the approximation of them being the eigenstates is justified [79, 80]. The situation used in the
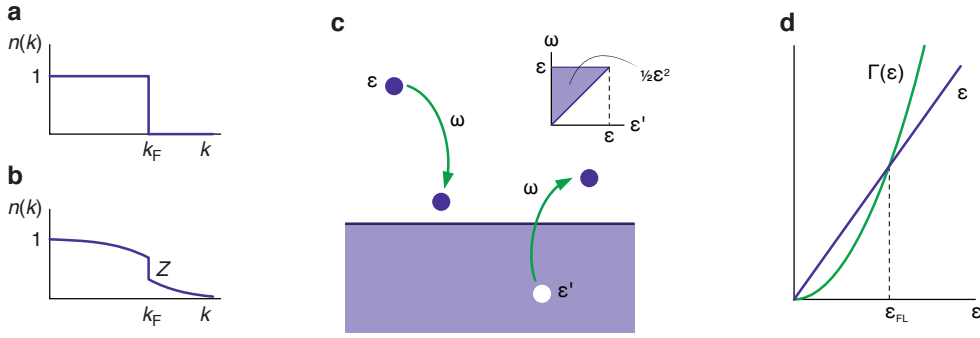
Figure 2.5: **Fermi liquid theory. a,b** Occupation probability functions $n(\mathbf{k})$ for bare electron states of a given $\mathbf{k}$ at $T = 0$ is shown in the: **a** non-interacting, and **b** interacting case. **c** Illustration of the scattering of a quasiparticle off the filled Fermi sea for calculation of the quasiparticle decay rate. The Pauli phase space restriction condition is illustrated in the inset. **d** Comparison of the quasiparticle excitation energy ε and its decay rate Γ, with the intersection value of energy $\varepsilon_{\mathrm{FL}}$ denoting the point where adiabatic continuity, and hence Fermi liquid theory, fails.

calculation is illustrated in Figure 2.5c.

We look at a full Fermi sea and a single quasiparticle with energy ε above it. For this quasiparticle to decay, it needs to scatter off another quasiparticle within the Fermi sea, with energy ε'. Due to the Pauli principle, both quasiparticles need to end up above the Fermi level after scattering, since those are the only available states. If the transferred energy in the process is ω, these Pauli restrictions dictate that $\omega < \varepsilon$ and $\varepsilon' < \omega$. We see already from this that there are less and less scattering options available (quasiparticles with energy ε') the closer the initial quasiparticle is to the Fermi surface, i.e. as ε approaches zero. The decay rate can be quantified using Fermi's golden rule [59] integrated over all available scattering channels:

$$\Gamma_i = \frac{2\pi}{\hbar} \sum_f |\langle i|H_{\mathrm{int}}|f\rangle|^2 \delta(E_f - E_i), \tag{2.2}$$

where $|\langle i|H_{\mathrm{int}}|f\rangle|$ is the matrix element of the interaction, here quasiparticle-quasiparticle scattering process, between the initial and final states, and E_i and E_f are the energies of those states, respectively. We have made the common assumption in the beginning that we are dealing with the screened Coulomb interaction as H_{int}, which is short-ranged in real space and therefore long-ranged in reciprocal space. It is thus justified to approximate the matrix element here as a constant, $|V_0|$. This leaves us with the sum over

the available second quasiparticles, and final states.

Transforming the sum to an integral over energy, each of these three states generates a density of states factor, taken as the density of states at the Fermi level, g_F. The Pauli restrictions, mentioned above, strongly limit the energy integrals over ω and ε' by $0 \leqslant \varepsilon' \leqslant \varepsilon$, giving the total energy factor of $\frac{1}{2}\varepsilon^2$ as seen in Figure 2.5c. Thus we obtain the decay rate of a quasiparticle with the excitation energy ε [79, 80] as:

$$\Gamma(\varepsilon) = \frac{\pi}{\hbar}|V_0|^2 g_\mathrm{F}^3 \varepsilon^2.$$

Two things are of note: quasiparticles exactly at the Fermi level have infinite lifetimes ($\tau = \Gamma^{-1}$) and are therefore exact eigenstates of the interacting system; and there is always a range of energies close to the Fermi level where the quasiparticle decay rate is lower than their excitation energy (Figure 2.5d). When the quasiparticle decay rate exceeds its energy, the quasiparticle decays before the interactions can be fully turned on adiabatically, i.e. before they can be adiabatically formed from bare electron states. This violates the basic assumption of Landau's Fermi liquid theory, and so it breaks down at sufficiently high energies.

Furthermore, if we consider the system at finite temperature, thermal excitations provide a minimum excitation energy scale for the quasiparticles as $\varepsilon \sim k_\mathrm{B}T$, and thus $\Gamma \propto \varepsilon^2$ results in a T^2 temperature dependence of the decay rate as well. In relatively pure metals at low enough temperatures (where other scattering channels have frozen out), one can therefore observe the effect of quasiparticle-quasiparticle scattering in transport experiments as resistivity increases with T^2 [78–80].

As long as adiabatic continuity of the quasiparticle construction holds, the configurational entropy of the quasiparticles is the same as that of the bare electrons, meaning that the number of filled states of the Fermi sea, and hence also k_F, do not change. However, that is not true of their energy. The effect that the interactions have on the energies of the states is in the Fermi liquid theory dealt by Landau's energy functional. On purely symmetry-based arguments, Landau was able to show that the energy change in the single-quasiparticle levels amounts to a simple mass renormalisation as compared to the bare band, changing its velocity (while keeping the same k_F).

In summary, including interactions requires us to switch to new electronic basis states called Landau quasiparticles [78–80]. They differ from the original bare electrons in three main points: they have a coherent contri-

bution of weight Z coming from the original bare electron and an incoherent contribution where the bare electron is dressed in electron-hole pair excitations; they have a finite decay rate which goes to zero at the Fermi level as $\propto \omega^2$; their dispersion is renormalised by giving them a higher effective mass (equivalently, smaller effective Fermi velocity v_F).

2.4   Single-particle spectral function

I started the discussion in this Chapter by constructing the band structure of solids using non-interacting electrons. I then introduced interactions and showed how the resulting Fermi liquid system is naturally described in terms of the Landau quasiparticles [78–80]. Now we turn back and ask what excitations of bare single particles and holes look like in such a Fermi liquid, and how they behave. Crucial insight comes from the realisation that Equation (2.1) can be inverted to represent the bare electron operator in terms of the quasiparticle ones:

$$\hat{c}^\dagger = \sqrt{Z}\hat{q}^\dagger + \sum b_{i,j}\hat{q}^\dagger\hat{q}_i^\dagger\hat{q}_j + ... \tag{2.3}$$

It shows that a single particle excitation is decomposed into a coherent quasiparticle carrying the same quantum numbers with $\sqrt{Z}$, and the incoherent part consisting of a cascade of quasiparticle-quasihole pairs [80]. This approach will in principle allow us to introduce any type of interaction into the model, using the mathematical formalism based on the Green's functions [84].

A Green's function represents the response function of a system when a bare particle (or a hole) with momentum $\mathbf{k}$ is introduced into it at a point in time and then removed at a later point, with the system evolving according to its full Hamiltonian in between [84]. A time-Fourier transform gives a Green's function in frequency and momentum, $G(\omega, \mathbf{k})$, which can be used to calculate the single-particle spectral function by $A(\omega, \mathbf{k}) = -\frac{1}{\pi}\operatorname{Im} G(\omega, \mathbf{k})$, as the poles of the Green's function. The spectral function $A(\omega, \mathbf{k})$ represents the probability of adding a particle or a hole with energy ω and momentum $\mathbf{k}$ to a many-body system [44, 45, 80, 84]. In essence, it therefore represents the electronic structure of the system. In the non-interacting case a particle inserted into the system cannot be scattered as it is in an eigenstate. Therefore the possibility of inserting a particle or a hole into the system exists only exactly at the positions given by the non-interacting,

bare band dispersion, $\varepsilon_{\mathbf{k}}$. The Green's function and the spectral function
are then given by:

$$G^0(\omega, \mathbf{k}) = \frac{1}{\omega - \varepsilon_{\mathbf{k}} \pm i\eta},$$

$$A^0(\omega, \mathbf{k}) = \delta(\omega - \varepsilon_{\mathbf{k}}).$$

An infinitesimal imaginary part η in the Green's function is just an artificial
tool to make the Fourier transform integrable, and the sign is chosen to
preserve causality depending on whether a particle or a hole was introduced.
It is set to zero at the end of the calculation.

In a general case, the particle inserted into the system is scattered by
the interaction Hamiltonian. A perturbative calculation in the interaction
leads to the famous Dyson equation:

$$G(\omega, \mathbf{k}) = \frac{1}{[G^0(\omega, \mathbf{k})]^{-1} - \Sigma(\omega, \mathbf{k})} = \frac{1}{\omega - \varepsilon_{\mathbf{k}} - \Sigma(\omega, \mathbf{k})}, \qquad (2.4)$$

which describes the interacting Green's function as a renormalisation of
the non-interacting Green's function, G^0, by the interactions [84]. In other
words, a quasiparticle (or a quasihole) propagates through the system like
the corresponding non-interacting particle whose properties have been mod-
ified by the term $\Sigma(\omega, \mathbf{k})$, called the irreducible self energy. It is a complex
property,

$$\Sigma(\omega, \mathbf{k}) = \Sigma'(\omega, \mathbf{k}) + i\Sigma''(\omega, \mathbf{k}),$$

and its real and imaginary part carry the dispersive and dissipative con-
tributions to $G(\omega, \mathbf{k})$ as a response function. The former modifies the dis-
persion of the band, and the latter determines the decay rate of the states
in it. The interacting Green's function from Equation (2.4) results in the
following general form of the spectral function:

$$A(\omega, \mathbf{k}) = -\frac{1}{\pi} \frac{\Sigma''(\omega, \mathbf{k})}{(\omega - \varepsilon_{\mathbf{k}} - \Sigma'(\omega, \mathbf{k}))^2 + (\Sigma''(\omega, \mathbf{k}))^2}. \qquad (2.5)$$

It takes the form of a normalised Lorentzian peak as a function of ω, with
its centre moved from the position $\varepsilon_{\mathbf{k}}$ of the bare band by $\Sigma'(\omega, \mathbf{k})$, and a
full width at half maximum (FWHM) of $2\Sigma''(\omega, \mathbf{k})$. The Green's function
formalism used here was for $T = 0$. Finite temperature Green's functions
can be used for a more accurate description at higher temperatures, where
the temperature dependence of the interactions is encoded in the self energy.

The width of the Fermi edge is also affected by temperature, but in most cases a simple multiplication of $A(\omega, \mathbf{k})$ by the relevant Fermi-Dirac distribution factor (f_{FD} for adding a single hole to the system, and $(1 - f_{\mathrm{FD}})$ for adding a single electron) at the given temperature is sufficient to describe this [84, 85].

2.4.1   Example interactions

The described formalism is general, capable of treating any perturbative interaction. I list here how the electronic band structure is modified in the presence of the three most common sources of electron scattering: impurities, electron-electron interactions in terms of the Fermi liquid model described earlier, and electron-boson (i.e. phonons, magnons, ...) interaction. The effect of these types of interactions on the spectral function are illustrated in Figure 2.6.

Impurities in the crystal will only cause incoherent scattering of the electrons. This is simply described by a self-energy term that only has a finite imaginary term, Σ''_{imp}, which does nothing to the dispersion of the band, but gives it a finite lifetime, as in Figure 2.6a [86].

I have already described electron-electron interaction within the Fermi liquid model. The single-particle spectral function allows us to visualise the Landau quasiparticles in terms of the bare single particle excitations as in Equation (2.3). The coherent quasiparticle part of the excitation produces a pole in the Green's function with the weight $Z_{\mathbf{k}}$ and a corresponding peak in the spectral function, while the incoherent part (G_{inch}) only superimposes a smooth, non-singular background (A_{inch}) [45, 79, 86]:

$$G(\omega, \mathbf{k}) = Z_{\mathbf{k}} \frac{1}{\omega - Z_{\mathbf{k}}(\varepsilon_{\mathbf{k}} + \Sigma') - iZ_{\mathbf{k}}\Sigma''} + (1 - Z_{\mathbf{k}})\, G_{\mathrm{inch}},$$

$$A(\omega, \mathbf{k}) = -\frac{Z_{\mathbf{k}}}{\pi} \frac{Z_{\mathbf{k}}\Sigma''}{(\omega - Z_{\mathbf{k}}(\varepsilon_{\mathbf{k}} + \Sigma'))^2 + (Z_{\mathbf{k}}\Sigma'')^2} + (1 - Z_{\mathbf{k}})\, A_{\mathrm{inch}}.$$

For strong electron-electron interaction strengths, the quasiparticle weight, $Z_{\mathbf{k}}$, can become fairly small, making the coherent peak of the quasiparticle barely distinguishable from the incoherent background. We have seen that the dispersive correction from the interactions can be seen as just a mass enhancement, reducing the bandwidth as compared to the bare band, while keeping the same k_{F}. The decay rate depends on ω^2 and on T^2 indepen-
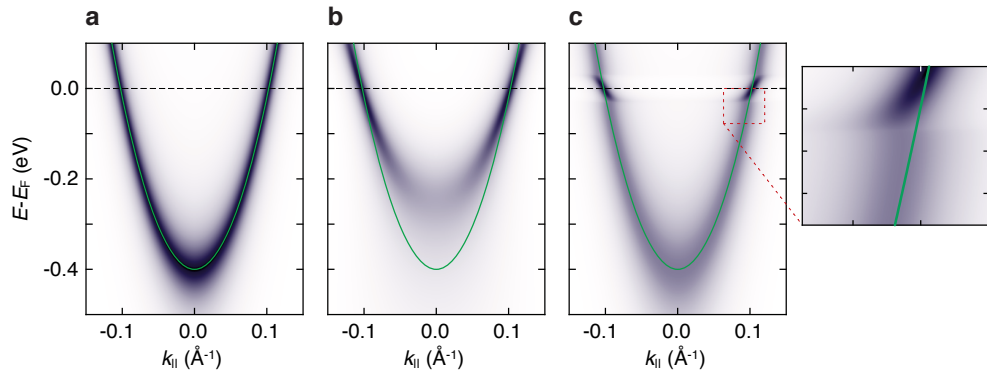
Figure 2.6: **Single-particle spectral function for interacting systems.** Simulated single particle spectral function, for: **a** simple impurity scattering, **b** coherent part of the Landau quasiparticles in a Fermi liquid for electron-electron interaction, **c** electron-boson interaction. The inset demonstrates the "kink" feature, characteristic for electron-boson interactions. The bare non-interacting band is overlaid for each case to better illustrate the effect of the interactions.

dently. All together we have the self energy of the following form:

$$\Sigma(\omega, \mathbf{k}) = \alpha\omega - i\beta \left(\omega^2 + (\pi k_{\mathrm{B}} T)^2 \right),$$

where α and β are factors that depend on the strength of the interaction [79], resulting in the spectral function shown in Figure 2.6b. Quasiparticle weight also depends on the quasiparticle-quasiparticle interaction strength, and indeed it can be related to the mass renormalisation as $Z_{\mathbf{k}} = (1 - \partial\Sigma'/\partial\omega|_{\omega\to\varepsilon_{\mathbf{k}}})^{-1}$.

Interaction with bosons will introduce a specific structure into the spectral function as a result of their characteristic maximal energy (Debye energy, $\omega_{\mathrm{D}} \sim 10$–1000 meV, in case of phonons [87]) typically being much smaller than the quasiparticle bandwidth. We can model the interaction as quasiparticles either emitting or absorbing the bosons [86]. At $T = 0$ the model simplifies as all bosons are in the ground state, and therefore unavailable to be absorbed, meaning only emission processes are possible. I will consider an excited quasiparticle above a filled Fermi sea in two energy regimes: with its energy within ω_D of the Fermi level, $\omega < \omega_D$, and with its energy larger than the characteristic boson energy, $\omega > \omega_D$. In the second case, quasiparticles can emit the full spectrum of bosons, with energies 0–ω_D, independent of their own energy, and so the scattering rate is constant with ω. However, close to the Fermi level, the scattering phase space is

limited by the Pauli restrictions, since the quasiparticle cannot enter the filled Fermi sea, and so it can emit phonons only up to its own energy, ω. This significantly reduces the scattering rate of the quasiparticles within ω_D of the Fermi level, as can be seen in Figure 2.6c. These processes renormalise the dispersion most strongly precisely at the characteristic energy of the bosons, ω_D, resulting in the characteristic "kink" feature [45, 86] seen in Figure 2.6c and its inset. At finite temperatures boson absorption processes become possible as well, which move the quasiparticle away from the Fermi level and are hence allowed at all energies. This has the effect of making the characteristic features become less prominent the higher the temperature of the system.

We will see in Chapter 3 that angle-resolved photoemission spectroscopy directly probes precisely the occupied part of the single-particle spectral function, and therefore has access to information about the electronic structure in solids, including also both the dispersive and the dissipative effects of the quasiparticle interactions.

3 | Methods

In this Chapter I will introduce the two main techniques used in the presented work: angle-resolved photoemission spectroscopy (ARPES), as an experimental method of imaging band structures of solids; and density-functional theory (DFT), as a tool for theoretically predicting band structures from first principles. These two methods are commonly performed together since the experimental results can be used to benchmark the calculations, while the theory can provide information inaccessible to the measurements. Combined, these techniques often yield insights about the problem which would not be possible from either one alone, as I will demonstrate in my results.

3.1   Angle-Resolved Photoemission Spectroscopy

Photoemission spectroscopy is a general term for a family of experimental techniques based on spectroscopy of electrons generated by the photoelectric effect [88], in which a photon of energy $h\nu$ liberates an electron from the material. Einstein recognised the process as a manifestation of the quantum nature of light [89]: a photon incident on a sample can be absorbed by an electron in it, giving the electron enough energy to overcome the work function of the material, Φ, and escape the material. If the photoelectron is then detected in a way which measures the direction in which it was emitted relative to the sample surface, as well as its kinetic energy (given by angles ϑ and φ, and $\mathbf{p}$ in Figure 3.1a, respectively), the technique is called angle-resolved photoemission spectroscopy or ARPES [85]. This is illustrated in Figure 3.1a, and gives ARPES direct experimental access to the momentum-resolved electronic band structure in crystalline solids. I will first give a short introduction to relevant photoemission theory following Hüfner [85, 86] and Damascelli [44, 45], then describe a typical ARPES experiment, and finally the basic ARPES data analysis procedures used in this thesis.

The photoemission itself can be thought of as a scattering process where a particular electron from an initial many-body state $|\Psi_i^N\rangle$ of N electrons within the material is scattered into a total final state $|\Psi_f^N\rangle$ consisting of
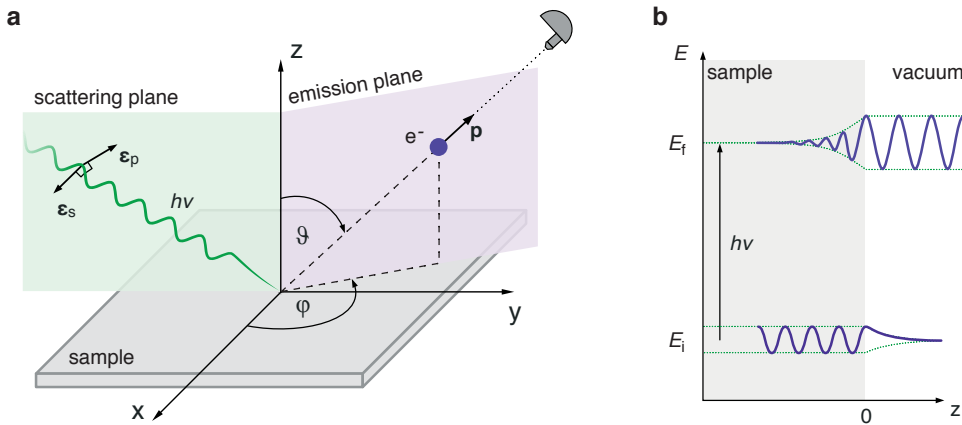
Figure 3.1: **Photoemission process overview. a** Schematic of the photoemission process. Incident photon, $h\nu$, liberates an electron with momentum **p** from the sample at polar angle ϑ and azimuthal angle φ. Polarisation vectors are shown for s and p linearly polarised incident light. **b** A schematic illustration of the one-step model of photoemission [85].

that electron freely propagating away from the surface leaving a hole in the now excited $N-1$ electron many-body state in the material. The probability of that scattering transition is therefore described by Fermi's golden rule [44, 45, 59, 85]:

$$w_{i\to f} = \frac{2\pi}{\hbar}|\langle \Psi_f^N|H_{\mathrm{int}}|\Psi_i^N\rangle|^2 \delta\left(E_f^N - E_i^N - h\nu\right),\tag{3.1}$$

where H_{int} is the Hamiltonian of the electron-photon interaction, the δ-function ensures conservation of the energy in the whole N-electron system. In principle, this process occurs in a single step, where the photoelectron is directly excited from an equilibrium Bloch state in the material to a freely propagating state in vacuum [90]. This final state is known as the inverse-LEED (low-energy electron diffraction) state [85, 91] and has a finite penetration depth into the material, which provides a finite overlap with the initial state needed for the transition. This one-step model is depicted in Figure 3.1b. While this approach treats photoemission correctly, it is too complex for the everyday treatment of experiments. For that reason, photoemission is typically treated in a three-step model [92] which, although an oversimplification of the process, is still highly successful in explaining the experimental results [44, 45, 85].

3.1.1   Three-step model

The three-step model separates the photoemission process into, unsurprisingly, three consecutive steps which it treats independently. Firstly, the electron is optically excited from its equilibrium to an excited state of the system. Secondly, the excited electron travels to the surface of the crystal, typically modelled in terms of a travelling wave packet. And thirdly, the photoelectron needs to overcome the workfunction of the material, escaping into the vacuum where it is detected. Typically, the whole photoemission process is treated as instantaneous, which is known as the sudden approximation. It assumes that the photoelectron leaves the sample without interacting with the remaining excited $N-1$ electronic sea, i.e. the excited photohole, which considerably simplifies the description of the process. This approximation is thought to hold well in a typical ARPES experiment, such as those used in this thesis, but may fail in extreme regimes, e.g. for very slow photoelectrons such as are produced in low-energy laser ARPES. I now give a short description of the three steps [44, 45, 85], highlighting the kinematic restrictions that are imposed at each step, as illustrated in Figure 3.2, arriving in the end at a set of equations used to interpret experimental ARPES data.

i) Optical excitation in the bulk

The first step considers the optical excitation of an electron from an equilibrium Bloch state to an excited Bloch state of the material. A common assumption here is that we can factorise the total wavefunctions of the system, Ψ^N, from Equation (3.1) into $\phi_{\mathbf{k}}$, the part describing of the photoelectron with momentum $\mathbf{k}$, and Ψ^{N-1}, describing the rest [44, 45, 85]. For the final state, we can only perform this factorisation of the wave function by invoking the sudden approximation. Applying this to both the initial and the final Ψ^N states then factorises the transition matrix element from Equation (3.1):

$$\langle \Psi_f^N | H_{\mathrm{int}} | \Psi_i^N \rangle = \langle \phi_f^{\mathbf{k}} | H_{\mathrm{int}} | \phi_i^{\mathbf{k}} \rangle \langle \Psi_{f,\mathrm{m}}^{N-1} | \Psi_i^{N-1} \rangle.$$

The first part, $\langle \phi_f^{\mathbf{k}} | H_{\mathrm{int}} | \phi_i^{\mathbf{k}} \rangle \equiv M_{f,i}^{\mathbf{k}}$, is a one-electron dipole matrix element, and the second is the overlap of the initial state of the remaining $N-1$ electron sea with some excited eigenstate m, $\langle \Psi_{f,\mathrm{m}}^{N-1} | \Psi_i^{N-1} \rangle$. The latter overlap gives a probability that a removal of a single electron from the initial state
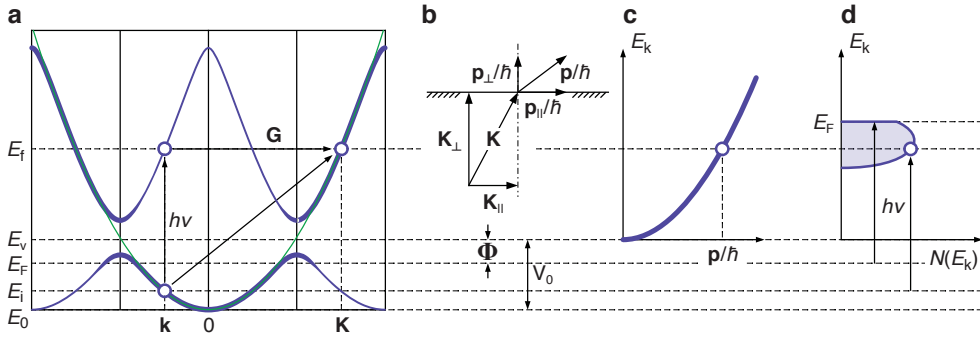
Figure 3.2: **Photoemission kinematics in the three-step model. a** Optical excitation from the initial (E_i) to the final (E_f) state illustrated in the reduced and the extended zone schemes of the NFE approximation. Adapted from Damascelli [45]. **b** Snell's law illustration for the photoelectron leaving the surface of the material in the third step of the model. Adapted from Hüfner [85]. **c** Dispersion of the free photoelectron in vacuum. **d** Energy distribution of the measured photoelectrons.

$|\Psi_i^N\rangle$ leaves the remaining electron sea in an excited state m [44, 45]. The associated probability, summed over m, is precisely the single-particle spectral function, $A(\omega, \mathbf{k})$, described Section 2.4. The photon can be absorbed by any electron (within the photon's penetration depth), and we therefore get the total contribution of the transition matrix to the photoemission intensity by summing over all initial and final states as: $\propto \sum_{f,i} |M_{f,i}^{\mathbf{k}}|^2 A(\omega, \mathbf{k})$.

Complete and accurate evaluation of the one-electron dipole matrix element, $M_{f,i}^{\mathbf{k}}$, is in a general case a complex issue [44, 45, 93, 94], which depends on the energy and polarisation on incident light, symmetry properties and momentum $\mathbf{k}$ of the initial and final states, as well as the details of the experimental geometry. The experimental geometry is determined by the relative orientations of the incident light and the analyser with respect to the sample. Both the direction of the incident light (setting the scattering plane) and its angle to the sample surface affect which initial states can be excited, based on the orbital symmetry of the states and the polarisation of the light. On the other hand, the direction of the emission of the photoelectron (setting the emission plane), can restrict which components of the final state we are able to detect, again based on their orbital symmetry. In a general case, without specific symmetry constraints to the experimental geometry, little can be inferred without detailed simulations [93, 94].

However, with careful control of the experimental geometry, it is still possible to extract some relevant information about the symmetry of the

initial state's orbital decomposition [44, 45, 93, 95–97]. In the case of linearly polarised light, the most useful geometries are with the polarisation vector (ε, see Figure 3.1a) within (p-polarised), or perpendicular (s-polarised) to the scattering plane, and in normal or grazing incidence. Combinations of those can place the polarisation vector along the three orthogonal axes on the crystal, and the orientation of the scattering plane can be set to match an intrinsic symmetry axis of the material. A simple example is demonstrated in the review articles by Andrea Damascelli [44, 45], where the highly symmetric case, of both the scattering and the emission plane coinciding with a mirror plane of the initial orbital is considered. It is then shown that the orientation of the light polarisation vector selects only the orbital character of the initial states with the matching mirror parity to appear in the measured spectrum, i.e. p-polarised light excites only the even-orbital contributions, while s-polarised light excites only odd-orbital contributions of the initial state.

Finally, the first, optical excitation step of the three-step model needs to obey the conservation of energy and momentum. Total energy conservation of the photoemission process, as given by the δ-function of Fermi's golden rule (Equation (3.1)), can within the sudden approximation be reduced to a simpler statement concerning only the energy of the electron being photoexcited, $E_f = E_i + h\nu$ [85]. The energy of the electron does not change after the optical excitation, as demonstrated by the horizontal line marking E_f in Figure 3.2.

The implications of the conservation of momentum are slightly more nuanced. Firstly, we typically neglect the momentum of the incident photon, which is a good approximation for standard ARPES experiments where the photon energy is below the soft x-ray regime ($h\nu \lesssim 100$ eV) and the corresponding photon momentum is much smaller than the typical Brillouin zone ($|\mathbf{G}| \sim 10$–20 Å^{-1}) [45]. This makes the transition "vertical" in the reduced Brillouin zone picture: $\mathbf{k} = \mathbf{K}$, where I use $\mathbf{k}$ and $\mathbf{K}$ for the crystal momentum of the initial and the final state, respectively. However, it is more useful in photoemission to think in the extended zone scheme [91], where it is explicitly seen that the periodic lattice provides momentum $\mathbf{G}$ to reach the final state, as depicted in Figure 3.2a. Without the lattice, there would be no final state available for a vertical transition. That gives total momentum conservation, $\mathbf{K} = \mathbf{k} + \mathbf{G}$, but also the equivalent for its components $\mathbf{K}_{\parallel} = \mathbf{k}_{\parallel} + \mathbf{G}_{\parallel}$ and $\mathbf{K}_{\perp} = \mathbf{k}_{\perp} + \mathbf{G}_{\perp}$, parallel and perpendicular

to the crystal surface, respectively [44, 45, 85]. The momentum conservation for the component perpendicular to the surface only holds here because of the assumption that the excitation step occurs between proper bulk Bloch states, such that $k_\perp$ is a good quantum number. This is not true close to the surface, which will be important in step *iii*).

ii) Transport to the surface

The second step of the 3-step model involves the final-state wavepacket travelling towards the surface of the crystal [44, 45, 85]. Only the electrons which do not scatter before reaching the surface contribute coherently to the photoemission process. Therefore, the relevant parameter here is the inelastic mean free path of that electron, λ_{mfp}, which, in combination with the light penetration depth in the material, sets the limit on the probing depth for photoemission techniques. We can describe the resulting attenuation of photoemission intensity with depth using Beer-Lambert's law [98]: $I(z) = I_0 \exp(-z/\lambda_{\text{mfp}})$, where $1/\lambda_{\text{mfp}}$ can be thought of as an imaginary contribution to the out-of-plane momentum of the final state, $K_\perp \to K_\perp + i\lambda_{\text{mfp}}^{-1}$. This reduced extent of the effective final state into the system means that $K_\perp$ is no longer a well defined quantum number, and that the final state becomes intrinsically broadened in momentum, resulting
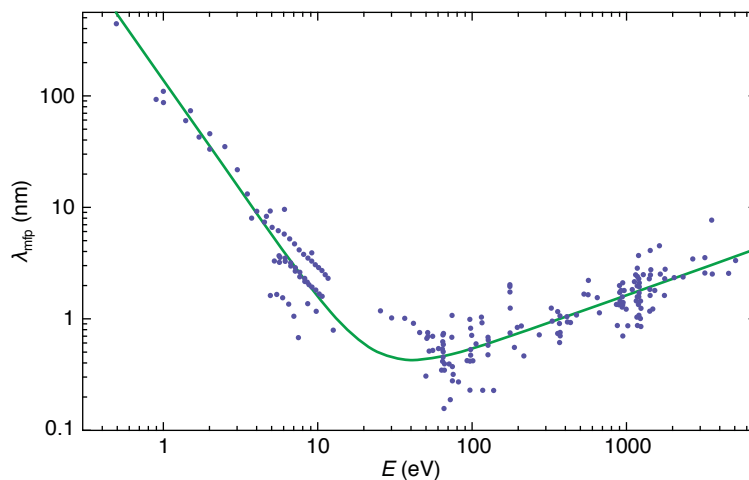

Figure 3.3: **Universal inelastic mean free path.** Material independent of the inelastic mean free path, λ_{mfp}, as function of the energy of the electron. Adapted from Seah and Dench [98].

in a broadening factor [85, 99] of:

$$\frac{1}{\left(k_\perp - K_\perp\right)^2 + \left(1/\lambda_{\mathrm{mfp}}\right)^2}.$$

The inelastic mean free path is found to change non-monotonically with the energy of the electron, following the same "universal" dependence seen in Figure 3.3 for most materials [98]. The curve has a minimum around typical ARPES energies, making the technique very surface sensitive, with a probing depth of $\lesssim 1$ nm. All the electrons that do get scattered during this step, but still leave the crystal, are known as "secondary" electrons and contribute to a **k**-uniform, but stepped in energy, background in the measured photoemission intensity [85, 100–103].

iii) **Escape into vacuum**

Upon reaching the surface, if the energy of the final state is above the vacuum level, the photoelectron will leave the crystal [85, 91]. As mentioned before, there is no change in the energy of the electron in this step. There is, however, a difference in the definition of the zero-energy point on two sides of the surface. Within the crystal, the reference point for energies within the crystal is given by the Fermi level, which sits below the vacuum reference point for the kinetic energy of the free electron, E_k. The difference is the work function of the material, Φ. Since the energy is conserved, this gives us $E_f = E_\mathrm{k} + \Phi - h\nu$, where E_f and E_k are both positive, and measured from E_F and the vacuum level E_v, respectively, as seen in Figure 3.2a,c.

On the other hand, crossing the surface does have a real effect on the momentum of the photoelectron. The reason for that is the same as the source of the work function: there is a discontinuous step in the electrostatic potential that happens at the surface of a material. Since the discontinuity exists only in the out-of-plane direction, by Fresnel equations the component of the momentum parallel to the surface is conserved [85], and we have $\mathbf{p}_\parallel/\hbar = \mathbf{K}_\parallel$, where $\mathbf{p}$ is the momentum of the free electron in vacuum. The effect on momentum perpendicular to the surface is easily understood if we interpret the surface potential step as a difference in effective impedances for electrons as waves in the material and in vacuum. The momentum perpendicular to the surface is then not conserved for electrons crossing it in a general case [45, 85, 91]. In order to quantify the loss of $K_\perp$ across the surface, we have to resort to a specific model for the final state.

The most commonly used one assumes that the final Bloch state in the crystal is a nearly free electron state, as described in Chapter 2, and illustrated in Figure 3.2a. This approximation is expected to work well for simple metals with NFE Fermi surfaces, and for final states which are high enough in energy that the crystal potential can be seen as only a small perturbation [45]. However, it has become broadly used also in systems where the initial states are not free electron-like. The NFE approach treats the surface potential as a constant, V_0, known as the inner potential. It represents the energy difference between the bottom of the NFE band of the final state and the vacuum level[1], i.e. the bottom of the free electron dispersion in vacuum, as depicted in Figure 3.2. The electron is treated as a plane wave on both sides of the surface, and so crossing the surface is perfectly described by Snell's law [85], seen in Figure 3.2b. That allows us to determine the out-of-plane momentum component of the final state as $\hbar^2 K_\perp^2 = p_\perp^2 + 2mV_0$ [91], in keeping with the view of the surface as a step in impedance.

Photoemission intensity

The three-step model allows us to write the total photoemission current of free electrons with kinetic energy E_k, emitted in the direction defined by the angles ϑ and φ, and obtained from excitation by photons of energy $h\nu$ [44, 45, 85]. Doing it step-wise, to better illustrate where the factors come from, this gives:

$$I(E_\mathrm{k}, \vartheta, \varphi, h\nu) \propto \sum_{f,i} |M_{f,i}^\mathbf{k}|^2 A(E_i, \mathbf{k})$$
$$\cdot\, \delta(E_f - E_i - h\nu)\delta(\mathbf{K}_\parallel - \mathbf{k}_\parallel - \mathbf{G}_\parallel)\delta(K_\perp - k_\perp - G_\perp)$$
$$\cdot\, \frac{1}{(k_\perp - K_\perp)^2 + (1/\lambda_\mathrm{mfp})^2}$$
$$\cdot\, \delta(E_\mathrm{k} + \Phi - E_f)\delta(\mathbf{p}_\parallel - \hbar\mathbf{K}_\parallel)\delta(p_\perp^2 + 2mV_0 - \hbar^2 K_\perp^2),$$

where the purple factors come from step *i)*, the green from *ii)*, and the red from step *iii)* of the model as it is described above. With some reordering of the factors in the above expression, and combining some of the δ-functions,

---

[1] The inner potential, V_0, corresponds to the depth of the potential well in the Sommerfeld model of a metal.

we obtain:

$$I(E_k, \vartheta, \varphi, h\nu) \propto \sum_{f,i} A(E_i, \mathbf{k}) \frac{|M_{f,i}^{\mathbf{k}}|^2}{(k_\perp - K_\perp)^2 + (1/\lambda_{\text{mfp}})^2}$$

$$\cdot\, \delta(E_k + \Phi - E_i - h\nu)$$

$$\cdot\, \delta(\mathbf{p}_\parallel/\hbar - \mathbf{k}_\parallel - \mathbf{G}_\parallel)\delta(p_\perp^2/\hbar^2 + 2mV_0/\hbar^2 - (k_\perp + G_\perp)^2).$$
$$(3.2)$$

This directly illustrates that by measuring $I(E_k, \vartheta, \varphi, h\nu)$ an ARPES experiment records the single-particle spectral function of the initial states $A(E_i, \mathbf{k})$, modulated by the matrix effects and final state broadening effects. The free electron momentum $\mathbf{p}(E_k, \vartheta, \varphi)$ is a function of the kinetic energy and the emission angles from Figure 3.2a. Therefore, the energy and momentum conservations given by the δ-functions lead to a set of equations relating the parameters of the measured photoelectron to those of the initial state [44, 45, 85]:

$$E_i = E_k + \Phi - h\nu \tag{3.3}$$

$$k_x = \frac{\sqrt{2m_e}}{\hbar}\sqrt{E_k}\sin\vartheta\cos\varphi \tag{3.4}$$

$$k_y = \frac{\sqrt{2m_e}}{\hbar}\sqrt{E_k}\sin\vartheta\sin\varphi \tag{3.5}$$

$$k_z = \frac{\sqrt{2m_e}}{\hbar}\sqrt{E_k\cos^2\vartheta + V_0}. \tag{3.6}$$

The energy convention here has $E_i < 0$ measured from the Fermi level. This definition is used throughout the thesis, and denoted as $E - E_F$. The only value not directly measured is V_0 which is most commonly, and most reliably, determined as an experimental fit parameter in the dependence of k_z on incident photon energy $h\nu$ (and hence E_k).

3.1.2   ARPES experiment

In a typical ARPES experiment, shown in Figure 3.4a, a source of monochromatic light is used to photoemit electrons from a single-crystalline sample. Photoelectrons leave the sample with a kinetic energy E_k in different directions relative to the surface of the sample (angles ϑ and φ in Figure 3.1a). The electrons emitted within a certain solid angle of acceptance in the direction of the analyser are first collected into a series of electromagnetic
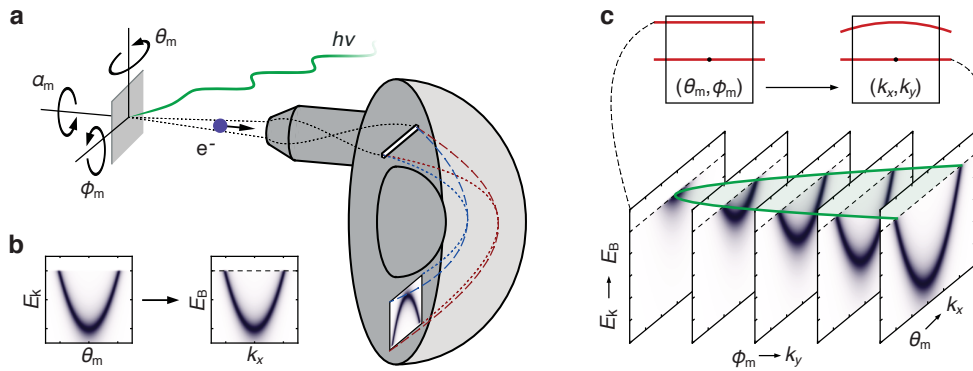
Figure 3.4: **Data collection and processing. a** Schematic of the APRES experiment. The orientation of the sample is determined by three angles: polar θ_m, tilt ϕ_m, and azimuth α_m. **b** Processing of the measured dispersions. **c** Illustration of the Brillouin zone mapping by changing the angle perpendicular to the analyser entrance slit (ϕ_m in this geometry), and the related data processing.

lenses which modify their overall kinetic energy, and adjust their trajectories to provide angular resolution. The electrons are then directed onto the entrance slit of the hemispherical analyser. The entrance slit is a thin opening, selecting only the electrons within a 1D subset of that solid angle (i.e. angle along the slit, θ_m in Figure 3.4) to be passed into the analyser. The analyser is in essence a hemispherical capacitor, where the electrons entering it get separated by energy in the direction perpendicular to the slit. After passing through the hemisphere (Figure 3.4a), the electrons arrive at a microchannel plate (MCP) detector, producing 2D intensity maps in kinetic energy versus the angle along the entrance slit, demonstrated in Figure 3.4b.

Brillouin zone mapping

By changing which part of the emission solid angle is mapped onto the entrance slit of the analyser, we can detect electrons emitted within a large total solid angle. This is typically achieved by rotating the sample along the angle perpendicular to the slit direction, ϕ_m in Figure 3.4. The θ_m and ϕ_m angles define the position of the physical sample within the experiment, and are not to be confused with emission angles ϑ and φ from Figure 3.1a. They do, however, span the same space and therefore map onto the in-plane crystal momentum $\mathbf{k}_\parallel$ [104]. Therefore, by collecting many dispersion scans at small increments of the ϕ_m angle, we can acquire a three-dimensional

dataset of electronic states in the material spanning the surface projected Brillouin zone, as illustrated in Figure 3.4c. We can then also extract constant energy contours of the bands from such a dataset, which, taken at E_{F}, correspond to the image of the Fermi surface of the material, commonly referred to as Fermi surface maps.

The described procedure is only one way to map the in-plane momentum space in an ARPES experiment, albeit the most widely used one. If the azimuthal angle of the sample, α_{m}, can be changed as well, then the space of the emission solid angle defined by (ϑ, φ) is over-constrained by the three orientational angles of the sample $(\theta_{\mathrm{m}}, \phi_{\mathrm{m}}, \alpha_{\mathrm{m}})$, and any two of them can be used to perform the mapping. Alternatively, some designs [104] of the analyser now use electromagnetic deflectors in the lens system which can selectively project different parts of the acceptance solid angle onto the analyser entrance slit, without the need to physically move the sample itself.

k_z mapping

In order to get information on the out-of-plane dispersion of the bands, along k_z, we perform a different kind of mapping procedure, varying photon energy, $h\nu$, for a given measured dispersion [44, 45]. Following Equation (3.6), we see that changing the photon energies, which then changes E_{k}, will lead to probing different k_z values. However, the size of the in-plane momentum component, $\mathbf{k}_{\parallel}$, also changes the probed k_z for a fixed photon energy. It is therefore easiest to see how this works at normal emission (i.e. $\cos\vartheta = 1$ and $\mathbf{k}_{\parallel} = 0$), when all of the kinetic energy of the detected photoelectron is in $\mathbf{p}_{\perp}$ (Figure 3.2b). Any variation in the binding energy of the measured band with $h\nu$ is then entirely determined by its dispersion along k_z. However, in reality, photon energy does not precisely determine the value of k_z. As described in step ii) of the three-step model, the damping of the final state by the finite inelastic mean free path, λ_{mfp}, results in the equivalent broadening of the $K_{\perp}$ [99]. The experiment therefore probes a finite-size k_z interval, in some cases even on the order of $2\pi/c$, the size of the out-of-plane dimension of the Brillouin zone. Bands with strong intrinsic k_z-dispersion will appear as broadened features, their binding energy integrated over the probed k_z interval. At high photon energies λ_{mfp} becomes larger, and the technique becomes more bulk sensitive, reducing the intrinsic k_z-width of the bands and increasing the effective k_z-resolution [99]. Soft x-rays (100 eV–10 keV) are therefore often needed in order to have suffi-

cient effective k_z-resolution to observe the out-of-plane dispersion of bands in this type of experiment. On the other hand, highly two-dimensional states, such as surface states or states confined to crystal layers parallel to the surface, will have very little out-of-plane dispersion. This makes them appear narrower than three-dimensional states in the measurements, with their measured linewidths reliably reflecting only the intrinsic lifetime of the initial state [45, 85, 99, 105].

Data processing

The raw measured datasets need to be processed, and converted from the experimental parameters to initial electronic state parameters using Equations (3.3) to (3.6). First, the measured E_k is converted to E_i of the initial state (for each measured dispersion slice if a mapping procedure was performed). This is done by using Equation (3.3), where the workfunction of the material is replaced by the workfunction of the analyser which sets the position of the vacuum level in the measurement process. Furthermore, the energy axis conversion requires a reliable Fermi level reference in the measured data (see Figure 3.2d). An added complication is that a straight entrance slit generates curvature on the energy axis in the measured data due to the hemispherical geometry of the analyser. This is resolved by acquiring a reference dispersion across the Fermi level on a polycrystalline gold sample, showing a uniform Fermi step across the detector. The fit of the Fermi level position is then applied to correct the measured dispersions and convert the energy axis into E_i.

The angle-axes parallel and perpendicular to the entrance slit of the analyser are converted into in-plane crystal momentum components by using Equations (3.4) and (3.5) relative to the position of normal emission (NE) in the data. Since this conversion is non-linear, dispersions for which the slit direction does not contain the NE point actually image a curved line in momentum space. This is illustrated in Figure 3.4c for the example of Brillouin zone mapping, where we need to convert the energy axis and the two in-plane momentum axes.

In the case of k_z-maps, the mapping axis is given as $h\nu$ by the experiment. For each $h\nu$ value, the measured dispersion is converted to E_i and $k_\parallel$ along the slit, by the procedure described above. If the inner potential, V_0, can be reliably determined, typically from the observed periodicity of the band dispersions with varying photon energy, the $h\nu$ axis of the map can

be converted into k_z by using Equation (3.6).

Spin-resolved ARPES

If the detection in an ARPES experiment is done in a way which is sensitive to the photoelectron's spin orientation, we can also measure the spin polarisation of the bands in a given material [106, 107]. There are several ways to achieve this, and our experiments were performed on experimental setups where the ARPES analyser was fitted with very low energy electron diffraction (VLEED) spin-detectors [108–110]. Electrons from the desired part of the dispersion are passed through an additional aperture positioned next to the MCP detector on the exit of the analyser, and scattered off magnetised O-passivated $Fe(001)p(1\times1)$-O thin film targets [111]. The exchange interaction between the magnetised target and the incident electrons provides a spin-selective scattering cross-section, and the electrons whose spin is aligned with the magnetisation of the target are preferentially scattered into a channeltron detector (electron counter).

By comparing the counts measured with the target magnetised in the two opposite directions along the same axis α (I_α^+ and I_α^-) for any $(E, \mathbf{k})$ point, we can determine the spin polarisation along α of that point [106, 107] as:

$$P_\alpha = \frac{1}{S}\frac{I_\alpha^+ - I_\alpha^-}{I_\alpha^+ + I_\alpha^-},$$

where S is an experimental parameter known as the Sherman function [112]. The Sherman function encodes the relative reflectivity of the opposite-spin species, defining the spin-differentiation efficiency of the experiment [106, 107]. For the $Fe(001)p(1\times1)$-O thin-film targets in VLEED detectors, the Sherman function is usually ≈ 0.2–0.4 [111], meaning that a 100% polarised electron beam would result in a 20–40% difference in measured count numbers. Knowing the polarisation of a dispersion point $(E, \mathbf{k})$ allows us to also extract the true contributions of spin-up and spin-down electrons along α for that point [106, 107] as:

$$I_\alpha^{\uparrow,\downarrow} = \frac{I_\alpha^+ + I_\alpha^-}{2}(1 \pm P_\alpha).$$

In our experiments, this procedure was performed point by point at constant energy, i.e. along momentum distribution curves (MDC) and at constant momentum, i.e. along energy distribution curves (EDC). The example of this procedure is demonstrated on an example MDC dataset in Figure 4.13.
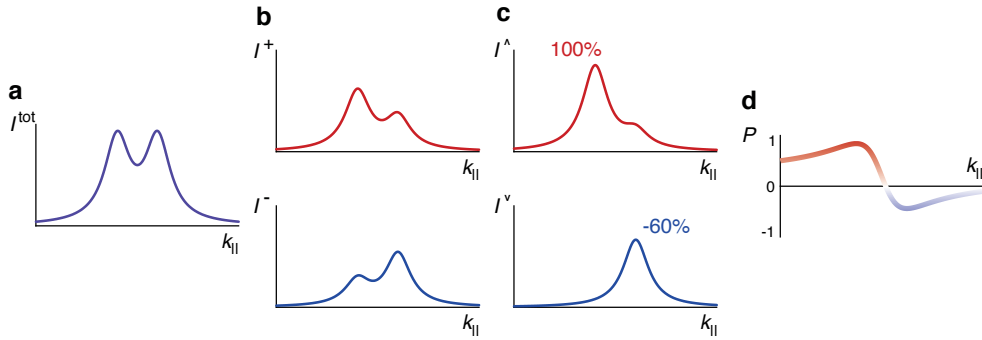
Figure 3.5: **Schematic spin-polarisation measurement of bands with ARPES. a** Sample data of a spin-integrated MDC. **b** The same MDC measured for positive (top), and negative (bottom) magnetisation of the VLEED target. **c** "True" spin-up (top) and spin-down (bottom) MDCs along the target magnetisation direction, calculated from (**b**). The numbers indicate the polarisation of each of the two bands. **d** Polarisation MDC calculated from (**b**).

The spectral weights attributed to individual bands, which can be extracted by peak-fitting procedures described below, can be analysed in the same way, yielding the polarisation values of the corresponding bands, represented in Figure 4.13c.

Any one target can only be used for two orthogonal axes α [106, 113]. Therefore, two VLEED targets are used with a 90° relative orientation [109, 110]. Each target is oriented such that it provides one of the orthogonal in-plane polarisation axes ($\hat{\mathbf{x}}$ or $\hat{\mathbf{y}}$) and the out-of-plane axis ($\hat{\mathbf{z}}$). Performing the measurement along the same EDC or MDC line with target magnetisations along each of the three axes, and both directions of magnetisation along each axis, we can extract the full polarisation vector of the bands by the procedure described above [106, 107, 109, 110, 113].

3.1.3 Experimental setup

In order to perform photoemission experiments, we need a source of high-intensity, monochromatic light, well focused on the sample. Most common laboratory-based options are plasma gas-discharge lamps and laser sources [86]. Plasma lamps are the easiest to maintain and use, but provide comparably low photon flux and no variability in photon energy. Laser sources, are more intense and provide very good resolution [114–116], but are often limited to very low photon energies, and are generally much more difficult to operate. Synchrotron facilities, however, provide light sources
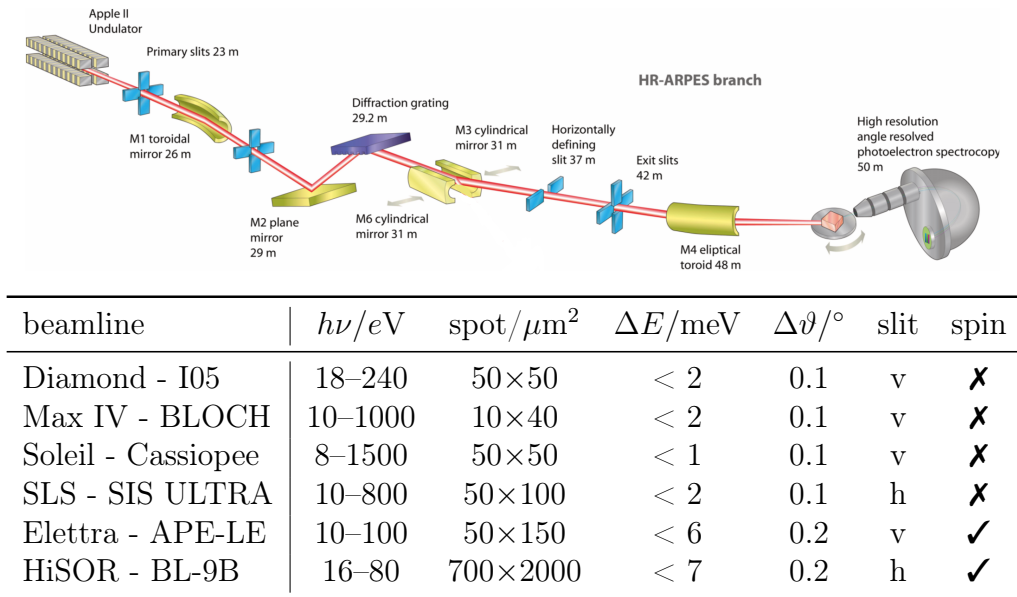
beamline	$h\nu/e$V	spot$/\mu$m^2	ΔE/meV	$\Delta\vartheta/°$	slit	spin
Diamond - I05	18–240	50×50	< 2	0.1	v	✗
Max IV - BLOCH	10–1000	10×40	< 2	0.1	v	✗
Soleil - Cassiopee	8–1500	50×50	< 1	0.1	v	✗
SLS - SIS ULTRA	10–800	50×100	< 2	0.1	h	✗
Elettra - APE-LE	10–100	50×150	< 6	0.2	v	✓
HiSOR - BL-9B	16–80	700×2000	< 7	0.2	h	✓

Figure 3.6: **Synchrotron beamlines.** Layout of the I05 beamline at Diamond Light Source, adapted from Hoeosch *et al.* [118], represents a typical ARPES beamline. The table lists some important technical details of the beamlines used in this thesis [108–110, 118–123]. Effective energy and angle resolutions for spin-resolved measurements in our experiments were 100 meV and 0.3°, respectively.

with very good photon fluxes over a wide energy range [45].

Synchrotrons are accelerator facilities where electrons are kept circulating along a curved path, producing tangential EM radiation as they curve [117]. Additional dipolar-magnet arrays called undulators are used to amplify the emitted synchrotron radiation within a given energy band and polarise it. Beamlines built around the electron storage ring guide the radiation from the undulators to various specialised user-based endstations where the synchrotron light is used in a multitude of different experiments. Complex beamline optics are used to select and monochromise the energy of the incoming photons, as well as direct and focus the light beam onto the sample. A typical outline of a synchrotron ARPES beamline is shown in Figure 3.6. Results presented in this thesis have been collected across six beamlines [108–110, 118–123], all at different synchrotron facilities. The main technical properties of the beamlines are summarised as a table in Figure 3.6.

ARPES experiments have another large technical requirement, which is that they need to be conducted in ultra-high vacuum (UHV) conditions with $p \sim 5 \cdot 10^{-11}$ mbar for optimal resolution and data quality [45, 86]. There

are multiple reasons for this. Most importantly, the photoelectrons need to travel a distance on the order of a meter from the sample until they are detected on the MCP in the analyser, without scattering. Also, as I have mentioned already, ARPES is a surface-sensitive technique. This means that any contaminants or adsorbates [124] (e.g. air molecules) greatly reduce the data quality by introducing random scattering both in the final state, as photoelectrons leave the surface, and in the initial state, increasing the impurity scattering contribution of the self energy from surface scattering [86].

The entire experimental endstation is therefore enclosed within a UHV chamber, with the sample mounted onto a motorised manipulator, allowing ideally, 6-axis motion (3 translations, 3 rotations). The (x, y, z) translations position the sample in the path of the incident light and at the focus of the analyser, while polar, tilt and azimuthal angles, $(\theta_{\mathrm{m}}, \phi_{\mathrm{m}}, \alpha_{\mathrm{m}})$, control the orientation of the sample relative to the entrance slit of the analyser as indicated in Figure 3.4a.

The relative orientation of the analyser entrance slit to the manipulator axis sets which manipulator angle needs to change to perform the Brillouin zone mapping procedure [104]. In the standard, vertical, position of the manipulator, vertical slit orientation uses the polar angle, while horizontal slit uses the tilt angle for mapping (Figure 3.4). As the light scattering plane is typically horizontal, different slit orientations will result in different symmetry conditions on the matrix elements in the measurements.

Sample surfaces do not only need to be atomically clean, they also need to be reasonably flat and uniform along some crystal plane [124]. Steps and terraces are unavoidable in practice, but do not present a problem unless their size is so small as to make the surface amorphous. This means that the samples need to be single-crystalline, at least on the length scale of the spot size of the incident light beam. The presence of polycrystallinity, multiple domains, or surface roughness can defeat the purpose of a momentum-resolved experiment, as they will integrate the spectrum over all crystallite orientations. Atomic flatness of the surfaces is achieved by cleaving the crystal along the desired direction. To have the surface clean, the cleave is done *in situ*, under measurement conditions of ultra-high vacuum and with the sample at base temperature [124]. A special technique is used for *in situ* cleaving, where we use silver epoxy to glue a small ceramic top-post onto the sample surface. The top-post is then knocked off in UHV, cleaving

away the top part of crystal. The same silver epoxy is also used to glue the sample to its holder, since good electrical contact is needed to ground the sample and prevent charge build-up due to a large current of photoelectrons leaving the sample.

3.1.4   Data analysis

As discussed in Section 2.4, a lot of information about the electronic states and their interactions is encoded in the spectral function (Equation (2.5)), which ARPES measures [45, 86]. In order to extract quantitative information from the experimental intensity maps, be they dispersions or constant-energy contours, we perform lineshape fitting analysis on the processed datasets. The fits provide quantitative estimates of the positions and widths of the bands, from which we can extract the interaction self energy $\Sigma(\omega, \mathbf{k})$ if the bare band dispersion $\varepsilon_{\mathbf{k}}$ is known. Typically, the fits are performed on one-dimensional cuts extracted from the data at either constant energy or constant momentum, known as momentum distribution curves (MDC) and energy distribution curves (EDC), respectively (see Figure 3.7a). From Equation (2.5) it can be shown that linecuts will have a Lorentzian shape in the EDCs if: *i*) Σ'' is energy-independent, *ii*) Σ' is at most linear in energy; and in the MDCs only if: *i*) Σ'' is momentum-independent, *ii*) Σ' is at most linear in momentum, *iii*) the bare band dispersion $\varepsilon_{\mathbf{k}}$ is linear in momentum.

Given the above considerations, and the three most common self energy terms discussed in Section 2.4.1, we can see that the EDC quasiparticle peaks have a strictly Lorentzian shape if only impurity scattering is present. Electron-electron and electron-boson interactions both lead to more complex distributions of the spectral weight. Further complications arise in EDC lineshapes since the quasiparticle peaks can partly overlap with the incoherent spectral weight in the Fermi liquid, the secondary photoelectrons provide an energy-dependent background, and the Fermi function cuts off the spectrum in a temperature-dependent step. The EDC fits in this thesis were performed as a sum of Lorentzian quasiparticle peaks and a background of secondary electrons, multiplied by the Fermi function at the appropriate temperature, and convoluted with a Gaussian broadening of the instrumental energy resolution. An example is demonstrated in Figure 3.7b.

On the other hand, the interaction self energies discussed in Section 2.4.1 are all $\mathbf{k}$-independent, so to extract self energy parameters by Lorentzian
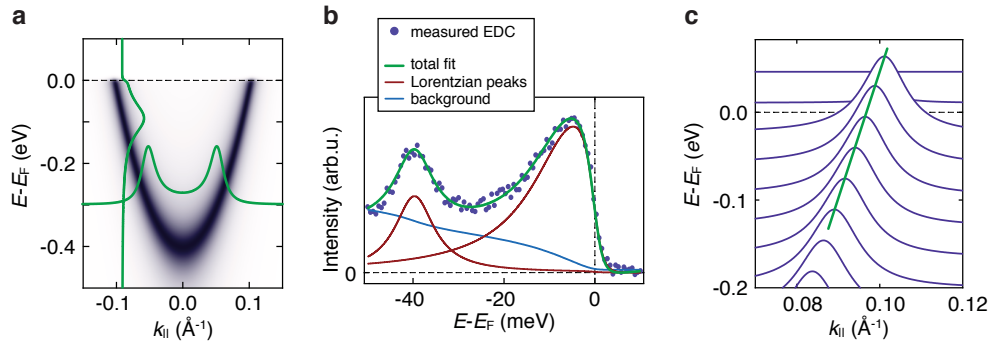
Figure 3.7: **ARPES data analysis. a** Example dispersion with extracted one EDC and one MDC. **b** A sample EDC line fit using Lorentzian peaks, an energy-dependent background and the Fermi function, convolved Gaussian broadening. **c** Lorentzian fits to MDCs near the Fermi level (purple), with the linear fit to the extracted peak positions in $k_\parallel$ (green).

peak fits to MDCs [44, 45, 86], we need to approximate the bare band dispersion as being linear[2]. The quasiparticle lifetimes can be extracted as $\Gamma(\omega) = v_0 \Gamma(k)$ when Σ is **k**-independent. The slope of the bare band, v_0, can be extracted from band structure calculations, e.g. from density-functional theory, which I describe below. By tracing the position of the peak for different energies, we can extract the experimental dispersion of a particular band. A linear fit to the dispersion at the Fermi level, as shown in Figure 3.7c yields directly the Fermi velocity, v_F, and the Fermi wavevector, k_F. The ratio of the measured Fermi velocity and the Fermi velocity of the bare band gives us an estimate of the strength of the interactions which are not already capture by the calculation.

In the case of constant-energy contours any one-dimensional cut is a momentum-distribution curve. To quantify the sizes and shapes of the Fermi pockets in maps, it is sometimes convenient to perform the line-fitting procedure on radial MDCs, centred in the pocket (usually at Γ). The integral of the pocket size then gives us the carrier concentration contributed by that Fermi pocket, and via Luttinger's theorem [125, 126], the filling of the corresponding band.

---

[2]When $\omega - \varepsilon(k)$, is linear in both ω and k, it can explicitly be rewritten into the form $k - k(\omega)$. The width of that Lorentzian in **k** is then: $\Gamma(k) = \Gamma(\omega)/\frac{\partial \varepsilon(k)}{\partial k}$.

3.2   Density-Functional Theory

Density-functional theory (DFT) provides a framework which makes solving large many-body quantum problems from first principles possible. The theory itself is completely general, and can be applied to any many-body system, be that an atom, a molecule, or a crystal. It is in principle set up as an exact theory, but in practice some assumptions and approximations need to be made in order to perform and interpret the calculations. In this Section, I will give a quick introduction to the basic principles of the theory and the common necessary approximations that are made in the calculations following a review by Capelle [127], and outline how the calculations are done in practice. Even though DFT has many uses, I will focus here on its application to electronic band structure calculations in crystalline solids.

3.2.1   Hohenberg-Kohn theorems

A quantum description of N electrons in a solid is typically given by the many-body Schrödinger equation [59]

$$\left[\sum_{i=1}^{N}\left(-\frac{\hbar^2}{2m}\nabla_i^2 + v(\mathbf{r}_i)\right) + \sum_{i<j}U(\mathbf{r}_i,\mathbf{r}_j)\right]\Psi(\mathbf{r}_1,...,\mathbf{r}_N) = E\Psi(\mathbf{r}_1,...,\mathbf{r}_N),$$

(3.7)

where the first term in the Hamiltonian represents the kinetic energy ($\hat{T}$), the second term represents a potential external to the electron sea ($\hat{V}$), i.e. electrostatic potential of the lattice in the Born-Oppenheimer approximation[3] and any applied external fields, and the third term is the electron interaction term from the Coulomb potential ($\hat{U}$). So, in an ideal case, we supply the external potential $v(\mathbf{r})$ for the desired system to Equation (3.7), solve the eigenproblem, and calculate any observable of the system using eigenfunctions Ψ. One such observable is the electron density,

$$n(\mathbf{r}) = N\int d\mathbf{r}_2 ... \int d\mathbf{r}_N \Psi^*(\mathbf{r}_1,...,\mathbf{r}_N)\Psi(\mathbf{r}_1,...,\mathbf{r}_N).$$

(3.8)

This approach has $3N$ variables, 3 coordinates for each electron, making it unwieldy in reality.

The first big breakthrough in forming the DFT approach came in the

---

[3]The Born-Oppenheimer approximation decouples the electronic system from the dynamics of the lattice, precluding *ab initio* inclusion of electron-phonon coupling in the calculation for a static $v(\mathbf{r})$. However, there are methods which can reintroduce it by hand at later stages of the calculation.

form of Hohenberg-Kohn theorems [128], which deal with that obstacle. The first theorem states that *the external potential $v(\mathbf{r})$ is a unique functional of the ground state electron density, $n_0(\mathbf{r})$* [127]. But this means that the full Hamiltonian is also a functional of the ground state density ($E[n_0(\mathbf{r})]$), and so all the properties of the system are determined by $n_0(\mathbf{r})$, along with all its many-body wavefunctions. However, the functional $E[n(\mathbf{r})]$ is not known within the formalism. What is known from the variational principle is the second theorem, which says that *the functional $E[n(\mathbf{r})]$ reaches a global minimum for, and only for the ground state electron density, $n_0(\mathbf{r})$* [127]. Excited states need to be calculated by other methods, making DFT a ground-state theory. Therefore, $\Psi_0(\mathbf{r}_1, ..., \mathbf{r}_N) = \Psi[n_0(\mathbf{r})]$, and the dimensionality of the problem is reduced from $3N$ to 3.

The formalism recognises that the total energy functional can be decomposed by the parts of the Hamiltonian in Equation (3.7) into a universal part, $F[n] = T[n] + U[n]$, which does not depend on the particular problem ($v(\mathbf{r})$), and a problem-specific part that does, $V[n]$. Furthermore, it separates $F[n]$ into two contributions. First holds the terms which are always known exactly, the non-interacting kinetic term, $T_s[n]$, and the Hartree (classical Coulomb) term, $U_H[n]$. The second contribution, on the other hand, combines the effects of exchange and correlation, which are not known exactly, into a single term $E_{xc}[n]$. The density functional for the total energy is then

$$E_v[n] = T_s[n] + U_H[n] + E_{xc}[n] + V[n], \tag{3.9}$$

and the variation of it with n yields the ground state energy E_0 for the minimising ground state density $n_0(\mathbf{r})$. The Hohenberg-Kohn theorems then guarantee that we can calculate any ground state observable, as they are all functionals of $n_0(\mathbf{r})$.

3.2.2 Kohn-Sham equations

Even though the variational problem set up by the Hohenberg-Kohn theory reduced the original $3N$- to a 3-dimensional form, we still do not know how to solve it explicitly. Minimisation of $E_v[n]$ is a non-trivial problem in general, and we still do not know explicit forms of the exchange-correlation functional, $E_{xc}[n]$. These problems are dealt with by the Kohn-Sham method [129]. In it, the original interacting many-body system in an external potential v (which we cannot solve) is replaced by an auxiliary non-interacting many-body system in an effective potential $v_{KS}(\mathbf{r})$ (which

we can solve). This is achieved by realising that Equation (3.9) can be rewritten as $E_v[n] = T_s[n] + V_{KS}[n]$, with the effective potential given as

$$v_{KS}(\mathbf{r}) = v_H(\mathbf{r}) + v_{xc}(\mathbf{r}) + v(\mathbf{r}), \qquad (3.10)$$

where $v_H(\mathbf{r})$ and $v(\mathbf{r})$ are the Hartree potential and the external potential of the system, respectively, and $v_{xc}(\mathbf{r})$ is an appropriately chosen approximate exchange-correlation potential for the ground state. We can then write the non-interacting single-particle Schrödinger equation:

$$\left[-\frac{\hbar^2}{2m} \nabla^2 + v_{KS}(\mathbf{r}) \right] \psi_i(\mathbf{r}) = \varepsilon_i \psi_i(\mathbf{r}), \qquad (3.11)$$

where ε_i and ψ_i are fictitious eigenvalues and wavefunctions of the auxiliary system, known as the Kohn-Sham energies and orbitals [127]. This procedure exactly solves the full many-body problem because the Kohn-Sham orbitals by construction reproduce the electron density of the original system as

$$n(\mathbf{r}) \equiv n_{KS}(\mathbf{r}) = \sum_i^N f_i |\psi_i(\mathbf{r})|^2, \qquad (3.12)$$

where f_i is the occupation number of ψ_i. Equations (3.10) to (3.12) are known as the Kohn-Sham equations [127, 129]. With them we have gone from describing the original system with the interacting many-body Schrödinger equation (3.7), via minimisation of the energy functional $E[n]$ in Equation (3.9), to solving a non-interacting Schrödinger equation with the Kohn-Sham potential. The equation is, however, non-linear, since v_{KS} depends on n_0, which depends on ψ_i, which depend on v_{KS}, and needs to be solved self-consistently.

For simplicity, I have described the basics of DFT for spinless, non-relativistic electrons. The theory can easily be expanded to include the spin of electrons by treating $n_\uparrow$ and $n_\downarrow$ as separate entities [127]. Relativistic effects can be fully included by substituting the Schrödinger for the Dirac equation, which properly includes spin-orbit coupling [127].

3.2.3   Approximations of DFT

There are three main types of approximations involved in solving the Kohn-Sham equations [127]. The first is conceptual, and concerns our interpretation of the Kohn-Sham energies and wavefunctions, i.e. how much real

physical meaning we ascribe to them. As I have stressed before, Kohn-Sham energies and orbitals are fictitious objects, purely mathematical constructs meant to help solve the original many-body problem. However, it turns out that they represent very good approximations for band energies and wavefunctions in the case of fermionic quasiparticles and no strong correlations [127]. This is precisely the approach of DFT band structure calculations for solids. The band energies are Kohn-Sham energies, ε_i, and the wavefunctions are Kohn-Sham orbitals, ψ_i. Taking this literal understanding of the Kohn-Sham eigenstates effectively turns DFT into a mean-field theory of the $v_{KS}(\mathbf{r})$ potential for non-interacting quasiparticles [127].

The second type of approximation is technical, and comes from the numerical precision of the specific code and algorithms used in the calculations [127]. As the Kohn-Sham equations are solved iteratively, on a discrete set of points in momentum space, enough points need to be included in order to ensure proper convergence of the calculation. The numerical precision of a correctly converged calculation mainly depends on the type of basis states that are chosen for the Kohn-Sham orbitals. A good choice for electrons in solids are augmented plane waves (APW) [130, 131]. They are constructed by dividing the space into atomic spheres, where the wavefunctions are atomic-like orbitals, represented by a linear combination of radial functions and their derivatives multiplied by spherical harmonics, and interstitial space where they are described by plane waves. With wavefunction matching at the sphere surfaces, this results in plane waves in the crystal, augmented by atomic-like orbitals within the spheres.

The third approximation is physical, and it involves constructing an approximate expression for the unknown exchange-correlation functional, $E_{xc}[n]$ [127]. Historically first, and still one of the most widely used, is the local density approximation (LDA) [128]. It assumes that energy density at any position $\mathbf{r}$ is that of a homogeneous ($n = \text{const.}$) system which has the electron density corresponding to the value of $n(\mathbf{r})$ at that position. This is tantamount to turning the exchange-correlation energy from a functional into a function of the electron density: $E_{xc}[n(\mathbf{r})] \rightarrow E_{xc}(n(\mathbf{r}))$. The LDA approximation separates the spatially inhomogeneous interacting problem into a spatially homogeneous interacting problem (the solution to which is known), and the spatially inhomogeneous non-interacting problem of the Kohn-Sham equations [127].

The generalised gradient approximations (GGA) were developed in order

to provide a semi-local treatment of the density [132]. They allow for the exchange-correlation energy to depend on its gradient as well as the value: $E_{xc}[n(\mathbf{r})] \rightarrow E_{xc}(n(\mathbf{r}), \nabla n(\mathbf{r}))$. In introducing the gradient-dependence, the GGA functionals offer an improvement over LDA, however, they lose a systematic cancellation of errors which is present in the LDA approach [127]. This means that making the choice on which one is more suitable often depends on the specifics of the system in question. Both approaches are known to underestimate band gaps in semiconductors, and more complex, hybrid functionals need to be employed in order to account for that.

3.2.4   Practical implementation

The program flow of any DFT code follows three basic steps. *i*) Initialisation, where the system under study is defined and the code calculates the initial guess for the electron density, $n(\mathbf{r})$. *ii*) The self-consistency cycle, in which the Kohn-Sham equations are iteratively solved. *iii*) Extraction of observables, in which the desired information about the system is calculated from the converged electron density. I present here the outline of these steps as implemented within the WIEN2k code [133–135], illustrated by the flowchart in Figure 3.8. I used this code to perform the calculations for the study of $Ca_3Ru_2O_7$ in Chapter 5, with the main results repeated and expanded on by Dr. Helge Rosner using the FPLO code [136], while all the DFT data for the study of NbGeSb in Chapter 4 was calculated by Dr. Matthew Dyer, using the VASP code [137].

The initialisation takes the crystal structure of the material whose band structure we want to calculate as input. The code will then deduce the symmetry elements of the structure, and use that information to reduce the computational cost of the calculation. We must then assign the type of magnetisation present in the system, if any, and, if we choose to include spin-orbit coupling, assign the direction in which it develops the magnetic moment. WIEN2k uses a fully relativistic approach for the core electrons, and a second variational method for the valence electrons, including the spin-orbit coupling [133–135]. The code can then solve the atomic Schrö-dinger equation for the atoms in the crystal, getting their atomic electron densities, whose superposition is used as the initial guess for $n(\mathbf{r})$ in the self-consistency cycle. There, the Kohn-Sham equations will be converged for a discrete set of points in the momentum space, the $\mathbf{k}$-mesh of the calculation. We must choose the point-density of the $\mathbf{k}$-mesh, keeping in mind
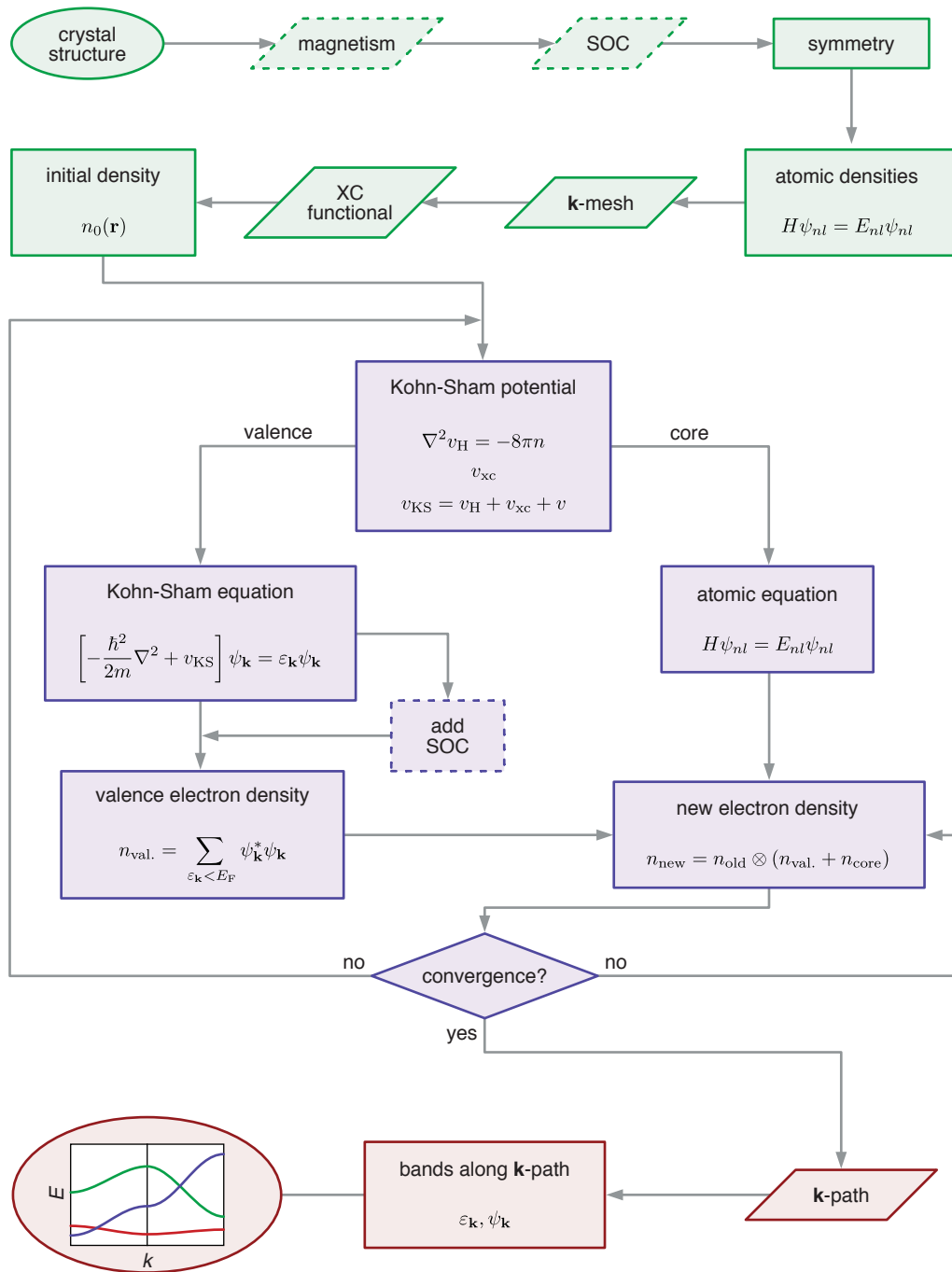
Figure 3.8: **Program flow of the WIEN2k code.** An algorithmic representation of the: initialisation (green), self-consistency cycle (purple), and band structure extraction (red) within the WIEN2k code. Adapted from the WIEN2k manual [135].

that if the mesh is too sparse, the calculation might not converge properly (if it converges at all), while if there are too many $\mathbf{k}$-points, the calculation will take an impractically long time to perform. Symmetries help us here as well, making it enough that the calculation is performed only on the irreducible wedge of the Brillouin zone. Finally, we must choose which approximation for the exchange-correlation functional will be used in the calculation. These considerations will prove important for the conclusions drawn from DFT calculations in the study of $Ca_3Ru_2O_7$ in Chapter 5.

Within the self-consistency cycle, n is first used to calculate the components of the effective Kohn-Sham potential. The Hartree (classical Coulomb) term is calculated using the Poisson equation, $\nabla^2 v_H(\mathbf{r}) = -8\pi n(\mathbf{r})$, and the correlation-exchange potential, $v_{xc}(\mathbf{r})$, is determined according to the chosen approximate potential. WIEN2k separates the core and valence electrons, treating core electrons using the atomic Schrödinger equation, and the valence electrons using the Kohn-Sham equation [133–135]. Separate electron densities for valence and core electrons are thus obtained from the eigenstates in the two cases, as illustrated in Figure 3.8. These are added together, and combined with the total electron density from the previous iteration, resulting a new value for $n(\mathbf{r})$. If predetermined convergence criteria are met, the code exits the cycle, and if not, it feeds the new density as the starting point of another iteration. We can also choose to allow the crystal structure to relax at this stage by minimising the forces on the atoms as one convergence criterion. This obviously means that the external potential is no longer kept fixed, but is also changed with each iteration, and a stable configuration of the atoms is obtained self-consistently.

Once the calculation has converged, we can proceed with obtaining the electronic band structure [133–135]. In order to do this, we need to specify the exact path in momentum space along which this should be done, typically some sequence of high-symmetry lines of the Brillouin zone. The code then extracts both the eigenvalues as band energies, and the details of the eigenvectors as wavefunctions with an atomic-orbital weight decomposition, for each $\mathbf{k}$-point along the desired path. This results in the famous "spaghetti"-plots of the band structure. As another calculable observable of interest for the electronic structure of solids, the total or partial densities of states can also be obtained at this point.

Slab calculations

By using the unit cell of the crystal structure as input for the calculation, only bulk electronic states can be obtained in the end. In order to get information on the surface states of materials, special structural unit cells need to be made [138]. We use slabs of several crystal-unit cells in thickness with a vacuum layer above the surfaces in the out-of-plane directions. This results in super-cells, which are still periodic in the out-of-plane direction, but with the vacuum layers between the slabs guaranteeing there is no overlap of electronic states between the slabs. In these cases, the surface crystal structure should always be allowed to relax, as there will typically be some degree of structural reconstruction present at crystal surfaces. Performing a DFT calculation with such slabs as structural units will yield surface states in the electronic structure, and they can easily be identified in the band structure as bands which have considerable projection onto atoms in the surface layers of the slab.

In the following two Chapters, I lay out my results on the studies of the electronic structures of NbGeSb and $Ca_3Ru_2O_7$, obtained by the methods described above.

4 | Protected band crossings in NbGeSb

In this Chapter I will present my results on investigating the band structure of NbGeSb, a material with weak electron interactions, and strong effects arising from spin-orbit coupling. It belongs to a family of materials known to host multiple protected crossing points and nodal lines in their band structure. My results will identify topological features in the band structure which are common to the materials of this family, but also some which have been observed for the first time in NbGeSb, notably two-dimensional Weyl-like crossing points of spin-split surface states. To help navigate the rich terminology of topological semimetals and clarify the terms which I use, I will first give a brief general introduction to topologically protected band crossings in electronic structures, with a focus on layered square net materials, relevant for NbGeSb.

4.1   Protected crossings in band structures

The physical models of elementary particles in the high-energy regime have been known to show some remarkable similarities to the models of low-energy excitations of quasiparticles in condensed matter systems [139]. Recent popular examples include the realisations of Dirac and Weyl fermions in the electronic structure of solids [11, 140, 141]. Dirac developed his famous equation as a relativistic extension of the Schrödinger equation [142, 143] for electrons. Its Hamiltonian is a 4×4 matrix which acts in the space of four-component spinors. It yields solutions for both the particle and the anti-particle, each with two spin states, i.e. four states in total. The equation generally has a mass term which gaps the spectrum at zero energy, separating the particle and anti-particle solutions.

Hermann Weyl modified the equation for massless electrons, eliminating two of the solutions in Dirac's formalism [144]. This results in an equation describing two singly degenerate, linearly dispersing states, bearing opposite spin. The Weyl Hamiltonian is therefore a 2×2 matrix simply given by [11,

144]:

$$H = \pm c\, \mathbf{p} \cdot \boldsymbol{\sigma}, \tag{4.1}$$

where c is the velocity of the particles (speed of light for massless particles), $\mathbf{p}$ is their momentum, and $\boldsymbol{\sigma}$ are the Pauli matrices, representing the two spin states. The sign at the front of the Hamiltonian determines the chirality of the solutions. Two pairs of Weyl states of opposite chirality can be combined to give the four states of the Dirac equation. In the condensed matter equivalent, the symmetries of a crystal allow for different velocities, $\mathbf{v}$, and we can write [11, 12]:

$$H \propto v_x k_x \sigma_x + v_y k_y \sigma_y + v_z k_z \sigma_z, \tag{4.2}$$

where $\mathbf{k}$ now represents the crystal momentum. Any 2×2 matrix can be written as a linear combination of the Pauli matrices [11, 59], and the Weyl Hamiltonian uses all of them[4] to define the dispersion of the bands. As such, adding any small perturbation will only change the position of the degeneracy of the two states in momentum space, but cannot completely remove it. Such protected crossings of bands in the electronic structure, described by the Weyl equation, are called Weyl points [11, 140, 141].

The same conclusion is found in general analysis of electron energy eigenvalue degeneracies in crystals [145, 146]. The energy gap of any two singly degenerate states is determined by three independent parameters of the corresponding two-state Hamiltonian. Three independent conditions (one for each Pauli matrix component) therefore need to be satisfied in order for the gap to close. If all three conditions are accidentally satisfied at an arbitrary point in momentum space, the two bands will be degenerate there, and can locally be described by the Weyl Hamiltonian in Equation (4.2). This means that the three conditions are satisfied by the three momentum-space coordinates of the degeneracy, and that any small perturbation will only change those coordinates, but will not lift the degeneracy. Such accidental crossing points of singly degenerate states in condensed matter are indeed topologically equivalent to the Weyl-fermion description, and are shown to be singularities of the Berry curvature, carrying topological invariants [147]. As a consequence, the pseudospin $\boldsymbol{\sigma}$ has non-trivial winding around the Weyl point, with the winding number representing the topological invariant, and

---

[4]The fourth basis matrix is the 2×2 identity matrix, which only provides a uniform energy offset to the Hamiltonian, and therefore bears no effect here.

corresponding to the chirality of the high-energy equation [11].

The analogy goes further, as two Weyl points of opposite chirality can be merged with each other at a high-symmetry line, creating a single Dirac point, a fourfold-degenerate crossing of two spin-degenerate bands described by the Dirac equation [11, 140]. As in the high-energy case, the fact that there are now four states in the system allows for a mass term to develop, which will generically gap the Dirac point, unless a symmetry protects it. Symmetry protection of band degeneracy occurs at symmetry-invariant points in the Brillouin zone, if the two bands belong to different irreducible representations of that symmetry. The bands are then orthogonal and hybridisation is prevented [76, 77].

In general, therefore, band degeneracies in condensed matter are protected by [11]:

i) symmetry - when they are completely pinned in momentum space by symmetry elements,

ii) accidental tuning of the parameters - occurring at an arbitrary place in momentum space,

iii) a combination of the two - where some of the coordinates in momentum space are pinned by symmetry while others can be tuned to achieve band degeneracy.

Only Weyl points represent purely accidental degeneracies, while Dirac points require some level of symmetry protection.

There are two main ways for symmetry to stabilise a Dirac point in condensed matter. Following a review by Armitage, Mele and Vishvanath [11], I will refer to them as "band-inverted" and "symmetry enforced" Dirac points. I illustrate band inversion in Figure 4.1, as a process where tuning a parameter of the system drives two bands of opposite parity to partially overlap. We start with two well separated, spin-degenerate bands of opposite parity in Figure 4.1a, describing a topologically trivial band insulator. Closing the gap between the two bands, the system goes through a quantum critical point between the trivial and a topological phase, with a semimetallic dispersion where the two bands touch in a single Dirac point, as in Figure 4.1b. Driving the band overlap further, the bands cross through each other, and in a generic case they hybridise [145], leaving them with sections of inverted band character [9, 10, 148–151] as seen in Figure 4.1c.

The resulting insulating state is topologically non-trivial, and describes a schematic of the standard $\mathbb{Z}_2$ topological insulators (TI) [152, 153]. As a
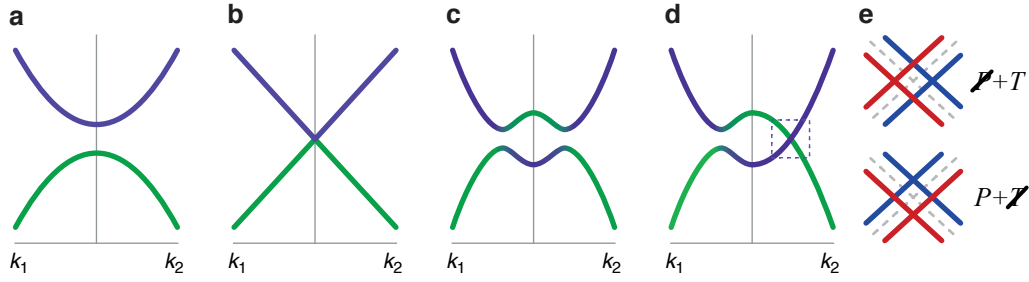
Figure 4.1: **Band inversion.** Two bands with opposite parity (green and purple lines) can be made to overlap by tuning a parameter of the system, driving the system between different regimes. **a** Topologically trivial insulator. **b** Bands touching at the quantum critical point between a trivial and a topological insulator. **c,d** Fully gapped finite band overlap leading to **c** a topological insulator, or **d** a semimetal if the crystal symmetries protect band crossings along certain high-symmetry lines (e.g. k_2, but not k_1), resulting in a Dirac point. **e** A schematic of a Dirac point splitting into two Weyl points if time-reversal or inversion symmetry is broken.

result of the bulk-boundary correspondence [154], topological surface states bridge the bulk projected gap, connecting the topological insulator in the bulk of the material with the trivial insulator (vacuum) on the outside. The inverted bulk bands do not necessarily hybridise at every momentum point though. Symmetry elements present in the Brillouin zone can prevent the hybridisation [155, 156], as illustrated in Figure 4.1d. In the illustrated case, the crossing point is pinned to a specific high-symmetry line, however, its position along that line is determined by the microscopic details for the system and therefore accidental. In special cases, the protected crossing can form a line instead of a single point, which is then known as a nodal line. [11, 140, 141].

If the material is time-reversal and inversion invariant, it can in principle host Dirac, but not Weyl points. When one of those symmetries is broken, the bands split by spin, and the Dirac points split into two Weyl points of opposite chirality [11, 140, 141]. This is schematically illustrated in Figure 4.1e. By construction of the band inversion mechanism, we see that all the induced crossing points can be removed if we un-invert the bands by simply tuning a parameter, without ever breaking any symmetries of the Hamiltonian.

The symmetry enforced Dirac points, on the other hand, represent the set of bulk band degeneracies which cannot be removed without breaking some fundamental symmetry of the Hamiltonian [11]. They occur when the space group of the crystal structure requires by symmetry that a de-

generacy point be present in the band structure, which is only possible in nonsymmorphic space groups [11, 157, 158], described below.

4.2   Nonsymmorphic symmetries and square nets

Nonsymmorphic symmetries, $\{g|\mathbf{t}\}$, are a combination of a point symmetry element, g, i.e. a mirror plane, M, or a rotation axis, C, with a translation, $\mathbf{t}$, by a fraction of the Bravais lattice vector resulting in a glide plane or a screw axis, respectively (e.g. Figure 4.2a,b). It has long been known that nonsymmorphic symmetries make bands "stick" together at the edges of the Brillouin zone as a result of the fractional translations [77, 158, 159]. The nonsymmorphic symmetries increase the size of the unit cell as compared to the underlying symmorphic structure by the factor of the fractional translation. This increases the number of the basis atoms in the unit cell, and reduces the size of the Brillouin zone by the same factor. Each atom in the unit cell now contributes an identical band in momentum-space to the original one (Figure 4.2c), offset by a phase factor given by its displacement $\mathbf{t}_i$ from the origin.

I illustrate how this is realised on an example of a simple 1D chain, by introducing a glide-mirror plane $\{M_z|\frac{1}{2}00\}$ in Figure 4.2a and a fourfold screw axis $\{C_{4,x}|\frac{1}{4}00\}$ in Figure 4.2b. The $\{M_z|\frac{1}{2}00\}$ glide-mirror creates two bands in anti-phase in the new Brillouin zone, while the screw axis $\{C_{4,x}|\frac{1}{4}00\}$ creates four bands with successive $\pi/2$ phase shifts, as shown in Figures 4.2d and e, respectively. This generically creates band touch-
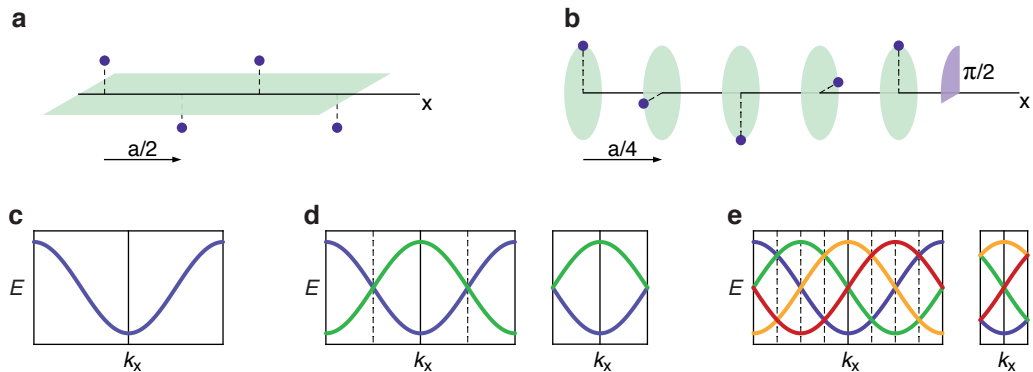

Figure 4.2: **Nonsymmorphic symmetries and band structure. a** A glide-mirror plane $\{M_z|\frac{1}{2}00\}$, and **b** a screw axis $\{C_{4,x}|\frac{1}{4}00\}$ are illustrated on a 1D atomic chain. The cosine band of a simple 1D chain (**c**) is transformed by the glide plane (**d**) and the screw axis (**e**), causing symmetry enforced crossings at the new Brillouin zone edges.
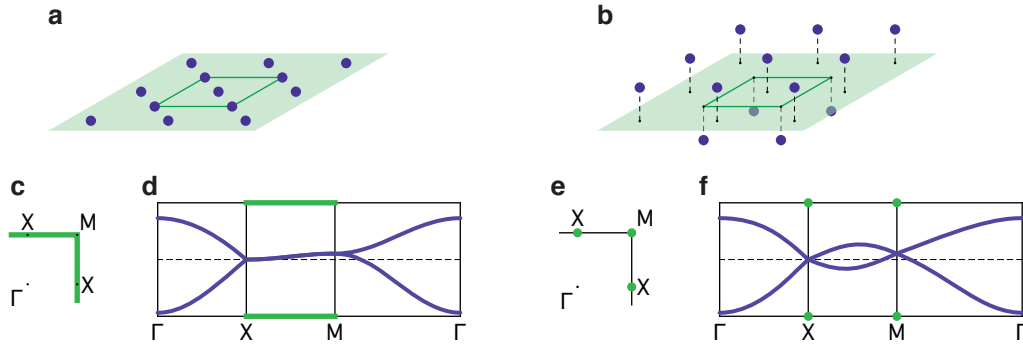
Figure 4.3: **The Young and Kane model. a** Two-dimensional square lattice hosts two basis-atoms in the indicated $\sqrt{2}\times\sqrt{2}$ unit cell. **b** A non-symmorphic bilayer created by offsetting the two different basis atoms from the lattice in **a** by z and $-z$, respectively. **c**–**f** The resulting respective Brillouin zones (**c**, **e**) and band structures (**d**, **f**), with the high-symmetry points hosting the enforced band degeneracy highlighted in green. The figure has been adapted from Young and Kane [161].

ing points at the edges of the nonsymmorphic Brillouin zone, as seen in Figure 4.2d,e, built into the symmetry of the Hamiltonian of the system.

This process can equivalently be described by "backfolding" the original band along the dashed lines, the edges of the nonsymmorphic Brillouin zones indicated in Figure 4.2d,e, making it clear that the states which are exactly on the dashed line will not move and will therefore be common for both new bands [77, 158, 160]. These effects can be seen in square net structures, which are of particular importance for NbGeSb (as well as of some relevance for layered perovskite structures discussed in Chapter 5).

Crystal structures in condensed matter come in many structural forms, and different models can be used to better illustrate the relevant constituting elements such as clusters [162], polyhedra [163], or 2D nets with various vertex connectivity (e.g. square, triangular, honeycomb and kagome 2D lattices) [160]. Even though multiple descriptions might mathematically be applicable to the same structure, a particular choice is usually made which most naturally explains the connection of the structure to the resulting physical phenomena. In Chapter 5 that will be the polyhedral description, while here I will focus on the layered nets, in particular square atomic nets.

A simple square lattice extends the cosine band from 1D in the tight-binding example of Section 2.1 into two dimensions as $E \propto \cos(k_x a)\cos(k_y b)$. However, this 2D plane can combine with other structural elements in real crystals, which often establish the true unit cell to be $\sqrt{2}\times\sqrt{2}$, with a 45° rotation compared to the primitive square unit cell, as illustrated in Fig-

ure 4.3a. The Brillouin zone is then half the size, also with a 45° rotation, as can easily be seen from a band "backfolding" construction where the corners of the simple BZ are folded back onto its centre [158, 160]. The two basis atoms of this unit cell are connected by a $(\frac{1}{2}\frac{1}{2}0)$ fractional translation, causing the bands to stick together along the entire Brillouin zone boundary as in the nonsymmorphic examples above, protected by the $\{E|\frac{1}{2}\frac{1}{2}0\}$ symmetry [161], where E is the identity. The position and appearance of the protected nodal lines are shown in Figure 4.3c,d.

Such square net layer can be made nonsymmorphic by offsetting the two basis atoms in the layer by $\pm z$, in the opposite directions perpendicular to the crystal plane, illustrated in Figure 4.3b. This generates a glide-mirror plane $\{M_z|\frac{1}{2}\frac{1}{2}0\}$, and two screw axes: $\{C_{2,x}|\frac{1}{2}00\}$ and $\{C_{2,y}|0\frac{1}{2}0\}$, which all together protect the degeneracies at the high-symmetry points on the Brillouin zone edge (X and M) [161], as indicated in Figure 4.3e,f. Dirac points at X and M generated in this way are symmetry enforced, and protected against gapping even when spin-orbit coupling is introduced.

4.3   Layered square nets

The two types of square nets presented in Figure 4.3a,b can be used as building blocks which generate the NbGeSb crystal structure (space group $P4/nmm$, #129 [164, 165]) shown in Figure 4.4a. This structure is generally know as the PbFCl-, or ZrSiS-type structure, and is very versatile, capable
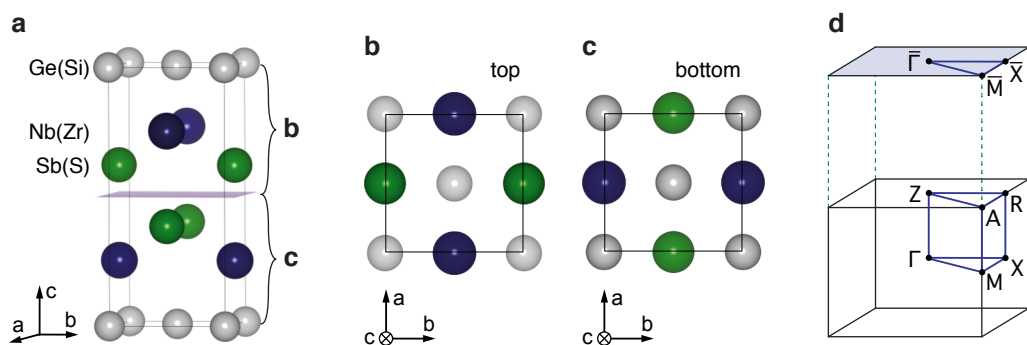

Figure 4.4: **NbGeSb crystal structure.** **a** The ZrSiS-type structure, space group $P4/nmm$, # 129, in which NbGeSb crystallises. The middle of the unit cell holds the glide-mirror plane of the nonsymmorphic bilayers which connects **b** the top half of the unit cell to **c** the bottom half. The optimal cleavage plane coincides with the glide-mirror plane shown in **a** leaving only **b** or **c** as the crystal termination. **d** The corresponding bulk, and *c*-axis surface projected Brillouin zones.
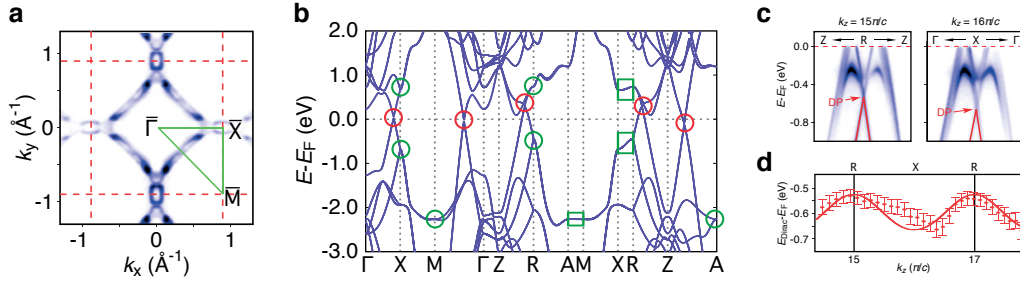
Figure 4.5: **Bulk ZrSiS electronic structure. a** Fermi surface of ZrSiS. **b** The bulk band structure of ZrSiS calculated by DFT along the indicated path in the Brillouin zone (Figure 4.4d). The red circles denote the Dirac points which form the square nodal line at the Fermi level, and gap with spin-orbit coupling. The green circles denote the enforced Dirac points, which form nodal lines in k_z indicated by the green squares. **c** Measured Γ–X and Z–R dispersions with the indicated position of the enforced Dirac point. **d** From such measurements at different k_z values, the enforced Dirac point is found to disperse with k_z. The **a**,**c** and **d** panels are adapted from Chen *et al.* [167], and the **b** panel from Su *et al.* [168].

of hosting large variations in chemical composition [160, 166]. It is built of two nonsymmorphic bilayers, of the type described in Figure 4.3b, and a $\sqrt{2}\times\sqrt{2}$ square net layer from Figure 4.3a. The nonsymmorphic bilayers are arranged so that they share the same glide-mirror plane, indicated in the middle of the unit cell of Figure 4.4a, with a bilayer of main group element atoms (Sb or S in Figure 4.4) enclosed between the two layers of the transition metal bilayer (Nb or Zr in Figure 4.4). These are then stacked along the c axis alternating with a $\sqrt{2}\times\sqrt{2}$ square net layer of another main group element (Ge or Si in Figure 4.4). This means that the $\{M_z|\frac{1}{2}\frac{1}{2}0\}$ glide plane of the nonsymmorphic bilayers is inherited by the bulk space group, and it connects the top and bottom halves of the unit cell, as can be seen by their c-axis view in Figure 4.4b and c, respectively.

Some band structure features are also directly inherited from these two-dimensional square net building blocks, both in the bulk and the surface projected Brillouin zone, shown in Figure 4.4d. In real materials, multiple orbitals present at each site of the square net result in multiple bands. Backfolding of these bands in the $\sqrt{2}\times\sqrt{2}$ unit cell can lead to crossings between different bands somewhere in the Brillouin zone [160, 166]. This crossing is generically not symmetry enforced and gaps with spin-orbit coupling, however, charge compensation can pin it to the Fermi level where it forms a nodal line. This has attracted much attention in ZrSiS, where such nodal lines are the only bulk states at the Fermi level, as seen in Fig-
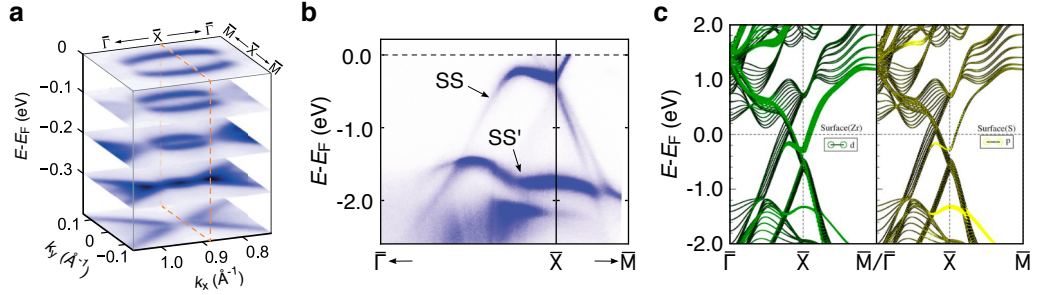
Figure 4.6: **Surface ZrSiS electronic structure. a** The elliptical surface state Fermi pocket seen at $\overline{\mathrm{X}}$ in Figure 4.5a is shown in constant energy contours, from Chen *et al.* [167], shrinking to a point with binding energy. **b** The two surface states are identified in ZrSiS in Topp *et al.* [178], shown along the high-symmetry lines in the vicinity of the $\overline{\mathrm{X}}$ point. **c** Slab DFT calculations in Su *et al.* [168] identify the orbital character of the two surface states from **b**.

ure 4.5a,b, making it a bulk Dirac nodal line semimetal [166, 169, 170] with clear signatures in transport measurements [168, 171–177]. The symmetry enforced Dirac crossings at the edges of the zone, introduced in Figure 4.3, are also preserved in three dimensions. In fact, since these nonsymmorphic symmetry elements are present at every value of the out-of-plane momentum, the Dirac points at X and M in 2D become nodal lines in 3D, along the k_z direction (along X–R and M–A in the 3D Brillouin zone) [166, 167, 169], as demonstrated in Figure 4.5c,d.

These materials also exhibit interesting behaviour at the surface of the crystal. Reportedly, the most stable *c*-axis termination is along the glide plane indicated in Figure 4.4a [168, 169, 179]. The nonsymmorphic symmetry of the bulk is therefore broken at the surface, since the bilayer building blocks are not complete in the surface half-unit cell (Figure 4.4b,c). This loss of nonsymmorphic symmetry allows the surface states to unpin from their bulk counterparts along the entire zone edge and disperse within the bulk projected band gap closer to the Fermi level [178]. Two such surface states were predicted and observed in ZrSiS [167–170, 178], as seen in Figure 4.6b. One of them, SS, is derived from the transition metal *d* states (Zr) [168, 178] (Figure 4.6c) and is mainly unoccupied, only crossing the Fermi level at the X point, and creating a simple elliptical electron-like Fermi surface pocket in Figure 4.6a. The other, SS′, mainly comes from the nonsymmorphic main group element layer (S) [168] (Figure 4.6c), and remains well below the Fermi level in the entire Brillouin zone.

Isovalent substitution of Hf for Zr increases considerably the strength of

spin-orbit coupling on the transition metal site, leading to a substantially increased spin splitting in the SS state, which originates from electrons on that site. As a result of that, the SS surface state, as well as its Fermi surface, develop considerable spin splitting via the Rashba mechanism enabled by the inversion symmetry breaking at the surface [167, 180] (Section 2.2).

NbGeSb represents another isostructural chemical substitution option. It would again be expected to host considerably stronger spin-orbit coupling [160, 165] as compared to ZrSiS, now on all three atomic species. However, the substitution here is aliovalent, with Nb having one electron more than Zr, and Sb one electron less than S. The total charge count is still the same, so we expect global charge compensation, but with a possibility of considerable energy shifts of both bulk and surface state bands. In the surface band structure, this is expected to manifest as lowering of the Nb-derived SS band in energy, and raising of the Sb-dominated SS′ band (which is fully occupied in ZrSiS) to cross the Fermi level. The substitution however violates the charge count requirements for the nodal line to be the only bulk states at the Fermi level, and introduces a significant bulk density of states to the Fermi level.

4.4   Methods

To study the electronic structure of NbGeSb with ARPES experiments, I used high-quality single crystals grown by Prof. Jonathan Alaria and his student, Keiron Murphy, at the University of Liverpool (Figure 4.7a). The samples were grown by chemical vapour transport in a quartz tube filled in an argon atmosphere and sealed under vacuum, using iodine as the transport agent [179]. The x-ray scattering data in Figure 4.7b show the crystals to be of very high quality. Materials in this family reportedly cleave along the glide-mirror plane indicated in Figure 4.4a [168, 169, 179], which leaves an Sb-terminated surface in NbGeSb. I have empirically found that $\sim 90\ \%$ of the cleaves on our samples are consistent with that cleaving plane. The remaining 10 % of the cleaves have not shown the recognisable "floating" [178] surface states in ARPES measurements, which implies that they leave the nonsymmorphic bilayers intact in the surface layer, most likely cleaving at the Ge layer. Unless explicitly mentioned, the presented data comes form the "standard", Sb-terminated cleaves.

Spin-integrated ARPES data, unless stated otherwise, was all measured at the CASSIOPEE beamline [120] of the Soleil synchrotron in France. Some
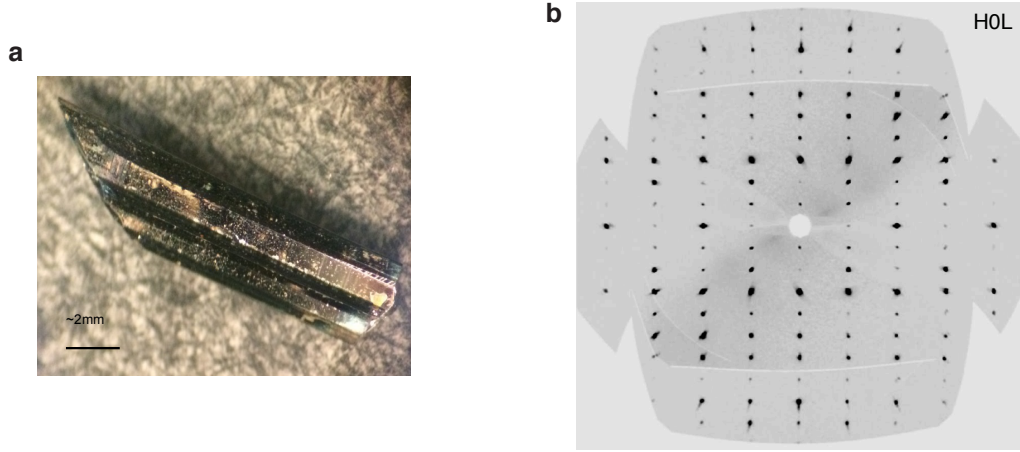
Figure 4.7: **High-quality NbGeSb single crystals. a** Image of a typical NbGeSb single crystal, and **b** the accompanying x-ray diffraction pattern data.

data were also collected at the SIS beamline [121] of the SLS synchrotron at the Paul Scherrer Institute in Switzerland. There, the horizontal orientation of the ARPES analyser entrance slit provides a different experimental geometry, and hence different conditions on the matrix element modulation of the measured photoemission intensity. Spin-resolved ARPES data were gathered at the APE beamline [110, 122] of the Elettra synchrotron in Italy, and the BL-9B beamline [108, 109, 123] of the HiSOR synchrotron in Japan. Both facilities use double VLEED detectors described in Section 3.1.2. The Sherman function, and the absolute orientation of the measured spin polarisation of the bands, was determined by me for the Elettra data by performing and analysing measurements on the known Au(111) Rashba spin-split surface states [65, 66, 181]. At HiSOR this normalisation procedure was performed by the beamline staff, using Bi(111) surface states [108, 109].

It is worth noting that the NbGeSb samples show deterioration in the quality of the acquired photoemission data over relatively short time scales, even in ultra-high vacuum conditions. We have observed noticeable broadening of the ARPES features after ~ 6 hours at the SIS and APE beamlines, and after ~ 8–12 hours at the BL-9B and CASSIOPEE beamlines.

To help with the interpretation of the photoemission data, Dr. Matthew Dyer and his student, Philip Murgatroyd, at the University of Liverpool performed a series of DFT band calculations both for the bulk and slab geometry of NbGeSb. The calculations were done using the VASP code [137], using the PBE exchange-correlation functional [132] with inclusion of spin-orbit coupling [182]. Starting from the experimental values, the bulk crystal

structure was first allowed to relax self-consistently on a $20 \times 20 \times 9$ **k**-mesh until all forces fell below 0.001 eV/Å. A 5-unit cell thick slab was created by taking seven unit cells of the relaxed bulk structure, and removing two in a way that created a symmetric slab, terminated by Sb layers on either side. The structure was then further relaxed on a $20 \times 20 \times 1$ **k**-mesh until all forces again fell below 0.001 eV/Å, resulting in relaxed periodic images of the slab, separated by a vacuum region of 18.36 Å. All properties of the band structure were then extracted non-self-consistently along the desired **k**-paths.

Further understanding of the surface state crossing structure, as well as the chiral texture of the bands near the crossing points, described in Section 4.7, was gained through a tight-binding calculation performed by Dr. Chris Hooley, developed through a series of collaborative discussions. The model is based on the five Nb $4d$ bands, each with two possible spin projections, and is built in three parts as:

$$H = H_0 + H_{\mathrm{R}} + H_{\mathrm{SO}}.$$

We first construct a spin-independent model, H_0, using the symmetry elements of the NbGeSb Brillouin zone (C_4 rotational symmetry, M_x and M_y mirror symmetries, and time-reversal symmetry)[5] to constrain the allowed hopping form factors. Employing only relatively near-neighbour form factors: $c_+ \equiv \cos k_x + \cos k_y$; $c_- \equiv \cos k_x - \cos k_y$; $s_x \equiv i \sin k_x$; $s_y \equiv i \sin k_y$; and $s_{xy} \equiv \sin k_x \sin k_y$, the model Hamiltonian becomes:

$$H_0 = \begin{pmatrix} \Delta_1 + t_1 c_+ & t_2 c_- & t_3 s_y & t_4 s_{xy} & t_3 s_x \\ t_2 c_- & \Delta_2 + t_5 c_+ & t_6 s_y & 0 & -t_6 s_x \\ -t_3 s_y & -t_6 s_y & \Delta_3 + t_7 c_+ + t_8 c_- & t_9 s_x & t_{10} s_{xy} \\ t_4 s_{xy} & 0 & -t_9 s_x & \Delta_4 + t_{11} c_+ & -t_9 s_y \\ -t_3 s_x & t_6 s_x & t_{10} s_{xy} & t_9 s_y & \Delta_3 + t_7 c_+ - t_8 c_- \end{pmatrix},$$

where the parameters $\Delta_1 = \Delta_2 = -1$, $\Delta_3 = \Delta_4 = 0$, $t_1 = -0.5$, $t_2 = -0.75$, $t_3 = t_4 = t_5 = t_6 = -1$, $t_7 = 0.75$, $t_8 = 0.25$, $t_9 = 1$, $t_{10} = 0.3$, and $t_{11} = 0.5$ were chosen arbitrarily. Spin-orbit coupling is then added to the model in two steps, as H_{R} and H_{SO}. Even though they originate from the same microscopic effect, we find it convenient to separate the spin-orbit

---

[5]The M_z mirror symmetry is not enforced, reflecting the surface nature of the bands in the model.

interaction into an inter-unit cell Rashba term, $H_{\mathrm{R}} = \alpha_{\mathrm{R}}\hat{\mathbf{z}} \cdot (\mathbf{S} \times \mathbf{k})$, and the intra-unit cell atomic spin-orbit term, $H_{\mathrm{SO}} = \alpha_{\mathrm{SO}}\mathbf{L} \cdot \mathbf{S}$ which is taken as $\mathbf{k}$-independent [183]. The terms are included with respective weights of $\alpha_R = 0.2$ and $\alpha_{\mathrm{SO}} = 0.02$.

These will help us in the understanding of the electronic structure of NbGeSb presented below.

4.5   NbGeSb band structure overview

Figure 4.8 shows the band structure of NbGeSb obtained from our ARPES measurements (Figure 4.8a,b) and DFT slab calculations (Figure 4.8c–e), from which we can immediately see the similarity in the main features.
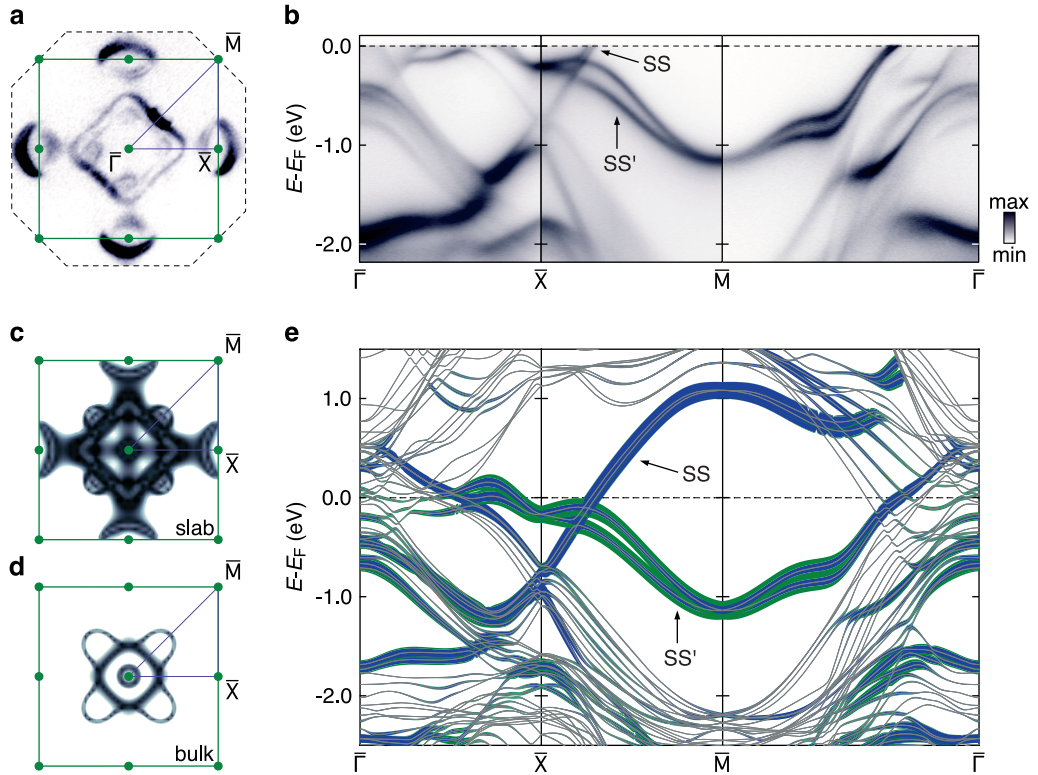

Figure 4.8: **NbGeSb band structure overview. a,b** Experimental band structure of NbGeSb, from ARPES measurements. **a** Fermi surface, measured with p-polarised 120 eV photons. **b** Dispersions along the high-symmetry lines, measured using 65 eV photon energy. The dispersions are a sum of measurements using circular left (CL) and circular right (CR) light polarisation. **c–e** Equivalent plots of the band structure, calculated using DFT. The Fermi surface is shown for calculations in both the slab (**c**), and bulk (**d**) geometry. **e** Dispersions were calculated in the slab geometry, with the coloured width of the lines representing the weight of the eigenstates projected onto the surface Nb (blue) and surface Sb (green) atomic layers.

Figure 4.8a shows the measured Fermi surface. We can see a square Fermi surface centred at the $\overline{\Gamma}$ point, as well as elliptical Fermi pockets around the $\overline{X}$ points, reminiscent of the ZrSiS Fermi surface (Figure 4.5a). Figure 4.8c,d are DFT calculated Fermi surfaces, for a slab configuration which includes surface state contributions, and for a bulk calculation, respectively. We can see that the square Fermi surfaces at the Brillouin zone centre are significantly more structured in NbGeSb than in ZrSiS, i.e. there are two concentric square pockets, the larger one being mainly derived from surface states. The bulk Fermi surface is composed of the smaller square pocket, a "cross"-shaped pocket with its "petal"-like ends pointing towards the $\overline{M}$ point, and a small round pocket just around $\overline{\Gamma}$. The "petals" of the bulk states cross through the surface state square pocket along the $\overline{\Gamma}$–$\overline{M}$ which can be seen both in the slab calculation of the Fermi surface and in the measured ARPES data as sectioning and outward bowing of the sides of the large square pocket close to the indicated $\overline{\Gamma}$–$\overline{M}$ line.

This can also be seen from the dispersions of the bands along the indicated high-symmetry lines of the Brillouin zone measured by ARPES in Figure 4.8b and calculated by slab-DFT in Figure 4.8e. The slab calculation in Figure 4.8e also shows the surface character of the calculated bands as coloured widths of lines, with blue representing the surface Nb, and green representing the surface Sb character of the bands. The small circular bulk Fermi pocket is best seen in the ARPES dispersions as a hole-like band crossing the Fermi level closest to $\overline{\Gamma}$. The "cross" bulk Fermi surface comes from an electron-like band around the Brillouin zone centre, seen in the measured $\overline{\Gamma}$–$\overline{X}$ dispersion as the second band crossing the Fermi level from $\overline{\Gamma}$. The slab calculation along the $\overline{\Gamma}$–$\overline{M}$ line clearly shows an electron-like bulk band being the one crossing the Fermi level furthest away from the $\overline{\Gamma}$ point, representing the "petal" of the "cross" Fermi surface.

The projected surface weight of the bands in the DFT calculation helps us distinguish the bulk and surface states in the measured data. We can see in Figure 4.8e that a lot of the surface weight in the band structure occurs within the bulk band manifolds, indicating they are surface resonances with significant extent of the wavefunction into the bulk. For example, the large square Fermi surface is made by surface states that have become resonant with the bulk bands, which in turn make the smaller, bulk square Fermi surface. There are two pairs of surface states though, which disperse in the bulk-projected band gap, completely separated from the bulk bands. These
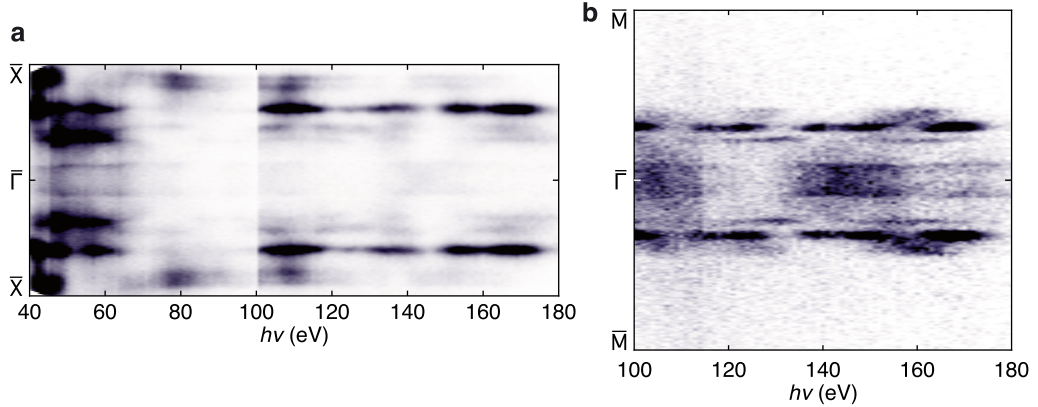
Figure 4.9: **Photon energy dependence of the Fermi surface.** Photon energy dependence of the bands at the Fermi level, along the **a** $\overline{\Gamma}$–$\overline{X}$, and **b** $\overline{\Gamma}$–$\overline{M}$ lines are shown as $h\nu$-$k_\parallel$ maps, measured using linear p polarisation of light.

I assign as the same surface states identified in ZrSiS [168, 178], arising from the breaking of nonsymmorphic symmetry at the surface. I will follow the naming convention set by Topp *et al.* [178], SS and SS′, shown also in Figure 4.6b.

The dispersions in Figure 4.8b,e illustrate the band shifts of these surface states as compared to ZrSiS, resulting from the aliovalent substitution of Nb for Zr and Sb for S described before. We can see that the SS state, which is derived predominantly from Nb states, is lowered in energy, while SS′, which also has a significant contribution from the Sb states, is significantly raised in energy. The effective hole doping on the Sb site forces SS′, which is fully occupied in ZrSiS, to cross the Fermi level along $\overline{\Gamma}$–$\overline{X}$, causing it to intersect SS along the $\overline{M}$–$\overline{X}$. This intertwining of the two surface states means that the elliptical Fermi pocket around $\overline{X}$ is now made from Fermi crossings of both surface states: SS along the $\overline{M}$–$\overline{X}$ line and SS′ along the $\overline{\Gamma}$–$\overline{X}$ line, unlike in ZrSiS, where it was made only by the SS state. Furthermore, we can see that with this substitution both SS and SS′ develop considerable splitting away from the high-symmetry time-reversal invariant momentum points, $\overline{X}$ and $\overline{M}$. The properties of this intertwining of the two pairs of surface states will be further explored in Section 4.7.

The surface states can in principle also be experimentally distinguished from the bulk states by their lack of dispersion in the out-of-plane direction. Changing the photon energy corresponds to probing bands at different out-of-plane momentum, and therefore, the bands that show no dispersion with photon energy can be assigned as two-dimensional, or surface states.
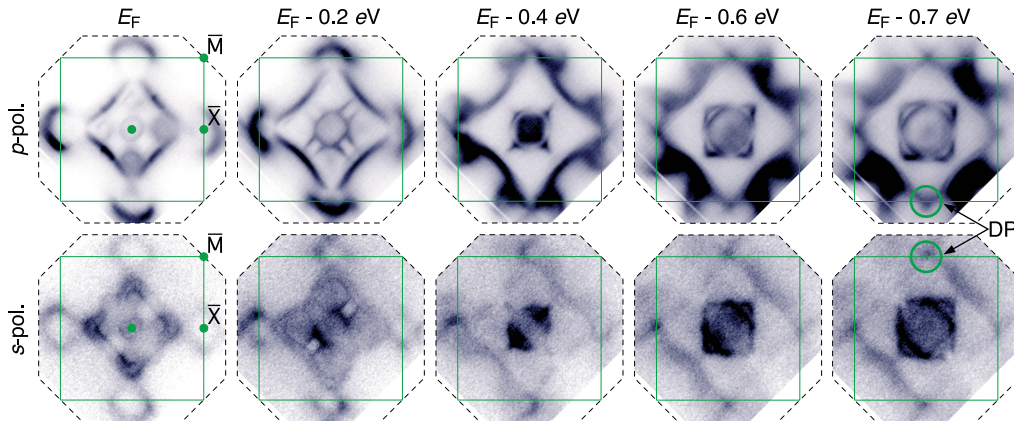
Figure 4.10: **Constant energy contours of the NbGeSb band structure.** The constant energy contours in 200 meV increments, measured at the SIS beamline in both p-polarised (top) and s-polarised (bottom) linear light polarisation. The symmetry enforced Dirac points are circled in green.

Figure 4.9a,b shows the photon energy ($h\nu$) dependence of the bands at the Fermi level along the $\overline{\Gamma}$–$\overline{X}$ and the $\overline{\Gamma}$–$\overline{M}$ high-symmetry lines, respectively. We can assign the observed bands to the features of the Fermi surface identified above. Indeed, the bands with significant surface character appear as straight lines in the k_z-$k_\parallel$ maps. We would expect the bulk bands to show periodic dispersion with k_z, and indeed such behaviour can be seen for the "petal" bands along $\overline{\Gamma}$–$\overline{M}$ and for the small square Fermi surface bands along $\overline{\Gamma}$–$\overline{X}$ for $h\nu \sim 60$–80 eV. Reliable recognition of dispersive features is made difficult due to two effects. The photon energies that were used in the experiment (< 200 eV) were too low for precise k_z selection, and instead integrate over a large interval of k_z values. The other effect comes from the matrix elements changing with photon energy, resulting in a strong variation of the measured spectral weight of the bands, additionally complicated by the nonsymmorphic symmetry [184].

The in-plane dispersion of the pockets can also be nicely illustrated by constant energy contours at a series of binding energies. Two such series of maps are presented in Figure 4.10, measured using the s and p linear polarisations of incident light. The different light polarisations highlight different features, such that we can see, e.g. the large square Fermi surface better using p-polarised light, while the corners of the small square Fermi surface and the "petal" pockets protruding from the large square pocket at the Fermi level are better seen with s-polarised light.

We can see that the square Fermi surfaces, as well as the small round Fermi surface at Γ, expand with increasing binding energy, demonstrating

a hole-like character. When the corners of the square pockets reach the X points, around 0.7 eV below the Fermi level, they cross the bands from the adjacent zones forming the enforced nonsymmorphic Dirac crossings discussed above. On the other hand, the "petals" of the "cross" pocket become smaller with increasing binding energy, narrowing to a line along $\overline{\Gamma}$–$\overline{M}$ around 0.5 eV below the Fermi level, which is explored in more detail below. This coexistence of electron- and hole-like pockets at the Fermi level is consistent with the expectation of global charge compensation in NbGeSb.

In the remainder of this Chapter I will first discuss two points of interest of the bulk band structure of NbGeSb, and then address the spin-orbit coupled surface states SS and SS′, which intertwine along the Brillouin zone edge forming the elliptical Fermi surface and two-dimensional equivalents of Weyl points.

4.6   NbGeSb bulk band structure

The most studied feature of the ZrSiS bulk band structure is the square Dirac nodal line pinned to the Fermi level [167–178], seen in Figure 4.5a,b. In NbGeSb, this nodal line develops much stronger hybridisation due to stronger spin-orbit coupling, but also becomes unpinned from the Fermi level due to charge redistribution as compared to ZrSiS. The equivalent feature can still be seen in the bulk band structure of NbGeSb as avoided crossings close to the Fermi level along the $\overline{\Gamma}$–$\overline{X}$ and $\overline{\Gamma}$–$\overline{M}$ lines in Figure 4.11 shown below, however, the notion of the nodal line is lost here.

Therefore, in this Section I discuss two striking features of the bulk electronic structure which were described above. The nonsymmorphic Dirac line nodes at the high-symmetry $\overline{X}$ and $\overline{M}$ points at the edge of the Brillouin zone, and the band crossing in the dispersion of the "petal"-shaped pockets along the $\overline{\Gamma}$–$\overline{M}$ high-symmetry line, seen in Figure 4.10. Both features are also shown to exhibit significant surface spectral weight, mixed with the bulk states in the form characteristic of surface resonances. Due to this mixed character of the bands, careful assignment of the origin of observed features will be necessary when discussing the data.

4.6.1   Symmetry enforced bulk Dirac nodal line

Arguably the most important feature of the bulk band structure are the nonsymmorphic symmetry enforced Dirac line nodes at $\overline{X}$ and $\overline{M}$. These
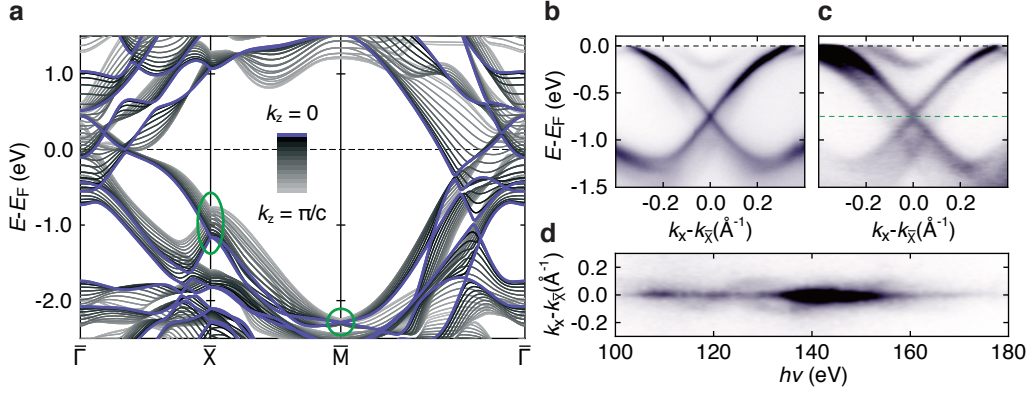
Figure 4.11: **Nonsymmorphic Dirac nodal line. a** Bulk band structure of NbGeSb from DFT calculations for different values of k_z. The symmetry enforced Dirac nodal lines at $\overline{\mathrm{X}}$ and $\overline{\mathrm{M}}$ are circled in green. **b** $\overline{\Gamma}$–$\overline{\mathrm{X}}$ dispersion, measured using 18 eV photon energy and linear s-polarised light, with clearly visible surface resonant states crossing at $\overline{\mathrm{X}}$. **c** The same dispersion as in **b**, measured using p-polarised 130 eV light, making the broad intensity of the bulk band dispersion visible as well. **d** Photon energy dependence of the cut indicated in **c**, measured with linear p-polarised light.

enforced nodal lines form along the out-of-plane momentum by extending the Young and Kane mechanism [161], illustrated in Figure 4.3e-f, into three dimensions as described above. To visualise the out of plane dispersion of the bulk bands, Figure 4.11a shows the bulk DFT calculation of the dispersions along the high-symmetry lines of the surface-projected Brillouin zone, projected to particular values of the out-of-plane momentum k_z. Two enforced Dirac nodes are circled, one at $\overline{\mathrm{X}}$ and the other at $\overline{\mathrm{M}}$. We can see that the enforced Dirac points are present at all plotted values of k_z, making them nodal lines along the M–A and X–R lines in the three-dimensional Brillouin zone, as was found for ZrSiS (Figure 4.5b). The Dirac points have a different binding energy at different k_z values, indicating that the nodal lines disperse along the out-of-plane direction. As in ZrSiS [167], we find that the nodal line at $\overline{\mathrm{X}}$ is much more dispersive than the one at $\overline{\mathrm{M}}$, indicated by the difference in binding energy of the crossing point for $k_z = 0$ and $k_z = \pi/c$.

This node is however most easily observable along the $\overline{\Gamma}$–$\overline{\mathrm{X}}$ line (Figure 4.11b,c), where it appears in the standard cone-like form, as a crossing of linearly dispersing bands with opposite velocities. Two features are seen to form the band crossing, a sharp cross with high measured intensity, and broad, weaker intensity which traces it. The broad feature is the k_z-broadened bulk state, while the sharp feature is the resonant surface spectral

weight, as seen in Figure 4.8e. Where these bands cross the Fermi level, they form the square Fermi surfaces along the $\overline{\Gamma}$–$\overline{X}$ line. The spectral weight of the bulk states is suppressed by matrix elements effects in Figure 4.11b. However, with a good choice of photon energy in Figure 4.11c, where both bulk band branches have visible intensity, we can experimentally confirm that the crossing occurs along a span of energies for different k_z values. We have performed a detailed photon energy-dependent measurement of these bands, and in Figure 4.11d I show a $h\nu$-$k_\parallel$ map centred at $\overline{X}$, 0.7 eV below the Fermi level where the surface resonant states cross. We can see that the surface state spectral weight forms a non-dispersive, straight line with $h\nu$, while the more diffuse, bulk spectral weight appears as a dispersive band around that line. Even though the shape of the bulk band in Figure 4.11d would indicate k_z dispersion, we cannot completely exclude that this is not simply an illusion coming from the intensity changes in the bulk states due to the variation of matrix elements effects with $h\nu$.

While the two bands that form the enforced crossing have opposite velocities along the $\overline{\Gamma}$–$\overline{X}$ direction, they both disperse downwards together along $\overline{M}$–$\overline{X}$. In the DFT calculations in Figure 4.11a, we can indeed distinguish these two bands, degenerate at the $\overline{X}$ and $\overline{M}$ high-symmetry points, but split and dispersing side-by-side along the Brillouin zone boundary. These are the bands that would have been degenerate if they originated only from the $\sqrt{2}\times\sqrt{2}$ square net layers of Ge atoms (Figure 4.3a,c,d). However, due to out-of-plane hopping of electrons, the bands gain some Nb and Sb character with a different symmetry environment (Figure 4.3b,e,f), which splits the two bands. This splitting can be seen as an energy scale of the relevant symmetry breaking due to the out-of-plane hopping processes. Comparing the calculated bands of NbGeSb in Figure 4.11a and for ZrSiS in Figure 4.5b, we can see that the splitting is considerably larger in NbGeSb, indicating stronger out-of-plane orbital overlap, consistent with NbGeSb having more radially extended orbitals as well as a smaller c/a lattice parameter ratio (2.218 [165], compared to 2.273 of ZrSiS [164]).

4.6.2   Dispersive nodal line along $\overline{\Gamma}$–$\overline{M}$

Another interesting feature of the bulk NbGeSb band structure presents itself along the $\overline{\Gamma}$–$\overline{M}$ high-symmetry line, without an obvious equivalent seen for ZrSiS in literature. I have described it already as the narrowing of the "petal"-shaped bands in Figure 4.10. A more detailed view is offered
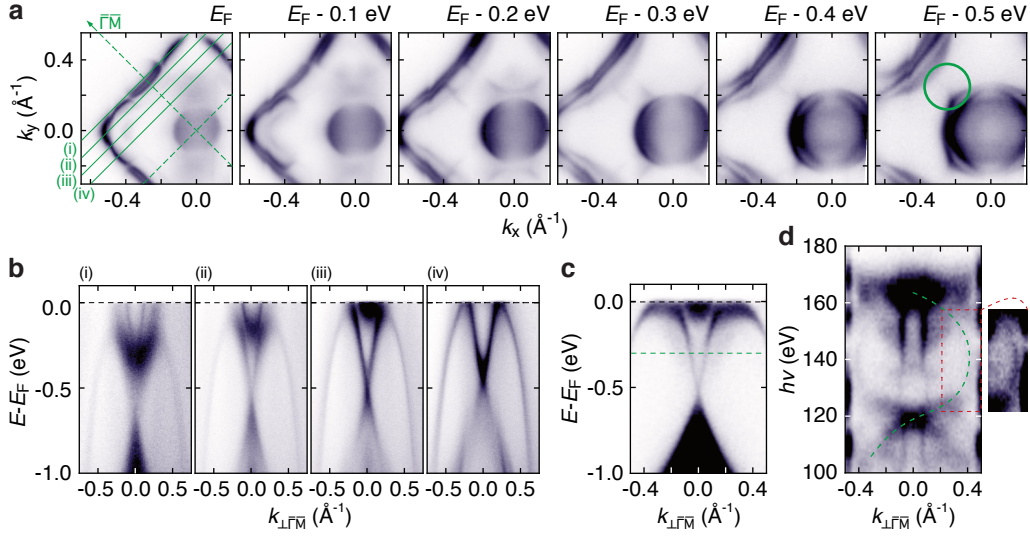
Figure 4.12: **Bulk line node along $\overline{\Gamma}$–$\overline{\mathrm{M}}$.** **a** High-resolution constant energy contours, measured using *s*-polarised 18 eV light. $\overline{\Gamma}$–$\overline{\mathrm{M}}$ lines are indicated by dashed green lines, and the position of the dispersive line node is circled in green. **b** A series of dispersions perpendicular to the $\overline{\Gamma}$–$\overline{\mathrm{M}}$ line were taken at position indicated in **a**. The data was measured using *p*-polarised 65 eV light, on a cleave which does not display the presence of the SS and SS′ surface states. **c** An equivalent dispersion to those in **b**, but measured at $k_{\overline{\Gamma\mathrm{M}}} = 0.386$ Å^{-1} along the $\overline{\Gamma}$–$\overline{\mathrm{M}}$ line, on a "standard" cleave, showing surface states, using *p*-polarised 130 eV light. **d** Photon energy dependence of the cut indicated in **c**, measured with *p*-polarised light. The dispersive bulk features are indicated by dashed green lines, and an inset with higher colour-saturation is used to make them more readily visible.

in Figure 4.12a, as constant energy contours from a high-resolution map, where we recognise the same features described above. It is clear that the flat sides of the large square Fermi surface are not continuous lines. The middle section along the $\overline{\Gamma}$–$\overline{\mathrm{M}}$ line is separated from the corners of the square (oriented along $\overline{\Gamma}$–$\overline{\mathrm{X}}$) by small hybridisation gaps at the Fermi level, presumably because they are intersected there by the bulk "petal"-pockets (not visible at the experimental conditions of the map in Figure 4.12a). Upon closer inspection, we can see that this middle section of the square Fermi surface's side is composed of two bands. This is expected since we have already concluded from Figure 4.8b,e that this Fermi surface comes from the split SS′ surface state pair becoming resonant with the bulk states as it crosses the Fermi level along $\overline{\Gamma}$–$\overline{\mathrm{M}}$.

Further below the Fermi level, we can clearly see the sides of the "petal" pockets coming closer together around the $\overline{\Gamma}$–$\overline{\mathrm{M}}$ line to form a cross with a centre at Γ, and finally meeting at 0.5 eV below the Fermi level. The

bands first meet close to the Brillouin zone centre, with the touching point moving to higher binding energies towards the $\overline{\text{M}}$ point. This forms an in-plane dispersive nodal line feature along the $\overline{\Gamma}$–$\overline{\text{M}}$ high-symmetry line.

Since the bands that form this nodal line disperse most strongly in the direction perpendicular to the $\overline{\Gamma}$–$\overline{\text{M}}$ line ($k_{\perp\overline{\Gamma\text{M}}}$), the crossing is most easily seen in that direction. Measured along the $\overline{\Gamma}$–$\overline{\text{M}}$ line ($k_{\overline{\Gamma\text{M}}}$) it appears only as a weak, non-dispersive feature seen in Figure 4.8b at ~ 0.3 eV below the Fermi level. Measured dispersions in the perpendicular direction, however, give striking results, showing a clear Dirac-like dispersion of the bands. Figure 4.12b shows such dispersion cuts measured at equidistant positions along the $\overline{\Gamma}$–$\overline{\text{M}}$ line, indicated in the constant energy maps in Figure 4.12a. The dispersions demonstrate that this linear band crossing indeed persists along $\overline{\Gamma}$–$\overline{\text{M}}$, forming a nodal line, as well as the fact that the nodal line disperses further below the Fermi level towards the edge of the Brillouin zone, as seen from the binding energy of the crossing point in the cuts in Figure 4.12b. It is worth noting here that the dispersions in Figure 4.12b were measured on one of the rare cases when the sample presumably did not cleave along the glide-mirror plane between the two Sb layers. The SS and SS$'$ surface states are therefore not present on this surface, and hence we do not observe the large square Fermi surface states which would appear as flat bands near the Fermi level of Figure 4.12b(i). In comparison, Figure 4.12c shows the equivalent dispersion cut, but measured on a "standard" cleave, and the surface states are clearly seen as a high-intensity flat state at the Fermi level. The flat band is broken into three parts where the bulk bands forming the "petal" cross through it, just as we have seen in the Fermi surface maps. This hybridisation of the bulk and surface states leads to surface resonant spectral weight of the SS$'$ states also dispersing down to form a sharp Dirac crossing. The lack of SS and SS$'$ surface states in Figure 4.12b, which typically manifest as the most intense bands in NbGeSb, has the advantage of giving the bulk states higher relative intensity in the measurements, allowing us to see them more clearly. However, this surface termination presumably also hosts surface states of a different kind, making the assignment of the band character difficult.

I again use a photon energy dependent map to help distinguish the bulk and surface contributions, and further characterise this band crossing. The out-of-plane dispersion of the states is shown in the $h\nu$-$k_{\overline{\Gamma\text{M}}}$ map in Figure 4.12d. It was taken at the same position along the $\overline{\Gamma}$–$\overline{\text{M}}$ line as the

dispersion in Figure 4.12c, at $k_{\overline{\Gamma M}} = 0.3861$ Å^{-1}, at the energy of 0.3 eV below the Fermi level. The normal emission of the map ($k_{\perp \overline{\Gamma M}} = 0$) represents the point on the $\overline{\Gamma}$–$\overline{M}$ line. Two main features can be seen in the map, a pair of parallel lines at $k_{\perp \overline{\Gamma M}} \approx \pm 0.05$ Å^{-1} showing no dispersion with $h\nu$, and two highly dispersive bands with low spectral weight, crossing at photon energies of ≈ 120 eV and ≈ 160 eV. The dispersion of this band is traced in Figure 4.12d for clarity, and an inset with higher colour saturation serves to make the band more easily visible. Since it is difficult to determine clear high-symmetry planes from our data without bias, I have chosen to leave the data represented by photon energy values, instead of converting those to k_z values. The features which are non-dispersive in the out-of-plane direction (with $h\nu$ in the map) are assigned as surface resonant spectral weight, and their crossing occurs at ≈ 0.5 eV below the Fermi level. The highly dispersive bands in Figure 4.12d are, on the other hand, bulk in origin, and form crossing points at ≈ 0.3 eV below the Fermi level as they disperse along the out-of-plane momentum direction. While it is likely related to the mirror plane which lies along $\overline{\Gamma}$–$\overline{M}$, the true origin of the observed Dirac nodal line here is currently not entirely understood.

4.7   Weyl-like points in the surface electronic structure

I now shift my focus to the two pairs of surface states, SS and SS′, introduced in Figure 4.8b,e as equivalents of the surface states known from ZrSiS (Figure 4.6). These surface states have a reportedly unconventional origin [178], arising from the breaking of the bulk nonsymmorphic symmetry at the surface which allows them to completely separate from their bulk partners along the entire Brillouin zone edge, and disperse in the projected bulk band gap there. However, this mechanism does not provide them with topologically non-trivial properties [168], and so we can consider them as conventional two-dimensional states, confined to the c-axis surfaces of the crystal. I will show below that starting from such trivial 2D states, and given the right symmetry conditions, we can engineer topologically non-trivial crossing points of singly-degenerate bands in the band-inversion scheme.

4.7.1   Spin-split surface states of NbGeSb

As discussed above, the two surface states are brought closer to each other in energy in NbGeSb than they are in ZrSiS. They are seen in Figure 4.8e to freely disperse along the Brillouin zone edge within a projected bulk band gap and to overlap at the $\overline{X}$ point causing a band inversion. Figure 4.13a provides a more detailed view of the bands, measured by ARPES, along the two high-symmetry lines in the vicinity of the $\overline{X}$ point. From the dispersions, we can clearly see that both surface states are split into two bands away from the high-symmetry (time-reversal invariant momentum) $\overline{X}$ and $\overline{M}$ points (Figure 4.8). While the SS bands have an electron-like dispersion at $\overline{X}$ along both high-symmetry lines (SS band along $\overline{M}$–$\overline{X}$ becomes the surface resonance seen best in Figure 4.11b along $\overline{\Gamma}$–$\overline{X}$), for the SS′ state $\overline{X}$ is more akin to a saddle point. The SS′ bands can be seen to disperse downwards from $\overline{X}$ towards the $\overline{M}$ point, but upwards, crossing the Fermi level to form the elliptical Fermi surface towards $\overline{\Gamma}$. I have conducted a series of spin-resolved ARPES measurements on these bands, with the key results presented in Figure 4.13a demonstrating that the splitting of both SS and SS′ surface states is a spin splitting. The spin-resolved EDCs and MDCs measured along the lines indicated in the $\overline{\Gamma}$–$\overline{X}$ and $\overline{M}$–$\overline{X}$ dispersions of Figure 4.13a reveal clear spin polarisation of the bands which reverses between the two branches of the same surface state. Given this behaviour,
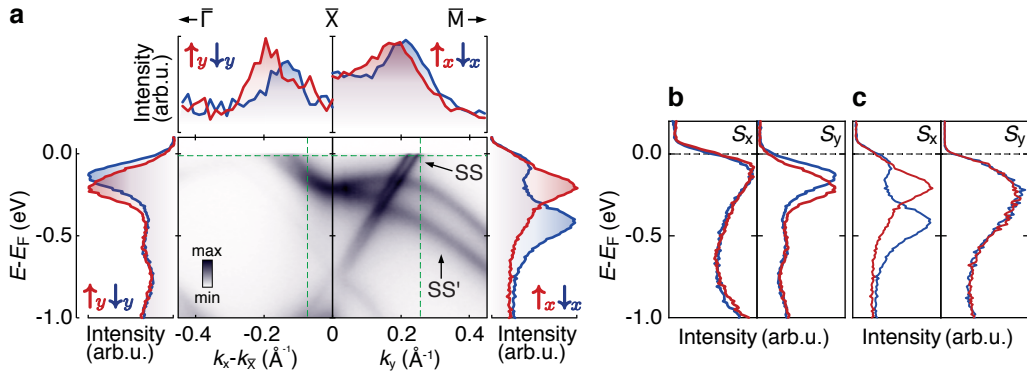

Figure 4.13: **Spin polarisation of the surface states. a** High-resolution ARPES data of the surface states near the $\overline{X}$ point, measured using *p*-polarised 18 eV light. The spin-resolved EDCs and MDCs show the splitting of the bands to be spin-splitting. The displayed spin component is perpendicular to the high-symmetry line at which the measurement is taken. **b,c** The measurement of the full in-plane spin polarisation of the bands is shown for: **b** the $\overline{\Gamma}$–$\overline{X}$ EDCs, and **c** the $\overline{M}$–$\overline{X}$ EDCs. The coordinate labels refer to Figure 4.14a.
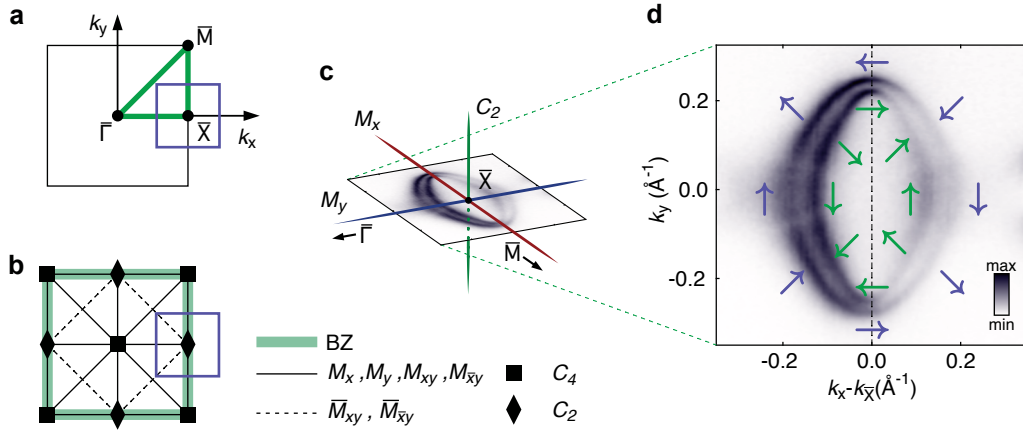
Figure 4.14: **Symmetry elements near the $\overline{\text{X}}$ point.** Surface projected Brillouin zone showing: **a** the coordinate system and high-symmetry lines, and **b** the position of all the symmetry elements of the *p4mm* layer group [185]. The elliptical surface state Fermi surface around the $\overline{\text{X}}$ point (purple squares in **a** and **b**) is shown with: **c** the relevant crystal symmetry elements, and **d** symmetry constrained spin texture for the outer (purple arrows) and inner (green arrows) elliptical pocket, determined by spin-ARPES experiments and DFT slab calculations.

I attribute the band splitting to the Rashba mechanism, described in Section 2.2, and in agreement with previous studies which observed a similar splitting of the SS state in HfSiS [167, 180].

All spin-resolved data in Figure 4.13a is plotted for the component of the spin polarisation perpendicular to the high-symmetry line along which the data was taken. Spin-resolved EDCs for the orthogonal in-plane spin components are shown alongside these in Figure 4.13b,c, exhibiting no resolvable polarisation of the bands for the component parallel to the high-symmetry line. The presence of C_4 and time-reversal symmetries precludes any out-of-plane spin polarisation. We can then conclude that the full 3D spin polarisation vector of the bands is in-plane, and lies perpendicular to the high-symmetry lines. All four Brillouin zone edges are equivalent under the C_4 rotational symmetry, and I choose the one at $k_x = \pi/a$ to focus on in the following discussion (see Figure 4.14a). At that zone face the S_y spin component is along $\overline{\Gamma}$–$\overline{\text{X}}$, while the S_x spin component is along $\overline{\text{M}}$–$\overline{\text{X}}$, as indicated in Figure 4.13. We can understand this by employing symmetry analysis to the possible spin components of the bands. As seen in Figure 4.14b,c, two mirror lines cross at the $\overline{\text{X}}$ point, running along the two perpendicular high-symmetry lines. Since spin is an axial vector property, mirror operations flip the components parallel to them, but keep the

70

perpendicular components invariant. Only those can therefore be present along the mirror lines. Quantum mechanically, singly degenerate bands along a mirror line need to be definite eigenstates of that mirror operation, i.e. spin-up and spin-down perpendicular to the mirror.

The symmetry elements present around $\overline{\text{X}}$ strongly constrain the spin texture of the surface states. In particular, we have seen that the SS and SS′ surface states combine to form the spin-split elliptical Fermi surface surrounding the $\overline{\text{X}}$ point. Due to all the described symmetry restrictions, and SS and SS′ having the same effective sign of the Rashba effect, the two ellipses of the Fermi surface acquire a complex spin texture schematically drawn in Figure 4.14d. The information about the spin texture comes from further, detailed spin-resolved measurements on and off the high-symmetry directions along the elliptical Fermi surface, and is also in good agreement with predictions from the DFT calculations. This spin texture is at a glance uncharacteristic of the standard spin-momentum locking in Rashba split states, such as Au(111) surface states mentioned before, as they have the opposite winding number. However, we need to keep in mind that this is a Fermi surface formed of two different Rashba split bands in perpendicular directions, and that it forms on the edge of the Brillouin zone, instead of at its centre, allowing for this texture.

4.7.2 Surface state band crossings

The structure of the crossing created by the inversion of SS and SS′ surface state pairs along the Brillouin zone edge will be of interest for the rest of this Chapter. Along the $\overline{\text{M}}$–$\overline{\text{X}}$–$\overline{\text{M}}$ line of the Brillouin zone edge, it is the top of the SS′ band that inverts with the bottom of the SS band at the $\overline{\text{X}}$ point. Since the two surface states here cross as spin-split pairs, they form a quartet of crossings on either side of the high-symmetry $\overline{\text{X}}$ point. This crossing structure is shown in Figure 4.15 as measured in a high-resolution ARPES dispersion and calculated by the DFT slab calculation. To make further discussion of the crossing structure easier, I assign numbers to the four crossing points, as shown in Figure 4.15, such that crossings #1 and #3 are between opposite-spin bands, while the #2 and #4 are between like-spin bands. The experiment and the calculations show excellent agreement, confirming that the electronic structure of NbGeSb is in the weakly interacting regime. We do observe a signature of electron-phonon coupling as small characteristic kinks (discussed in Section 2.4.1) in the SS bands
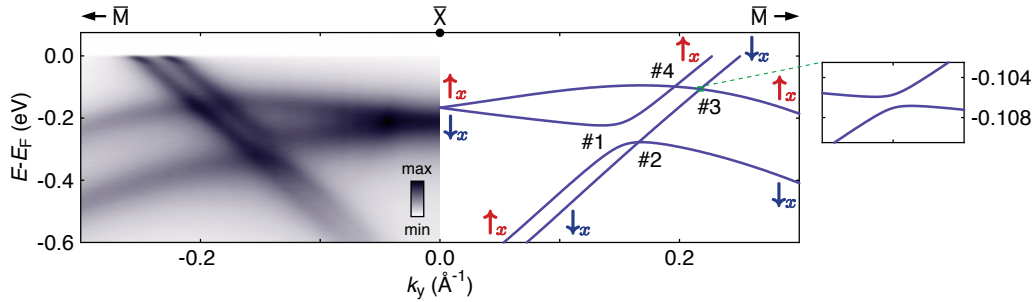
Figure 4.15: **Surface state crossing structure along $\overline{\mathrm{M}}$–$\overline{\mathrm{X}}$–$\overline{\mathrm{M}}$.** The fourfold crossing between SS and SS′ states along the Brillouin zone edge is shown in high-resolution ARPES measurement (left), and from DFT calculations (right). The crossing points are numbered in the DFT dispersion, and spin labels are assigned to the bands. The inset shows a small gap developing at crossing #3.

appearing at ≤ 50 meV from the Fermi level.

The observed quartet of crossings exhibits a peculiar structure, presenting two main points of interest. First is that the like-spin crossings appear to be protected, with no sign of hybridisation in either the measured or calculated dispersions. This is in contrast with the crossing #1, of oppositely spin-polarised bands, which develops a clear gap on the order of 50 meV. However, the crossing #3, its opposite-spin partner, is only seen to open a small gap of ≈ 1 meV in a calculation done on a very dense $\mathbf{k}$-path (inset of Figure 4.15). This is too small to be experimentally resolved here, and the #3 crossing shows no appreciable gap in the measured ARPES dispersion. A strong anisotropy is thus present in the hybridisation strengths of the #1 ($\uparrow_x$,$\downarrow_x$), and the #3 ($\downarrow_x$,$\uparrow_x$) band crossings.

The intertwining of the SS and SS′ surface state pairs around $\overline{\mathrm{X}}$ is further revealed in the way the elliptical surface Fermi surface evolves with binding energy in Figure 4.16a,b. Instead of the pocket simply becoming smaller further below the Fermi level, as it does in ZrSiS (Figure 4.6a), it goes through a series of Lifshitz-like transitions at the energies where the bands intersect. The constant energy contours at the energy of each of the four crossing points identified in Figure 4.15 are shown both as measured ARPES maps, and as calculated by slab DFT. At ~ 0.75 eV below the Fermi level, the original pocket finally closes and merges into a point, which we can identify as the symmetry enforced Dirac crossing of the surface resonant states along $\overline{\Gamma}$–$\overline{\mathrm{X}}$ seen in Figure 4.11b,c.

This can also be seen in Figure 4.16c, in a series of dispersions parallel with the $\overline{\mathrm{M}}$–$\overline{\mathrm{X}}$–$\overline{\mathrm{M}}$ line, extracted from the same dataset. These dispersions
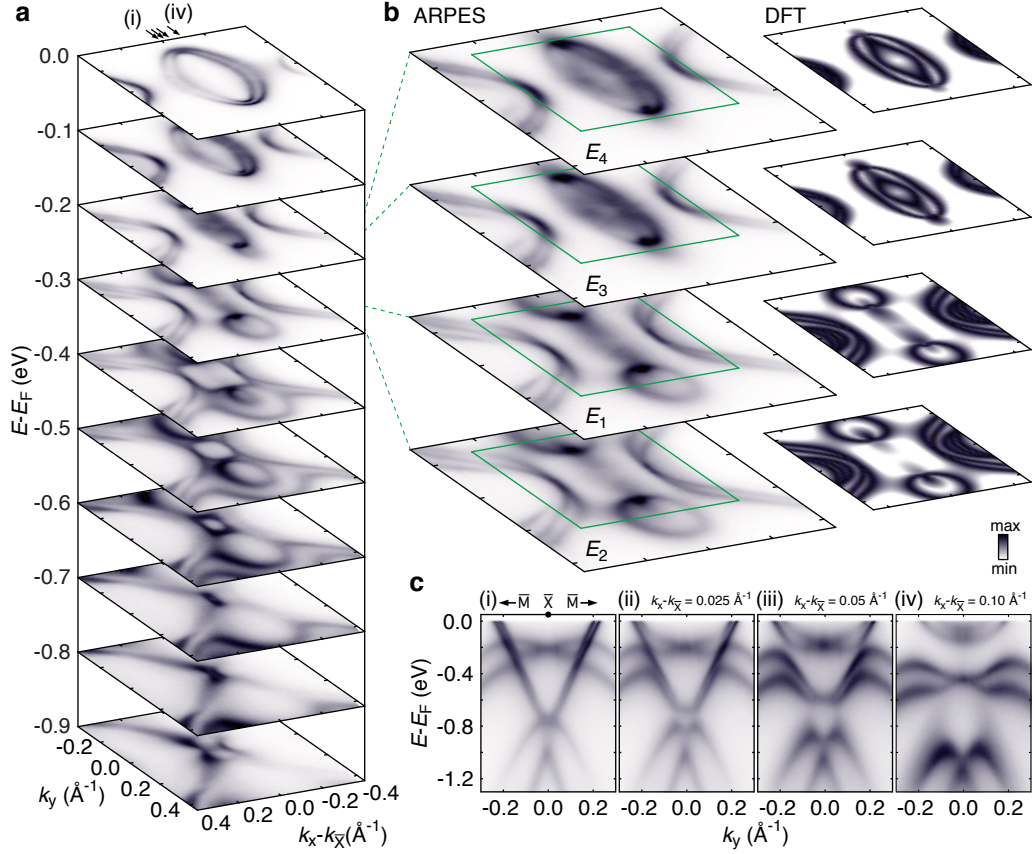
Figure 4.16: **Intertwining of surface states off high-symmetry lines.** Constant energy contours of the elliptical surface state Fermi pocket, **a** at 100 meV intervals, and **b** at binding energies of the four crossing points from Figure 4.15 which are compared to DFT calculations. **c** Dispersions parallel to the $\overline{\mathrm{M}}$–$\overline{\mathrm{X}}$ line from the same measured dataset at k_x positions indicated in **a**. For clarity, the ARPES data is presented as a sum of normalised measurements made using p- and s-polarised 18 eV light.

also reveal the importance of the mirror symmetry element present on the Brillouin zone edge. While the unusual structure of the four crossings seen in Figure 4.15 is present along the Brillouin zone edge, even slight deviation from the mirror line leads to the two pairs of surface states opening gaps and separating completely.

The asymmetric hybridisation of the #1 and #3 crossings in Figure 4.15 are highly unusual, since for conventional bulk states, which have their orbital momentum quenched by the crystal field, there is no *a priori* way to differentiate a $(\uparrow_x, \downarrow_x)$ from a $(\downarrow_x, \uparrow_x)$ crossing. In that situation we might expect similar hybridisation gaps to develop in both crossings. However, this is not necessarily true for surface states, where finite unquenched orbital angular momentum (OAM) is allowed to develop. I will show below that

this ultimately drives the unusual crossing structure here.

4.7.3   Orbital angular momentum of the bands

The loss of inversion symmetry at the surface allows for the development of unquenched orbital angular momentum by allowing additional orbital hybridisations, prohibited in the inversion symmetric bulk [73, 95, 186–188]. When spin-orbit coupling is smaller than the scale of inversion symmetry breaking, it cannot mix the states which have opposite orbital angular momenta, but instead only splits them by spin. Such a spin-splitting then develops on the scale of the full atomic spin-orbit coupling, and considerable orbital angular momentum is expected to arise in such surface states, with approximately the same expectation value in both spin-split branches [73, 187, 188]. For the SS and SS′ surface states of NbGeSb, the size of the spin splitting is best seen in Figure 4.15. The SS band develops maximal splitting of $\sim$ 90 meV, while the splitting in SS′ reaches $\sim$ 225 meV, values comparable to the average atomic spin-orbit coupling for Nb $4d$ and Sb $5p$ orbitals [60, 189], weighted by their relative contributions to the bands. This indicates that the energy scale of the inversion symmetry breaking in NbGeSb is indeed larger than that of the atomic spin-orbit coupling [188], and that we can expect these surface states to develop significant orbital angular momentum.

Since the Brillouin zone edge hosts a mirror line, all eigenstates of the SS and SS′ surface states along it must have definite parity with respect to that mirror operation [76, 77]. Considering that orbital angular momentum is an axial-vector property, the same symmetry restrictions apply to it as for the spin angular momentum, discussed above. It is therefore expected that L_x would be the only orbital angular momentum component that develops an expectation value in the bands along the $k_x = \pi/a$ Brillouin zone edge, which is a M_x mirror line. We can already see this from the orbital decomposition of the surface states as given by the slab DFT calculations in Figure 4.17a,b. The Nb $4d$ orbitals (Figure 4.17a) even under the M_x mirror are the $d_{3r^2-z^2}$, $d_{x^2-y^2}$ and d_{yz}, and they contribute only to the SS state. These orbitals form the basis for the orbitally unquenched states with $L_x = \{-2, 0, +2\}$, which are even under M_x. The remaining d_{xy} and d_{xz} contribute only to the SS′ state. They are odd under the M_x mirror, and form the basis for $L_x = \{-1, +1\}$ states, placing the orbital angular momenta of the SS and SS′ states in two orthogonal manifolds as required
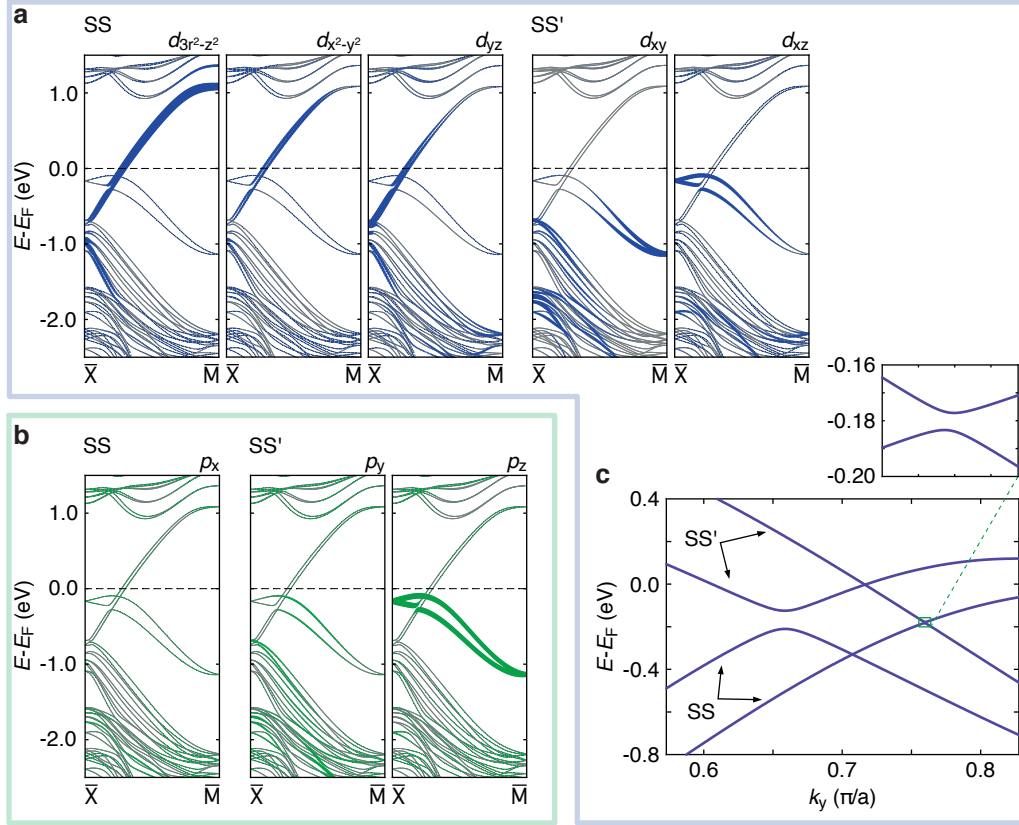
Figure 4.17: **Orbital decomposition of surface states and the tight-binding model.** Slab calculation along the $\overline{X}$–$\overline{M}$ line with projection of the eigenstates onto atomic orbital basis of: **a** Nb, and **b** Sb surface layers. **c** The fourfold crossing of the surface states along $\overline{X}$–$\overline{M}$ is reproduced by a tight-binding model using the five Nb $4d$ orbital basis.

by symmetry.

Of the Sb $5p$ bands (Figure 4.17b), p_x contributes to SS, and p_y and p_z contribute to SS′. This would naïvely appear to be opposite parity contributions to those from the Nb orbitals. However, since Sb and Nb atoms never lie on the same M_x mirror line in the surface unit cell (the symmetry schematic in Figure 4.14b applies to Figure 4.4b,c as well), we need to make a choice of which one to use. The mirror line which keeps the Nb positions invariant will map the Sb atoms to a point a distance a away in the x direction, and an opposite translation is then needed to bring them back to the original position. This translation introduces a corresponding Bloch factor of $e^{-i\mathbf{k}\cdot\mathbf{r}}$ into the wavefunction, where the translation vector is $\mathbf{r} = (a, 0)$ and on our chosen Brillouin zone edge we have $k_x = \pi/a$. The Bloch factor therefore reduces to a phase of $e^{i\pi} = -1$, exchanging the effective parities of Sb orbitals for the M_x mirror operation.

75

In order to pursue the orbital angular momentum composition of the bands further, we have constructed a tight-binding model of the SS and SS′ surface states. For simplicity, we restrict the choice of basis states to the five Nb $4d$ orbitals, since the symmetry allowed mixing of the Sb states would not affect the fundamental results. The model is built in three steps as:

$$H = H_0 + H_{\mathrm{R}} + H_{\mathrm{SO}},$$

described in detail in Section 4.4. The H_0 term encodes the spin-independent near-neighbour hopping processes, restricted by the symmetries of the system given in Figure 4.14b, and H_{R} and H_{SO} represent separate inter-unit cell Rashba component and an intra-unit cell atomic **k**-independent component of spin-orbit coupling, respectively. This separation of spin-orbit terms allows us to consider the influence of orbital mixing generically allowed by the atomic $\mathbf{L} \cdot \mathbf{S}$ term on the crossings of bands split by the Rashba mechanism. The result of the model along the $k_x = \pi/a$ Brillouin zone edge, shown in Figure 4.17c, faithfully reproduces the fourfold crossing structure of the surface states seen in Figure 4.15 and the asymmetry in the hybridisation strengths of the opposite spin crossings #1 and #3.

Figure 4.18a reproduces the quartet of band crossings from the tight-binding model from Figure 4.17c, now including the expectation values of orbital angular momentum. Our expectation based on symmetry analysis is confirmed, and only the L_x component of orbital angular momentum acquires a finite value along this Brillouin zone edge. The SS′ pair of bands is shown to be nearly in the pure $L_x = +1$ state, while SS pair is mainly in the $L_x = 0$ state, showing small admixture of the $L_x = \pm 2$ state.

A minimal model which neglects the $L_x = \pm 2$ contribution in the SS′ states, and treats all bands as having pure orbital angular momentum values, is shown in Figure 4.18b and represents a good starting point for explaining the peculiar crossing structure from Figure 4.15. Since this simplification puts the orbital angular momenta of SS and SS′ in neighbouring L_x projections, we can see that the strong symmetry restrictions on allowed angular momentum components along the Brillouin zone edge formulate the minimal band crossing problem in terms of a two-level model in both the spin and orbital angular momenta. Any inter-orbital mixing of states with orthogonal mirror parity is forbidden at the mirror lines, and so only the atomic spin-orbit coupling of the $H_{\mathrm{SO}} \propto \mathbf{L} \cdot \mathbf{S}$ form can open hybridisation gaps seen in crossings #1 and #3.
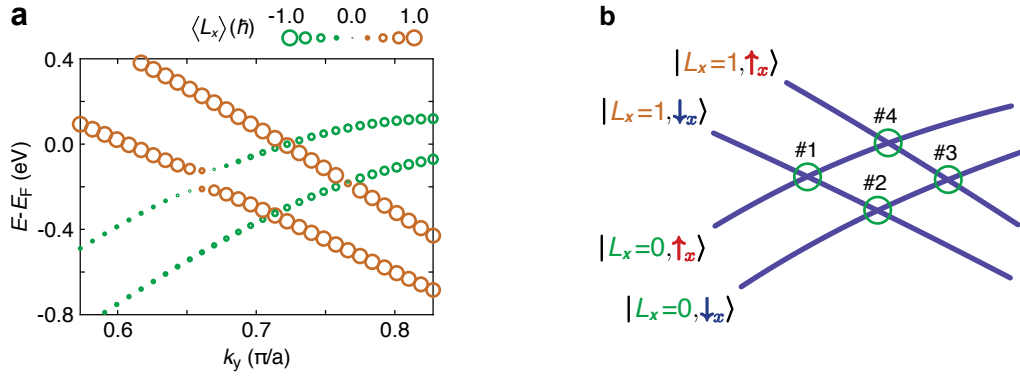
Figure 4.18: **Orbital angular momentum in surface states. a** The tight-binding bands from Figure 4.17c are shown with projected expectation value of the x component of the orbital angular momentum. **b** Schematic of the minimal model of the fourfold surface state crossing, with the bands labelled by the orbital and spin angular momenta in ket notation.

The x basis is the natural one to use in this situation, as only the x components of orbital and spin angular momentum are expected to be non-zero, giving us [59]:

$$\mathbf{L} \cdot \mathbf{S} = L_x S_x + \frac{1}{2}(L_+ S_- + L_- S_+)$$

as the Hamiltonian acting at the four band crossings in Figure 4.18b. The $L_x S_x$ term will not be able to act at any of the four crossing points, since they are all between bands with different L_x values, regardless of the spin sector. In fact, even with allowing for the orbital angular momentum states not to be pure, this still holds because the bands that cross always belong to orthogonal manifolds under the mirror symmetry. We therefore only need to consider the remaining, "spin-flip" terms, which hybridise states where the spin and the orbital angular momenta change in the opposite sense.

Only crossing #1, between $|L_x{=}1, \downarrow_x\rangle$ and $|L_x{=}0, \uparrow_x\rangle$ fits into that category, and it is indeed the one where a sizeable gap is visible in the real material. At #3, its opposite-spin crossing partner, the spin and angular momenta change in the same sense between $|L_x{=}1, \uparrow_x\rangle$ and $|L_x{=}0, \downarrow_x\rangle$ and it is therefore protected within this minimal model. In reality, the admixture of $L_x = \pm 2$ in the SS' states allows the "spin-flip" terms to act, and so our tight-binding model opens a gap at #3. The size of this gap is determined by the amount of the admixed states, and is expected to be small compared to the one that opens at #1. The gap size ratio in our tight-binding model is ~ 14, while an even larger ratio is seen for the real material (~ 50 in the

DFT calculations in Figure 4.15). The large observed gap asymmetry points to the deviations from the simple two-level model being small in reality.

At the two like-spin crossings, #2 and #4, the "spin-flip" terms cannot act between bands as they have the same spin projection, and $L_x S_x$ is still forbidden because the bands belong to orthogonal orbital angular momentum manifolds. Even in the realistic case when the orbital angular momentum states are not pure, these conditions are ensured by the presence of the mirror symmetry along this high-symmetry line, making the #2 and #4 crossings strictly protected.

4.7.4   Weyl-like points in the tight-binding model

We have seen in Figure 4.16c already that all four crossing points open up gaps as the bands move off the mirror line on the Brillouin zone edge. As soon as the strict symmetry requirements on the eigenstates are lifted away from the mirror line, both inter-orbital mixing and spin canting become allowed, opening gaps even for the crossings of the like-spin bands. This means that the #2 and #4 crossing points along the $\overline{X}$–$\overline{M}$ line are isolated band degeneracies in momentum space. The full dispersion of bands in the vicinity of the crossing point #4 is depicted in Figure 4.19a and locally has the typical cone shape of tilted type-I Weyl fermions [190] seen in bulk materials.

Here, however, the bands are confined to the two-dimensional surface of the crystal. As I have discussed in Section 4.1, 3D Weyl points are fully "accidental" crossings of two singly degenerate bulk bands, with their
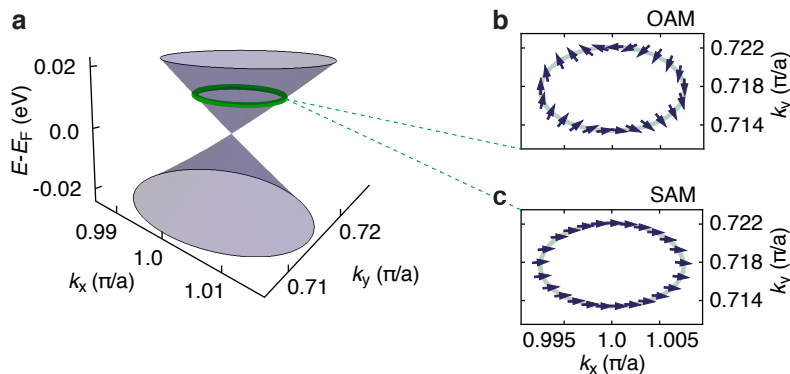

Figure 4.19: **Protected Weyl-like crossing of surface states. a** Band dispersion around the crossing #4 from Figure 4.18b, calculated by our tight-binding model. **b** Orbital and **c** spin angular momenta are extracted along the indicated green contour.

local protection lying in the fact that the three dispersion terms in the Hamiltonian use up all of the Pauli matrices spanning the basis of the Hamiltonian. In two dimensions the out-of-plane dispersion is lost, and some additional symmetry is needed to prevent perturbations in σ_z, which would generically open a gap in the spectrum. At this level one could still imagine the crossing point occurring at an arbitrary value of both in-plane momentum components (k_x, k_y). The surface states of NbGeSb, however, fall in the category shown in Figure 4.1d, where a crystal symmetry protects the crossing only along a particular high-symmetry line in momentum space. The symmetries in NbGeSb fix the value of one of the in-plane momenta to the Brillouin zone edge, leaving the remaining one as the accidental position of the crossing along the high-symmetry line, and also prevent any perturbations in σ_z from gapping the like-spin crossings of the surface states.

For the conventional Weyl theory, the two bands that cross have opposite spin, and the winding of the spin angular momentum of the bands on closed contours around the crossing point has become one of the defining characteristics of Weyl points [11, 140, 141]. In our case, the protected crossings are between bands of the same spin, but different parity of orbital angular momentum. In order to interpolate between the two opposite parities, it is now the orbital angular momentum which winds on a small closed loop around the crossing point in **k**-space, seen in Figure 4.19b, while the spin only develops slight canting in Figure 4.19c. The low-energy description of the crossing can be written as

$$H_{\text{eff}} = v\xi_z \left(\tau_x p_y + \tau_y p_x \right), \tag{4.3}$$

where v is the velocity, ξ_z is a pseudospin-1/2 variable defining on which Brillouin zone edge the crossing is located, $\boldsymbol{\tau}$ is the orbital pseudospin, and **p** is the in-plane momentum relative to the crossing point. The orbital pseudospin-1/2 variable $\boldsymbol{\tau}$ is written here in its natural basis, such that it is aligned with the orbital angular momentum **L**. Applying subsequent C_4 rotation and M_x mirror reflection to the pseudospin does not affect the winding number of the effective Hamiltonian in Equation (4.3) and it transforms it into the standard Weyl form $\propto \boldsymbol{\tau} \cdot \mathbf{p}$ of Equations (4.1) and (4.2) [11, 140]. This shows that the low-energy description of the protected crossings of NbGeSb surface states is topologically equivalent to a 2D Weyl Hamiltonian, leading me to denote them as "Weyl-like" [140].

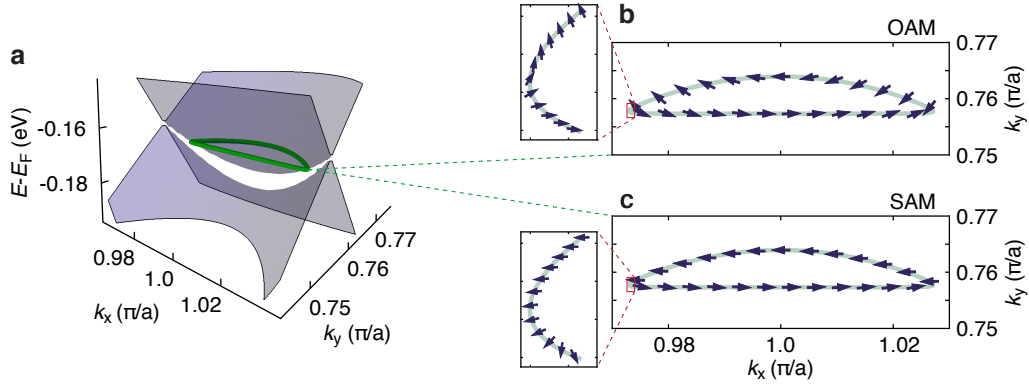The local dispersion around the slightly gapped opposite-spin crossing

Figure 4.20: **Gapped crossing of surface states.** **a** Band dispersion around the crossing #3 from Figure 4.18b, calculated by our tight-binding model. **b** Orbital and **c** spin angular momenta are extracted along the indicated green contour. The insets demonstrate the winding of both angular momenta near the high-symmetry line.

#3 is shown in Figure 4.20a. As the bands at this crossing have both different spin and orbital angular momentum, both properties develop a winding on a closed loop around the crossing point to interpolate the values. The orbital and spin angular momenta display winding numbers of -1 and +1 in Figure 4.20b,c, respectively, with the majority of the winding being restricted to the close proximity of the high-symmetry line as seen in the insets of Figure 4.20b,c. It is interesting to note that this complex winding structure does not in itself require the crossing to be gapped. We can imagine closing only the $\mathbf{L} \cdot \mathbf{S}$ derived gap without changing the rest of the band structure, effectively setting $\alpha_{\mathrm{SO}} = 0$ in the tight-binding model. In that case the winding structure of both spin and orbital angular momenta seen in Figure 4.20b,c would still persist around the now protected crossing point #3, making the interplay of the spin and orbital degrees of freedom even more intricate here than in the like-spin crossings #2 and #4.

4.8 Conclusion

I have presented an overview of the electronic structure of NbGeSb, a little-studied member of the ZrSiS family of nonsymmorphic bulk Dirac nodal line materials. Alongside an observation of the expected bulk nodal line enforced by nonsymmorphic symmetry, I identify an additional dispersive nodal line along the $\overline{\Gamma}$–$\overline{\mathrm{M}}$ high-symmetry line in the bulk band structure.

In the surface electronic structure, I show two topologically trivial, Rashba spin-split pairs of states whose band inversion creates a series of

two-dimensional Weyl-like crossing points along the edge of the Brillouin zone. This finding reveals the exciting possibility of driving topological transitions via parity inversion of electronic bands not only in the bulk, but also in two-dimensional surface systems. This is of practical importance as the surface state energies lend themselves much more easily to manipulation and tuning via e.g. gating of interfaces or surface adsorption of dopants. In NbGeSb, transport effects from the protected surface state crossings would be obscured by the presence of the metallic character of the bulk. However, we can imagine similar band structures could be realised within projected bulk band gaps, where they would be accessible even to transport measurements.

One could also imagine this leading to additional lower-dimensional topological edge state, i.e. an equivalent of the surface Fermi arc states, which span the projections of the chiral pairs of standard Weyl points in 3D onto the surface Brillouin zone [11, 140, 141]. Further theoretical analysis of the 2D Weyl analogues I present here is needed to ascertain whether they could support equivalent long-lived one-dimensional edge states. In general, it might be possible to stabilise 1D edge states by parity inversion of two-dimensional bands in a material with a topologically trivial bulk. This would provide an alternative to the theoretically predicted hinge-states [191–193], which are also 1D edge modes, but stabilised by higher-order topological invariants in the bulk.

The surface state electronic structure of NbGeSb showcases how the interplay of spin-orbit coupling and crystal symmetries can create intricate and novel phenomena in weakly interacting electron systems. In the next Chapter, we shall see how such interplay manifests in a material with strong electronic interactions.

5 | Electronically driven spin reorientation in $Ca_3Ru_2O_7$

In this Chapter, I shift the focus to $Ca_3Ru_2O_7$, a material in which strong electronic interactions are present. Materials with partially filled d or f orbitals typically exhibit strong electronic correlations [194, 195], giving rise to an abundance of new phenomena such as metal-insulator transitions [39, 41], high-temperature superconductivity [6–8, 44], colossal magnetoresistance [196], or quasiparticles with large effective masses and reduced spectral weight [197, 198]. The prevalent explanation for the correlated behaviour relies on the Mott mechanism, whereby carriers are localised due to strong Coulomb repulsion, U, and reduced bandwidth, W, leading to Mott insulators [39, 41]. The Mott effects, proportional to U/W [39], are most pronounced in $3d$ materials such as cuprates, but weaken down the periodic table where more extended orbitals provide for both reduced values of the screened Coulomb interaction and relatively broad bands due to higher orbital overlap. Nonetheless, $4d$ materials such as ruthenates still exhibit significant correlation effects, as well. In the past decade it has been recognised that many of them owe their strong correlation effects to Hund's coupling, giving rise to so called Hund's metals [40, 199]. They also host pronounced strength of spin-orbit interaction, which is typically considered negligible in the light $3d$ transition metal atoms, making them ideal for our study.

5.1 $Ca_3Ru_2O_7$ crystal structure

$Ca_3Ru_2O_7$ has a layered perovskite structure, belonging to the Ruddlesden-Popper family [200, 201]. The materials of the Ruddlesden-Popper series have the general formula: $A_{n+1}B_nO_{3n+1}$ (Figure 5.1), and can host a wide variety of physical properties due to many allowed combinations for the A and B site cations [202]. The A site is typically an alkaline metal, mainly influencing the overall crystal structure and its deformations through steric and bond-valence effects [203–205]. Meanwhile, the B site is occupied by a transition metal cation centred within an oxide octahedron which dominates
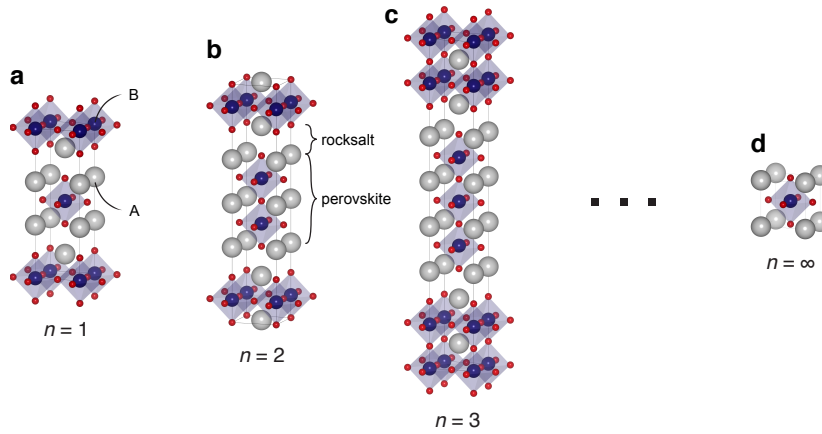
Figure 5.1: **Ruddlesden-Popper series.** The crystal structure of the Ruddlesden-Popper series, showing the: **a** single-, **b** bi- and **c** trilayer compounds, as well as the **d** $n = \infty$ cubic perovskite. The A and B cation positions of the general formula ($A_{n+1}B_nO_{3n+1}$) are indicated (**a**), and the rocksalt and perovskite layers are indicated in (**b**). Here I show the strontium titanate series, which retains the high-symmetry $I4/mmm$ structure across the first three members.

the electronic properties of the material. Their structural basis, the simple cubic perovskite structure, can be described as an interpenetrating primitive cubic structure of A and B cations, with face-centred oxygens (see $n = \infty$ in Figure 5.1), or alternatively, as a staggered stacking of AO and BO_2 square layers [205, 206], giving the formula unit ABO_3 of cubic perovskites. The chemical formula of the Ruddlesden-Popper series, $A_{n+1}B_nO_{3n+1}$, can be rewritten as $(AO)(ABO_3)_n$ illustrating the separation of the n perovskite layers stacked along the c-axis of the crystal, and the rocksalt spacer layers, as indicated in Figure 5.1b. The series goes from single-layer, $n = 1$, materials, where the perovskite and rocksalt layers alternate 1-to-1, to $n = \infty$, which is the simple cubic perovskite structure without any rocksalt layers.

The base structure is defined by the tetragonal body-centred space group $I4/mmm$ [200, 201]. However, many members of the Ruddlesden-Popper series will undergo structural distortions, lowering the overall symmetry of their structures. These distortions will commonly involve rotations [207] and Jahn-Teller distortions [57, 208–210] of the BO_6 octahedra, as well as global polar distortions of the structure [211, 212]. Some general trends of the extent of the distortions are observable in related Ruddlesden-Popper materials, such as Sr and Ca based ruthenate series [40, 213]. One is the number of the stacked perovskite layers, n, and is specific to the layered

nature of the structure. With increased n there is an increased number of structural degrees of freedom to provide distortions which could lower the total energy of the structure, and so we observe a tendency towards more distorted structures with increased n. Another factor in this case is the type, and size, of the A site cation [202, 206]. As mentioned above, its influence will mainly be through steric and bond-valence effects, well known in inorganic crystal chemistry [203–205]. In order to stack the AO and BO_2 layers in the perovskite crystal structure, the interatomic distances between the oxygen and the cations are changed from their equilibrium values, leading to suboptimal effective valence of the cations. In order to alleviate this problem, the perovskite structure buckles by way of rotating the BO_6 octahedra. The rotation disproportionates the O–A–O bond lengths, and as the bond-valence depends exponentially on the the interatomic distance, this brings it back closer to the equilibrium value. Due to steric effects, smaller cations will typically allow for larger octahedral rotations [206].

The Sr and Ca ruthenate series nicely exemplifies these trends. The single-layer Sr_2RuO_4 has completely undistorted RuO_6 octahedra [214], whereas in the bilayer $Sr_3Ru_2O_7$ they develop in-plane rotations [215]. By substituting the smaller Ca cation for Sr in the series, we observe further increase in the distortions for the same n. In Ca_2RuO_4 [216] and $Ca_3Ru_2O_7$ [217] the octahedra buckle, developing both in-plane and out-of-plane rotations. However, while Ca_2RuO_4 is centrosymmetric, $Ca_3Ru_2O_7$ develops a global polar distortion. All of these materials, as well as their cubic perovskite ($n = \infty$) counterparts, host a wide variety of correlation-induced phenomena [40]. Of the simple perovskites, $SrRuO_3$ is a ferromagnetic metal [218], and $CaRuO_3$ is a paramagnetic metal showing transport behaviour incompatible with Fermi liquid predictions [219]. Single-layered Sr_2RuO_4 is a highly studied unconventional superconductor [214, 220–222], while the bilayer $Sr_3Ru_2O_7$ has been reported to host a metamagnetic quantum critical point [223] and electronic nematicity [224]. The single-layer Ca compound is the only reported ruthenate insulator [225], undergoing an orbitally selective Mott transition [226, 227] whose transition temperature can be shifted by applying pressure or driving an electric current through the sample [228]. All of them exhibit significant mass renormalisations ($m^*/m = 4$–10) as compared to simple band structure calculations [40], and as a $4d$ metal, Ru introduces significant spin-orbit coupling. The bilayer $Ca_3Ru_2O_7$ is thus a prime candidate for the study of spin-orbit coupled

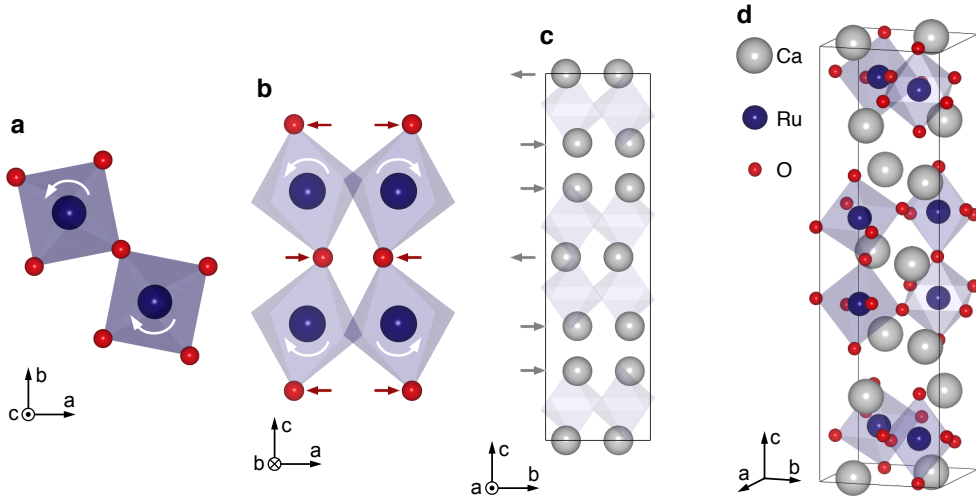Figure 5.2: **Crystal structure of** $Ca_3Ru_2O_7$**. a** Illustration of the X_2^+ octahedral rotation mode in one bilayer of the $Ca_3Ru_2O_7$ structure. Only basal oxygen atoms shown for clarity. **b** Illustration of the X_3^- octahedral tilt mode in one bilayer of the $Ca_3Ru_2O_7$ structure. Only apical oxygen atoms shown for clarity. **c** Illustration of the polar Γ_5^- mode displacing Ca ions in the unit cell of $Ca_3Ru_2O_7$. **d** The unit cell of the $Ca_3Ru_2O_7$ (space group #36, $Bb2_1m$), from [217].

strongly correlated electrons.

Three distortion modes, illustrated in Figure 5.2, describe how the $Ca_3Ru_2O_7$ crystal structure is generated from its parent structure in the $I4/mmm$ space group. The modes are labelled according to the irreducible representation of the parent symmetry group to which they belong[6] [159, 229].

The in-plane octahedral rotation mode X_2^+, and the out-of-plane octahedral tilt mode X_3^- define the space group of $Ca_3Ru_2O_7$ as #36, $Bb2_1m$ [212, 230–232]. These two modes are not polar in themselves, but when they appear together there is a symmetry-allowed coupling to a polar Γ_5^- distortion mode of the Ca ions [230]. The in-plane rotation, X_2^+, rotates the octahedra around the c-axis of the crystal, in the opposite sense for in-plane neighbours as shown in Figure 5.2a, but the same sense for the vertically stacked octahedra in a bilayer [231, 233]. This rotation doubles the unit cell as compared to the high-symmetry one, and rotates it by 45°. It also allows for a pronounced orthorhombic distortion to set into the structure, differentiating the in-plane a and b crystallographic axes.

---

[6]In the Miller and Love notation [229] the letter denotes the **k**-vector of the irrep in the first BZ, $\pm$ is the sign of the inversion parity with respect to the origin, and the subscript number is just used to differentiate irreps at the same **k** without particular meaning.

The out-of-plane, X_3^-, mode will prove very important later on. As seen in Figure 5.2b, the two octahedra sharing a central apical oxygen in the bilayer tilt along the a axis in a hinge-like manner, such that the outer apical oxygens displace one way, while the central apical oxygen displaces in the opposite direction [233]. This induces a local polar distortion, with the effective dipole coming from the fact that two negative oxygen ions were displaced in, e.g. the $+a$ direction, while only one was displaced in the $-a$ direction. Considering this as a single site of the perovskite bilayer, the neighbouring bilayer sites hinge in the opposite sense along the a-axis. The alternating direction of the tilts leads to an antipolar ordering of the local dipoles [231, 232]. Therefore, no global net polar distortion is induced by the X_3^- tilt mode.

The crystal structure is, however, not only non-centrosymmetric, but also polar [217]. The polar distortion is set by the Γ_5^- mode (Figure 5.2c) which defines displacements of the Ca ions along the b-axis of the structure. The Ca ions in the outer CaO_2 planes of the perovskite bilayers (belonging to the rocksalt layer as well) displace in one direction along the b-axis, while the Ca ions in the middle of the bilayer displace in the opposite direction [233]. This creates a local polar distortion, much like the apical oxygens in the tilt mode did along the a-axis. However, since the Ca atoms displace in the same direction throughout the bilayer and in the same sense in both bilayers of the unit cell, there is now a net polar axis in the structure along the b direction [231, 232]. The way in which this polar mode couples to the two non-polar octahedral rotations is the basis for the theory of hybrid improper ferroelectrics, originally based on an insulating sister compound with the same structure, $Ca_3Ti_2O_7$ [212, 230, 231]. Unlike the titanate compound, $Ca_3Ru_2O_7$ is not an insulator, but a metal, preventing it from becoming a ferroelectric with a developed electric dipole of the unit cell. Instead, the itinerant electrons screen the internal electric fields although a robust polar distortion remains present in the structure, making $Ca_3Ru_2O_7$ one of the rare "polar metals" [234–239].

As a general observation, higher temperature tends to increase the symmetry of the lattice. Indeed, while the ruthenate and titanate compounds have only been reported in the distorted $Bb2_1m$ structure, the sister compound $Ca_3Mn_2O_7$ has a high-temperature transition into the parent $I4/mmm$ structure [240]. A temperature dependent structural study [217] reveals this tendency in $Ca_3Ru_2O_7$ as well, as seen in Figure 5.3. At temperatures
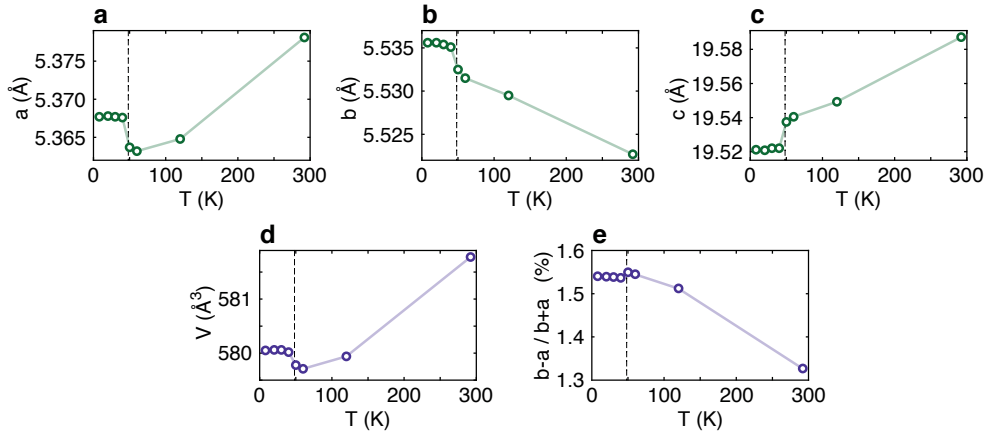
Figure 5.3: **Temperature dependence of the crystal structure.** The changes of the lattice parameters: **a** a, **b** b, and **c** c, **d** the unit cell volume, and **e** the orthorhombicity factor $(b-a)/(b+a)$, with temperature from 8 K to room temperature. The temperature $T_S = 48$ K of the phase transition is indicated as a dashed line. Data adapted from [217].

above 50 K, the unit cell volume slowly increases, and the lattice parameters change so that the orthorhombicity of the structure is reduced with the increase of temperature. However, this change still remains rather small on the absolute scale of the orthorhombic distortion, with the orthorhombicity factor $(b-a)/(b+a)$ (Figure 5.3e) only changing between approximately 1.55 % and 1.35 % from 50 K to room temperature, always retaining relatively large values.

A more abrupt structural change, however, can be seen in Figure 5.3a–d at lower temperatures. At the temperature of $T_S = 48$ K there is a sudden change in the lattice parameters, whereby both in-plane lattice parameters increase upon cooling, while the c-axis reduces, together giving a total volume increase to the unit cell. Below this transition, the structure hardly changes any more with further cooling, and the orthorhombicity is set in the low-temperature phase at ≈ 1.55 %. It is also worth noting that the same neutron scattering study measured no appreciable distortion of the RuO_6 octahedra themselves down to base temperature of 8 K [217]. This transition is isostructural, squashing the unit cell along the c-axis without any change in the symmetry of the structure. It is also intimately coupled to a magnetic and an electronic transition occurring at the same temperature, as they are described below.

5.2   Magnetic order

The magnetic moment in $Ca_3Ru_2O_7$ comes predominantly from Ru $4d$ electrons. Ru is present in the $+IV$ oxidation state, as Ru^{4+} ions with the electronic configuration of $[Kr]4d^4$. As the Ru ions sit in an octahedral environment formed by the oxygen atoms, the octahedral crystal field splits the Ru $4d$ atomic levels, raising the e_g, and lowering the t_{2g} manifold energies [163, 210]. This configuration yields a low-spin state, with the four $4d$ electrons partially filling the three t_{2g} orbitals, leaving two unpaired electrons per Ru atom aligned [163, 245] as illustrated in Figure 5.4a. Elastic and inelastic neutron scattering experiments measure the total magnetic moment to be 1.59 μ_B [217] and 1.8 μ_B per Ru [246], respectively, while magnetisation saturation experiments yield 1.73 μ_B per Ru [247], indicating that this electron configuration provides a good approximate description of the physical reality. The discrepancy would suggest that a truly localised picture of the magnetic moment is not fully valid here and that the electrons responsible for magnetism have partially itinerant character as well.

At high temperatures $Ca_3Ru_2O_7$ is thus a paramagnet, ordering antiferromagnetically upon cooling below the Nèel temperature of $T_N = 56$ K [241, 247–250]. The Ru magnetic moments order ferromagnetically within the bilayers, but antiferromagnetically between bilayers [217, 241–243] as shown
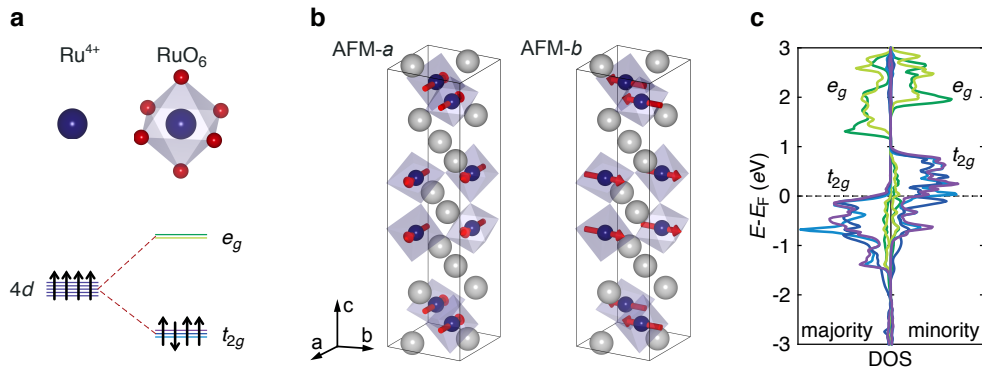

Figure 5.4: **Spontaneous magnetic order in $Ca_3Ru_2O_7$. a** Diagram of the crystal field splitting of the Ru $4d$ states in the octahedral environment of RuO_6. **b** $Ca_3Ru_2O_7$ orders in two antiferromagnetic phases, AFM-a and AFM-b, with ferromagnetic coupling within the bilayers and antiferromagnetic coupling between the bilayers [217, 241–243]. Data adapted from [244], originally measured by [217]. **c** Density of states calculation of the Ru $4d$ electrons confirms the crystal field picture, shown here separately for the minority- and majority-spin projections within a ferromagnetic bilayer.

in Figure 5.4b. Thinking of the perovskite bilayers as magnetic units, this magnetic structure is also described as the A-type antiferromagnet, or by a $(0, 0, \pi/2)$ ordering vector. At the temperature of the Nèel transition, the easy magnetic axis is along the short axis of the structure, and so the magnetic moments align with the a crystal axis [241–243] (AFM-a in Figure 5.4b). Upon further cooling, $Ca_3Ru_2O_7$ goes through a spin-reorientation transition, whereby the sense of the magnetic ordering is preserved, but the easy axis changes. The magnetic moments simply reorient to the b crystal direction [241–243] (AFM-b in Figure 5.4b). The spin reorientation occurs at T_S, together with the isostructural transition described before.

As discussed below, we performed DFT calculations of the $Ca_3Ru_2O_7$ band structure. It is worth noting here that in the magnetically ordered phase we predict a magnetic moment of 1.8 μ_B per Ru, in good agreement with the experiments and previous work. The calculations also predict the configuration with magnetic moments oriented along b to be the lowest energy state. As mentioned in Section 3.2, DFT is a ground-state technique, so it cannot by itself determine why the magnetic easy axis is oriented along the a axis at higher temperatures. However, we know this to be the case, and then DFT can give us valuable insights into the nature of the transition, as I will show in Section 5.7. The density of states obtained from the calculation is shown in Figure 5.4c. It predicts predominantly Ru t_{2g} electrons at the Fermi level in an almost half-metallic configuration with an exchange splitting of ≈ 1 eV. This supports the itinerant picture for the Ru t_{2g} electrons, with the two unpaired electrons ferromagnetically aligned.

5.3   Transport properties

The transport properties of a material depend on its electronic structure at the Fermi level [48]. As seen in Figure 5.5a, the absolute values of in- and out-of-plane electrical resistivity show a resistivity anisotropy of two orders of magnitude [251, 252], revealing highly two-dimensional transport in $Ca_3Ru_2O_7$. I will focus on the in-plane behaviour, dominated by transport within the perovskite bilayers.

At high temperatures $Ca_3Ru_2O_7$ is metallic, with the resistivity decreasing linearly with decreasing temperature. Such T-linear resistivity behaviour has been the subject of much discussion in the community, due to its disagreement with Landau's Fermi liquid theory, which predicts a
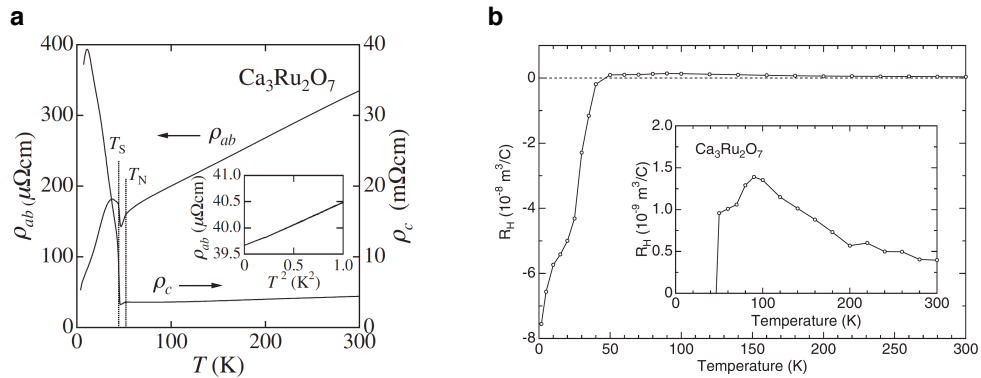
Figure 5.5: **Electronic transport in $Ca_3Ru_2O_7$. a** Resistivity measurements in the *ab* plane and along the *c* axis, adapted from [252]. Inset shows the resistivity is proportional to T^2 below 1 K. **b** Hall coefficient measurement, adapted from [256].

T^2 dependence of resistivity as pointed out in Section 2.3. This type of non-Fermi liquid behaviour is famously seen in the normal state of high-T_C cuprate superconductors at optimal doping [253, 254], near candidate quantum critical points [254, 255]. The fact that $Ca_3Ru_2O_7$ exhibits this type of behaviour makes its high-temperature phase interesting for further study, but is beyond the scope of this thesis.

Cooling through the Nèel transition leads to a minor dip in resistivity, expected as the spin-fluctuation scattering channels are frozen out. Lowering the temperature further, the material goes through the coupled isostructural and spin-reorientation transition at T_S, discussed above, upon which the resistivity exhibits a sudden jump. The temperature dependent Hall coefficient [256], shown in Figure 5.5b, also shows a sharp change of both sign and magnitude at T_S. Below the transition, the resistivity starts to increase with cooling, showing a local maximum at ≈ 30 K. The phase transition at T_S has often been discussed as a metal-insulator transition [247, 257–259], and the temperature region between 30 K and T_S as an insulating phase of $Ca_3Ru_2O_7$. This is controversial in the literature [252, 260–263], as $Ca_3Ru_2O_7$ is assumed to be a low-carrier density semimetal with multiple types of carriers below T_S. Transport properties of such systems depend on the temperature dependence of the concentrations and mobilities of different carrier types. They can result in complex, and even non-monotonic gradual[7] changes of the resistivity with temperature. At very low tempera-

---

[7]This cannot cause sharp changes of resistivity though. The sudden jump at T_S is due to the phase transition.

tures the resistivity assumes a $\propto T^2$ Fermi liquid behaviour, as seen in the inset of Figure 5.5a. The observation of quantum oscillations [252] confirms the presence of Landau quasiparticles in this regime.

The phase transition at T_S therefore likely has an electronic aspect, along with the structural and magnetic ones discussed above, making $Ca_3Ru_2O_7$ an interesting platform to study the interplay of all these degrees of freedom in a single phenomenon.

5.4   Methods

The samples I used in the experiments came from Dr. Dmitry Sokolov, our collaborator at the Max Planck Institute for Chemical Physics of Solids in Dresden, Germany. They were grown using the floating zone method in a mirror furnace, according to an established procedure [264, 265]. The growth atmosphere was an Ar and O_2 mixture in an $85 : 15$ ratio. The grown rods are brittle and are shattered post-growth into smaller crystals. I chose high-quality single crystals from several growth batches, with a typical size of $\gtrsim 1 \times 1$ mm^2, with an example shown in Figure 5.6a. $Ca_3Ru_2O_7$ single crystals grow with antiphase domains, in which the a and b crystal axes are interchanged as shown schematically in the insets of Figure 5.6a, but the space group in both domains remains $Bb2_1m$[8] [231]. The antiphase domains can be seen under an optical microscope, using polarised-light microscopy, as displayed in Figure 5.6a. I cannot exclude the presence of micro-domains in our samples, but we can put an upper limit on their size to 500 nm, set by the resolution of the optical microscope. I used only the samples in which I had observed the domain structure to be the same on both ab-plane surfaces of the crystal. I oriented the crystals using the fact that the antiphase domain boundaries occur along the (110) direction (corresponding to (100) of the parent tetragonal structure) [231, 243, 266], and used the domain boundaries as guides for cutting the crystal with a wire saw into 500×500 μm^2 single-domain squares. The crystals were cut with a standard wire saw, and the cut pieces sonicated in acetone for 30 minutes to remove the slurry without any further damage to the crystals.

An independent check can be performed during the ARPES measurements by the symmetry of the Fermi surface. I will discuss the Fermi surface

---

[8]These are not to be confused with the orthorhombic polar twin, which has the space group $A2_1am$. There the axes stay where they are but both octahedral distortion mode irreps, X_2^+ and X_3^-, are taken around the a, instead of the b axis [231].
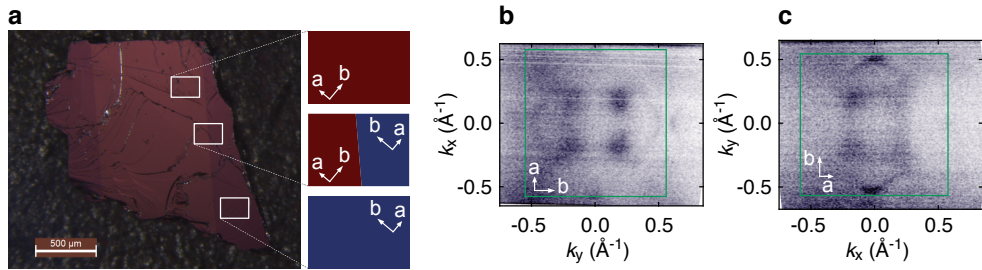
Figure 5.6: **Antiphase domains in single crystals of $Ca_3Ru_2O_7$. a** Image of a typical raw single crystal of $Ca_3Ru_2O_7$ taken under a polarised-light optical microscope. The difference in hue at the surface of the crystal indicates different antiphase domains, where the a and b axes of the crystal have been interchanged as shown in the diagrams. **b,c** Fermi surfaces displaying two-fold rotational symmetry, measured on the same single-domain crystal, upon rotating the sample by 90°.

at length below, but it is sufficient to observe here that the constant energy cuts display a strong two-fold symmetry. If the samples contained a significant amount of both antiphase domains on the length scale smaller than the diameter of our beam (Figure 3.6), the photoemission intensity coming from both domains would overlap, and therefore appear fourfold symmetric. Rotating the sample by 90° results in the corresponding rotation of the features in the constant energy cuts (Figure 5.6b,c), eliminating the possibility that the two-fold symmetry comes from photoemission matrix elements effects. Rather, it follows the underlying symmetry of the lattice.

The experiments themselves were performed at the BLOCH beamline of the Max-IV synchrotron in Sweden [119], and the I05 beamline of Diamond Light Source in the UK [118]. In order to find suitable measurement conditions for visualising the band structure (those that maximise the photoemission matrix element contributions described in Section 3.1.1), we have performed test measurements at a series of photon energies in the 20–100 eV range and with different polarisations of the light. The data were collected using 22 eV p-polarised light, with some datasets taken using s-polarised light to better highlight weak band features (due to symmetry effects on the matrix elements, Section 3.1.1). A detailed study of the photon energy dependence of the band structure may however yield further improvements. To collect data from a particular direction in momentum space, we first need to ensure that the crystal is correctly aligned with respect to the entrance slit of the analyser as discussed in Section 3.1.2. However, extremely low signal intensity of the low-energy bands and the lack of distinct fea-

93

tures in most of the Brillouin zone make precise alignment of $Ca_3Ru_2O_7$ samples challenging and laborious. Temperature dependent data were reproduced on both synchrotrons, using multiple samples, and in both heating and re-cooling cycles, ensuring that the effects presented below are intrinsic, rather than artefacts of the setup, crystal quality, or sample ageing due to temperature cycling.

To gain further insights, we employed density-functional theory as introduced in Section 3.2. I performed a series of calculations within the WIEN2k formalism [134], converged on a **k**-mesh of $5 \times 5 \times 5$ **k**-points. However, after we had noticed slight numerical inconsistencies in the calculations, most of the calculations were repeated by Dr. Helge Rosner, our DFT specialist collaborator, using the FPLO code [136] and a **k**-mesh of at least $16 \times 16 \times 6$ **k**-points. These additional calculations showed only minor discrepancy with mine, confirming all the findings of my calculations, and we were able to identify the numerical inconsistencies as being due to the sparsity of the **k**-mesh I used[9]. The data presented in this thesis therefore comes from my calculations, unless explicitly stated otherwise.

All calculations used experimentally derived crystal structures at various temperatures from Yoshida *et al.* [217], fully including spin-orbit coupling unless otherwise stated. I used the local spin density approximation (LSDA) exchange-correlation functional (LDA for spin polarised calculations), and Perdew-Burke-Ernzerhof (PBE) [132] as the most established functional in the GGA family. All the reported data were calculated with the LDA functional, unless explicitly stated otherwise, in which case I will discuss the implications of using different exchange-correlation functionals.

Magnetic order was simulated as ferromagnetic throughout the unit cell rather than using the true, antiferromagnetic order, which makes the calculations much faster and easier to perform. In the AFM case, the Ru atoms bearing opposite magnetic moment need to be separately defined in the input structure of the calculation, and the antiferromagnetic space group symmetries need to be carefully taken into account. The increased number of atoms and the decreased symmetry constraints make the antiferromagnetic calculations particularly difficult and computationally demanding if they are to converge correctly. Considering the ferromagnetic alignment of the spins within the perovskite bilayers [217, 242, 243], and very weak inter-bilayer

---

[9]Unfortunately, much denser **k**-meshes were unavailable to me, due to restrictions in computational resources.

coupling which is seen in transport measurements, the FM calculations are expected to reproduce all the key aspects of the band structure. This assumption has already been shown to work [258, 267], and is corroborated by the broad agreement between our calculations and the experimentally measured electronic structure shown below.

5.5   Low-temperature electronic band structure

The calculated total density of states (DOS) across a relatively broad energy range around the Fermi level is shown in Figure 5.7a. The orbitally projected DOS calculation (Figure 5.7b) puts the Ru t_{2g}-derived bands at the Fermi level, in accordance with the crystal field argument for a Ru^{4+} ion in an oxide octahedron made before, and illustrated in Figure 5.4a. Furthermore, the crystal field has pushed the e_g states well above the Fermi level, separating them completely from the t_{2g} manifold with a well defined gap. An angle-integrated photoemission spectrum, shown in Figure 5.7c, measures the DOS directly. The Ru e_g states are inaccessible to conventional photoemission experiments, but below the Fermi level we find a broad band corresponding to the Ru t_{2g} states, followed by a high-intensity man-
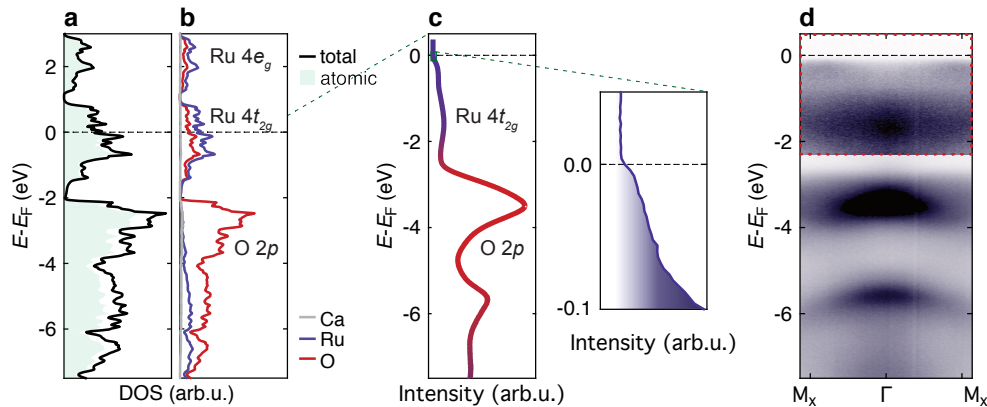

Figure 5.7: **Valence band density of states. a** Total density of states (DOS) calculated by LSDA+SOC. The shading indicates the DOS within the atomic spheres of the augmented plane wave basis (APW). **b** Atomically resolved DOS shown for the same axis scaling. **c** Angle-integrated photoemission measurement reveals a similar structure of the valence bands. Inset at the Fermi level reveals very low quasiparticle residue, in good agreement with a previous study [260]. **d** The angle-resolved photoemission dispersion shows only very broad features with little dispersion. Due to large variation in the measured intensities of the bands, the region around the Fermi level is shown with increased contrast for clarity.
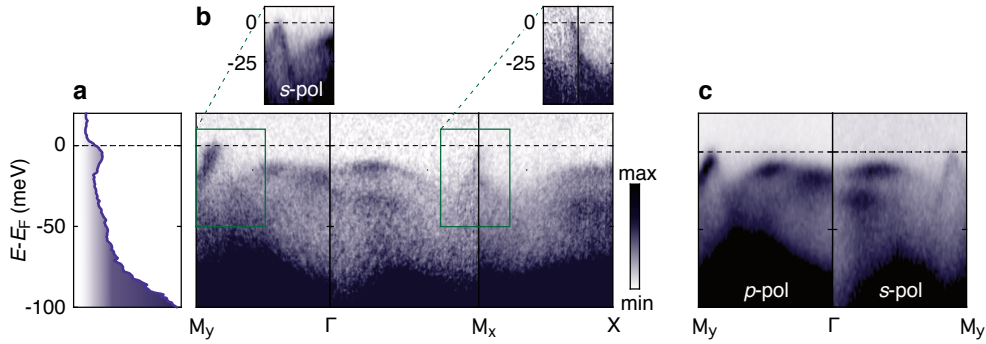
Figure 5.8: **Low-energy electronic structure. a** An EDC taken at k_F along the $M_y - \Gamma$ direction shows a quasiparticle peak. **b** ARPES measurements show coherent quasiparticle dispersions along the $M_y - \Gamma - M_x - X$ path of the surface projected Brillouin zone. Insets better illustrate the bands crossing the Fermi, along $M_y - \Gamma$ by using data collected with s-polarised light, and along $M_y - \Gamma$ by using the data from the second Brillouin zone and higher intensity contrast for clarity. **c** The $M_y - \Gamma$ high-symmetry line is shown as measured using s and p linearly polarised light.

ifold identifiable as O $2p$ in origin. We find that our calculated density of states shows excellent agreement with the measurements, and confirms the assigned character of the observed bands. Figure 5.7d shows an angle-resolved measurement for the same energy range, with the measured bands appearing as very broad, incoherent features. Looking at a narrow energy range below the Fermi level in the inset of Figure 5.7c, we can barely see a quasiparticle peak before the strong incoherent intensity sets in at about 100 meV.

The angle-resolved measurements of the same low-energy range, shown in Figure 5.8, display well defined quasiparticles to binding energies of ≈ 50 meV, albeit with very low intensity. Figure 5.8a shows an example of a quasiparticle peak in this region. I can estimate the value of the quasiparticle residue as $Z \approx \left(1 + v_F^* / v_F^{\mathrm{DFT}}\right)^{-1} = 0.15$ from the extent of mass renormalisation between the measured bands and the DFT calculation, which will be detailed below. Such a small value of Z suggests a high degree of electronic correlation. It also causes considerable experimental difficulty for the ARPES measurements, requiring high-quality crystals and long acquisition times to improve the signal-to-noise ratio, as well as very high energy resolution (< 2 meV on both beamlines where the experiments were performed) to clearly resolve the band features.

The dispersions in Figure 5.8b are very different for the $M_y - \Gamma$ and $M_x - \Gamma$

high-symmetry directions leading to a pronounced two-fold symmetry in the Brillouin zone. There are three main distinct band features to notice: a steep band crossing the Fermi level close to the zone boundary along the $M_y-\Gamma$ line, a small electron-like band crossing the Fermi level around the M_x point, and relatively flat, M-shaped bands near the zone centre. A previous ARPES study [260] has identified these, and our measurements mostly agree with their findings on the low-temperature electronic structure. However, the technical advances of the ARPES experiments in the past 10 years and a careful selection of only single-domain samples for the experiments allow us to better resolve weak features at small energy scales such as are present in $Ca_3Ru_2O_7$, and develop a better understanding of the underlying band structure. A concurrent ARPES study to mine [263] appeared as preprint as I was writing the thesis, with high-quality data identifying the same features in the low-temperature electronic structure. However, their focus is slightly different, disregarding the M-shaped bands at the Brillouin zone centre, leading them to an electron-nematic interpretation of the T_S phase transition. I will comment on this further, after presenting my own results.

The steep band crossing the Fermi level along $M_y - \Gamma$ is seen to have a partner with roughly the same k_F, but opposite v_F. Together they form a Λ-shaped hole-like band, offset from the Brillouin zone boundary, whose band top just reaches the Fermi level. The two sides of this Λ-shaped band show up with very different intensities when p-polarised light is used, but exhibit similar, if weaker, intensities with s-polarised light making them easier to observe (Figure 5.8c). Along the $M_x - \Gamma$ high-symmetry direction, a shallow electron-like band crosses the Fermi level. With a binding energy of $\lesssim 15$ meV, its band bottom reaches towards the top of a hole-like band dispersing further downwards below it. The inset in Figure 5.8b also shows slightly different k_F values for the band along the two different high-symmetry directions. Finally, there is a set of relatively flat bands reaching $\lesssim 10$ meV below the Fermi level around the centre of the Brillouin zone. Using different light polarisations we can identify at least three hole-like bands in that set, dispersing up towards the Fermi level before levelling off into an M-shaped band top.

In Figure 5.9, I compare the experimental results to my *ab initio* band structure calculations. Figure 5.9a first shows the raw calculated band structure, which is then overlaid on the experimental data for comparison in Figure 5.9b. Due to electronic interactions, the experimental band structure
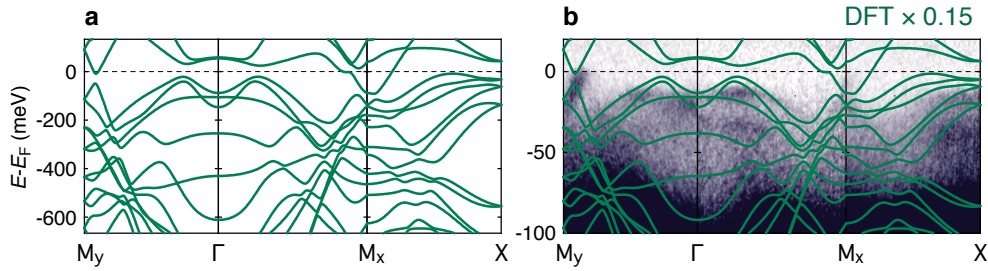
Figure 5.9: **Band structure calculated by density-functional theory.
a** The LSDA+SOC calculated band structure along the $M_y - \Gamma - M_x - X$ high-symmetry lines near the Fermi level. **b** The same data is shown again overlaid over the experimental band structure. The DFT calculation has been uniformly renormalised to account for the correlation effects, by a factor of 0.15, which provided the best overall fit to the experimental data.

is strongly renormalised as compared to the bare dispersions obtained from DFT calculations. However, we find good agreement of the calculations with the experimental data upon simple uniform scaling of the calculated bands. In order to approximately account for the strong mass renormalisation, I rescale the energy of the calculated bands by a factor of 0.15, indicated above Figure 5.8b, corresponding to an average effective mass increase by a factor of ≈ 7. This value was used earlier to estimate the quasiparticle residue, Z. Detailed fits of the steep Λ-shaped bands near M_y indicate that its effective mass is only ≈ 4 times larger than that of the bare band, while the M-shaped bands at zone centre require much larger renormalisation. This points to highly orbitally and **k**-dependent mass renormalisation effects in $Ca_3Ru_2O_7$, which DFT does not capture. First-principle studies that better capture many-body effects have have been performed on its single-layer sister compounds [116, 227, 268], showing promise in capturing such phenomena.

Nonetheless, our DFT calculations already offer sufficiently good agreement with experiments to allow useful further insights. To begin with, the DFT calculations also display a strong two-fold symmetry in the Brillouin zone, indicating that the origin of this symmetry lies in the orthorhombic nature of the structure, rather than it being driven by electronic interactions as proposed in a recent study [263]. The authors of that paper make the same claim regarding the asymmetry of the electron pocket around M_x seen in the inset of Figure 5.8b. However, my non-interacting calculations also predict that pocket to be asymmetrical, as seen from the different k_F values
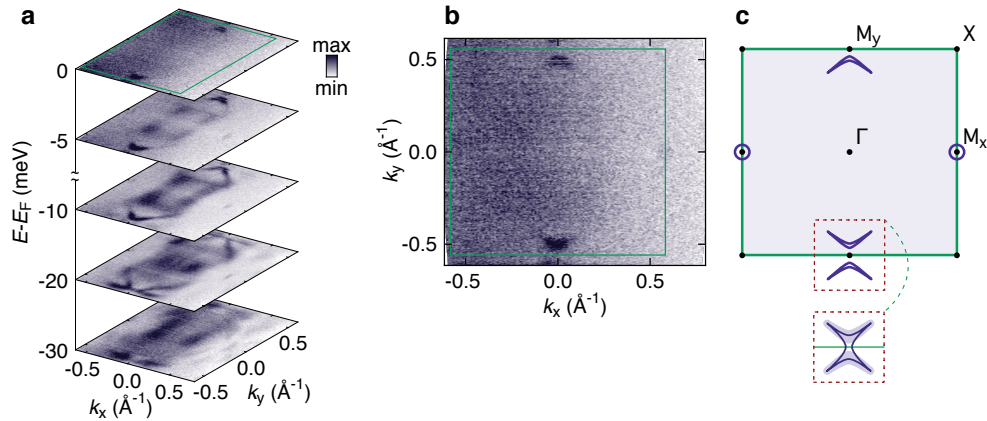
Figure 5.10: **Fermi surface at low temperatures. a** Constant energy cuts of the full Brillouin zone of $Ca_3Ru_2O_7$ with a 2 meV energy integration window. **b** Fermi surface map with the indicated surface projected Brillouin zone outline. Small boomerang-shaped pockets observed near the BZ edge along $M_y - \Gamma$, and weak-intensity circular pockets around the M_x point. **c** A schematic of the Brillouin zone with the Fermi pockets. The inset demonstrates the difference in the this Fermi surface, with two "boomerang"-shaped hole pockets, and the one obtained from a two-band, d_{xz} and d_{yz}, model, with a single star-shaped hole pocket, proposed by Kikugawa *et al.* [252].

of the electron pocket along $M_x - \Gamma$ and $M_x - X$ in Figure 5.9. The calculations also successfully predict the Λ-shaped band along $M_y - \Gamma$, displaced from the zone boundary, even though they place the band maximum below the Fermi level, with its electron-like partner crossing E_F instead. Finally, the calculations show the M-shaped band top at the Brillouin zone centre to be the result of several electron- and hole-like bands hybridising near the Fermi level, producing this characteristic shape. This hybridisation will feature heavily later in the Chapter, as it appears to play a crucial role for much of the complex physics in the T_S phase transition of $Ca_3Ru_2O_7$.

For the moment, however, I will focus on the bands crossing the Fermi level, as they are responsible for the electronic behaviour at low temperatures. Transport measurements shown above indicate the low-temperature electronic state of $Ca_3Ru_2O_7$ is a very low carrier density Fermi liquid, showing parabolic increase of resistivity with temperature (Figure 5.5), proven by quantum oscillations measurements [252]. A constant-energy ARPES map in Figure 5.10b allows us to image the Fermi surface directly. Along $M_x - \Gamma$, an electron pocket appears around the M_x point. It is weak in intensity, but just visible in the measured data. A narrow, boomerang-shaped

hole pocket near M_y is formed as the top of the Λ-shaped band, which just crosses the Fermi level and disperses diagonally towards M_x. This firmly establishes $Ca_3Ru_2O_7$ at low temperatures as a low carrier density semimetal, with both electron and hole carriers.

Such structure of the Fermi surface could account for the relatively large absolute value of the Hall coefficient [256] below T_S in Figure 5.5b. A temperature-dependent evolution of the chemical potential, which may be expected to have noticeable impact in such a system, can also explain the non-monotonic behaviour of resistivity [251, 252], as well as why T^2 dependence may not be established until very low temperatures. Quantum oscillations in magnetotransport indicated small electron and hole Fermi pockets [249, 252, 269], while the scale of the crossover from weak- to strong-field magnetoresistance implies the presence of sharp corners in the Fermi surface [252].

These observations were explained by Kikugawa *et al.* [252] in terms of an effective two-band model of the Fermi surface, where only Ru d_{xz} and d_{yz} bands cross the Fermi level. That model agrees with our schematic of the Fermi surface in Figure 5.10c in all but one aspect, the exact shape and connectivity of the hole-like Fermi pocket. The hole pockets in my results are "boomerang"-shaped and centred away from the Brillouin zone edge, resulting in two hole pockets within each Brillouin zone. In contrast to that, this two-band model predicts that the two "boomerang" pockets near the same M_y point are joined across the zone boundary into a single, larger hole pocket centred at that M_y point, as illustrated in the inset to Figure 5.10c, yielding only one full hole pocket per Brillouin zone. However, the gap across the Brillouin zone boundary is too small to be easily detectable in transport measurements, making the transport results consistent with the ARPES maps and the three band model as well.

The band structure of $Ca_3Ru_2O_7$ can be thought of as coming from a square net layer of Ru atoms with O atoms bridging them. This is then doubled for the bilayer, and doubled again for the minority- and majority-spin due to the AFM magnetic order, with each of these causing a splitting on a characteristic energy scale. The rotations of the octahedra cause a doubling of the unit cell with a 45° rotation, leading to backfolding of the bands in the reduced Brillouin zone. As a result, we have a complex band structure of the t_{2g} manifold around the Fermi level. Figure 5.11 shows my DFT calculations for the whole Ru t_{2g} manifold, with projected orbital character. I
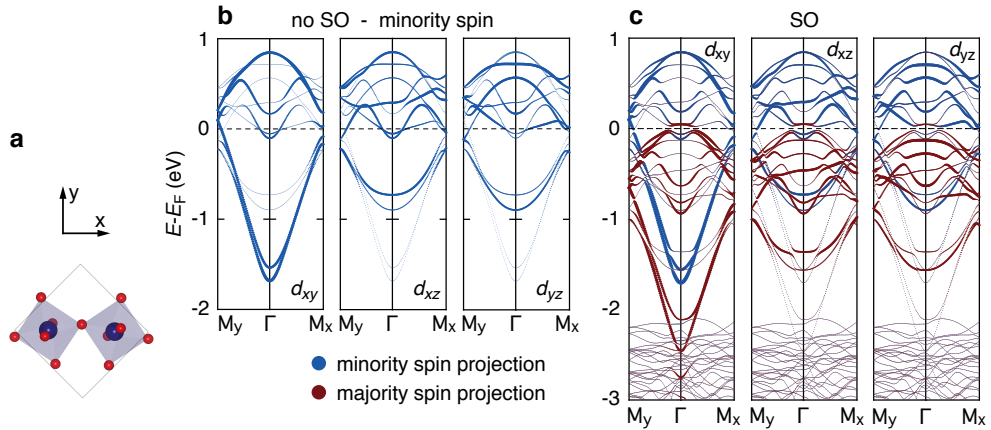
Figure 5.11: **Orbital character of the bands in the Ru $4t_{2g}$. a** The local coordinate system for the orbital quantisation is chosen as that of the parent tetragonal structure. This would align the coordinate system's axes with the Ru–O bonds of the octahedra, in absence of the any octahedral rotations or tilts. **b** For clarity, the projections on the three Ru $4t_{2g}$ orbital characters are first shown only for the minority-spin bands calculated without spin-orbit coupling. **c** The projections in the full LSDA+SOC calculations, with the colour indicating spin orientation.

chose the coordinate system for the orbitals to be aligned with the tetragonal parent unit cell, as those are parallel to the axes of the undistorted octahedra. Therefore, a small degree of mixing of the pure orbital basis as given by the octahedral crystal field at the Ru site can be expected due to rotations and tilts of the octahedra. Orbitally dependent correlations could, in reality, reduce the bandwidth of the d_{xy} band as compared to the DFT calculation, as in the case of the single-layer compound Ca_2RuO_4. There it has been established that LDA underestimates the occupancy of the d_{xy} orbital, and that computational techniques which take interactions into account are necessary in order to get a reliable picture of orbital character within the t_{2g} manifold [226, 227, 270], showing the d_{xy} orbital to be fully occupied and not contributing to the Fermi surface.

Nevertheless, as noted above, the Fermi surface of $Ca_3Ru_2O_7$ does not agree with the predictions of such a two-band model. To understand this discrepancy, I investigate the orbital character of the bands that form the hole Fermi surface, i.e. the Λ-shaped band. The different behaviour of the matrix elements with light polarisation in the two branches of the Λ-shaped band along the $M_y - \Gamma$ line, as seen in Figure 5.8c, would suggest that these branches differ in their orbital composition. This is confirmed

by the orbital character projections in my DFT calculations in Figure 5.11, where one branch of the Λ-shaped band is indeed of d_{xz} and d_{yz} character, while the other is purely d_{xy}. The d_{xy} band at the Fermi level separates the hole pocket of the two-band model (inset of Figure 5.10c), into the experimentally observed thin "boomerang"-shaped Fermi pockets. In $Ca_3Ru_2O_7$, therefore, bands containing contributions from all three t_{2g} orbitals cross the Fermi level, and contribute to the Fermi surface and to transport and thermodynamic properties. The d_{xy} orbital character also bears significant weight in the flat states at zone centre. Those indeed do not cross the Fermi level at low temperatures, but will have a vital role at the phase transition, as is demonstrated below.

5.6 Temperature dependent electronic structure

With an understanding of the low-temperature electronic structure established in Section 5.5, I now turn to its temperature dependence, and in particular, to the changes in the electronic structure across the isostructural
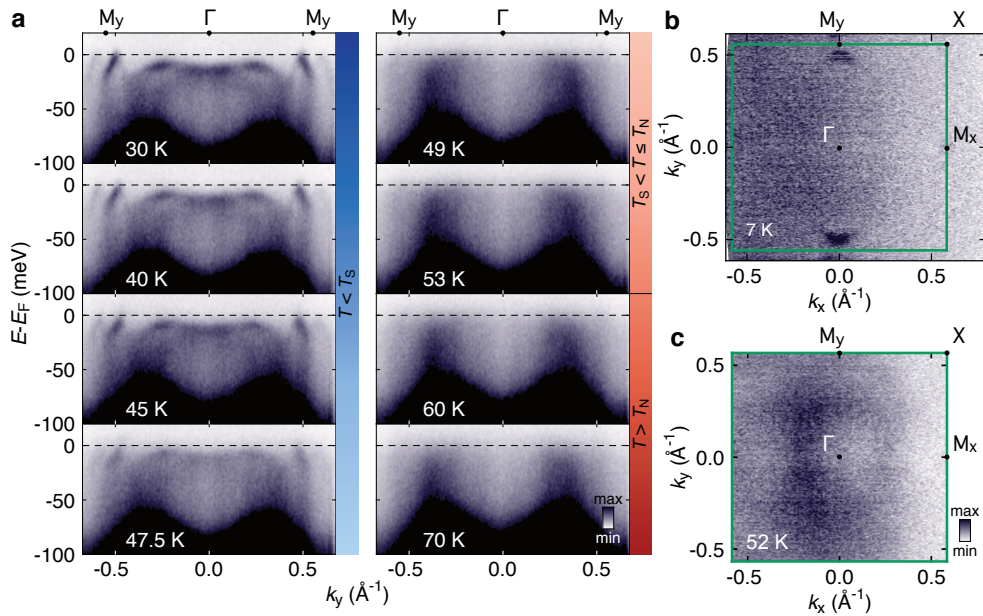

Figure 5.12: **Temperature dependence of the low-energy electronic structure of** $Ca_3Ru_2O_7$**. a** A series of experimental dispersions along the $M_y - \Gamma$ direction for temperatures varying across both T_S and T_N phase transitions. While dramatic changes occur at T_S, we observe no qualitative change to the band structure at T_N. **b,c** Measured Fermi surfaces for the: **b** $T < T_S$ and **c** $T_S < T < T_N$ phases, demonstrating the appearance of a large Fermi pocket around the zone centre at temperatures above T_S.
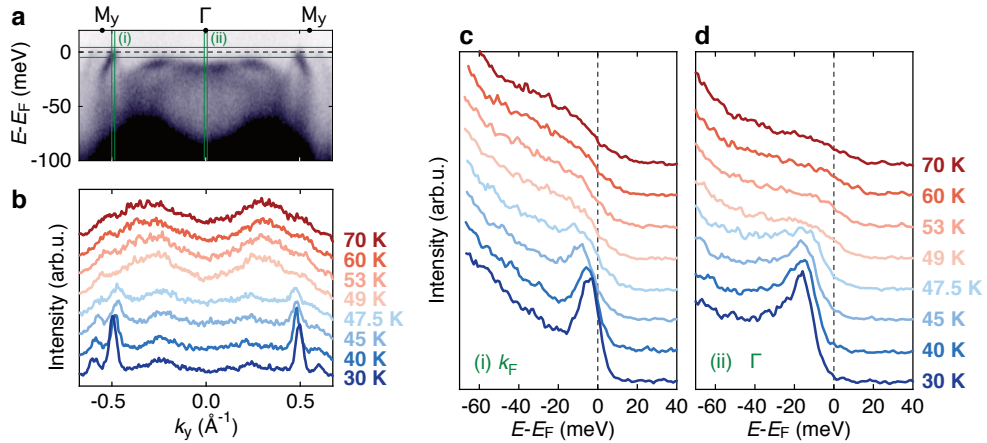
Figure 5.13: **Temperature dependent key momentum- and energy-distribution curves. a** An example dispersion from Figure 5.12a, indicating the integration regions for the extracted temperature-dependent distribution curves. **b** Temperature-dependent MDCs at the Fermi level from the temperature dependent dispersions in Figure 5.12a. **c,d** Temperature-dependent EDCs at: **c** k_F of the Λ-shaped band, and **d** at Γ.

and spin-reorientation transition at T_S. A series of temperature dependent $M_y - \Gamma$ dispersions are shown in Figure 5.12a, from which I extract some key momentum- and energy-distribution curves in Figure 5.13. To improve the signal-to-noise ratio, the distribution curves are integrated within a small range around the desired position: ± 2 meV for the MDCs, and ± 8 mÅ^{-1} for the EDCs.

The bands display two main changes as the temperature of the sample goes through T_S. Firstly, their linewidths suddenly increase above the transition, and all the features in the dispersions in Figure 5.12a broaden. I can best illustrate this on the Λ-shaped bands. Both the MDCs at E_F (Figure 5.13b) and the EDCs at the k_F of the Λ-shaped bands (Figure 5.13c) show a well defined quasiparticle peak below T_S. Although diminished close to the transition temperature, those peaks persist up to T_S. The EDCs above the transition show no clear peak as the linewidth makes it too wide to be distinguishable. In the MDCs at low temperatures, the Λ-shaped bands give the most prominent peaks, with the neighbouring bands in the second zone also visible, although with reduced intensity. Above the transition these peaks broaden. However, they are still clearly visible as shoulder-features located at the zone boundary. Even though these are not easily discernible in dispersions and Fermi maps, I take this as evidence that the small Fermi pockets of the low-temperature Fermi surface persist to high

temperatures.

The other change is in the dispersion of the hole-like bands at the Brillouin zone centre. Below T_S these are fully occupied, with an M-shaped band top. However, above T_S they cross the Fermi level, leaving no observable flat band at the Γ point. The EDCs at Γ therefore have a clear quasiparticle peak at $\approx$ 15 meV below the transition, which completely disappears above T_S, giving way to broad background intensity with a Fermi cutoff. The MDCs below the transition exhibit some intensity bleeding in closer to the zone centre, coming from the local maxima of the M-shaped bands due to their close proximity to the Fermi level and finite linewidth of the bands. Above T_S these turn into broad peaks with high intensity where the bands now cross the Fermi level. In fact, these changes do not only happen along the $M_y - \Gamma$ high-symmetry line shown in Figure 5.12a, but throughout the Brillouin zone. The hole-like band now crossing the Fermi level at Γ therefore creates a new, large, hole-like Fermi surface in the high-temperature regime, clearly seen in Figure 5.12c.

These measurements also provide insight into the controversial insulating phase in $Ca_3Ru_2O_7$ which I have mentioned above [247, 257–259]. My results demonstrate that $Ca_3Ru_2O_7$ has a Fermi surface at all experimental temperatures. I have observed no insulating phase between 30 K and T_S, and indeed no qualitative differences comparing that data to the electronic structure measured at 6 K. The changes in the electronic structure and the linewidths observed across T_S do, however, directly imply an involvement of the electronic sector in the phase transition, and can be expected to have a significant influence on the transport properties at the phase transition. The size of the Fermi pockets corresponds to the carrier concentration, while the linewidths scale as their scattering rate, as described in Section 3.1.4. To investigate their influence quantitatively, I estimate the transport properties discussed before from my ARPES measurements.

In order to quantify the change in the linewidths, the dispersions from Figure 5.12 are taken as series of MDCs at different energies, to which I then fit Lorentzian peaks (as illustrated in Figure 3.7b). The full width at half maximum, Δk_{FWHM}, of those peaks is proportional to the quasiparticle scattering rate. I show examples of the fits, one for above and one for below T_S, as insets in Figure 5.14. Below the transition I have fit the higher-intensity branch of the Λ-shaped band. We can note from Figure 5.12a that the M-shaped bands show comparable linewidths, but they are more difficult
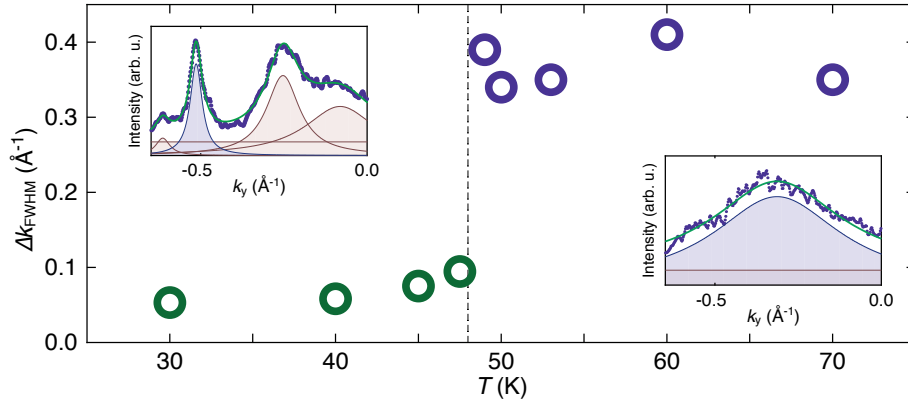
Figure 5.14: **Temperature dependence of the measured linewidths.**
Full-width-half-maxima of Lorentzian peak fits to band features: Λ-shaped
bands forming the boomerang Fermi surfaces below T_S, and the broad band
forming the large Fermi surface above T_S. Typical fits for both temperature
regimes are indicated each side of the main graph.

to fit reliably due to multiple bands being in close proximity. Above the
transition I fit the dominant, hole-like bands close to the Fermi level as they
are the only features prominent enough to yield a reliable fit. I performed fits
on MDCs in a $20-50$ meV range below E_F and then took an average value
to reduce the effects of noise as well as artificial changes of the linewidth
which can occur close to the Fermi level. The well defined quasiparticles
in the low-temperature phase show gradual broadening of spectral features
with increasing temperature, (Figure 5.14 - green symbols), characteristic of
electron-electron and electron-phonon scattering as discussed in Section 2.4.
At T_S, the linewidths suddenly increase, and then show no further change
within experimental uncertainty as the temperature is increased into the
paramagnetic regime. As the linewidths of the spectral function directly
relate to the scattering rates, i.e. lifetimes of the respective states, this
change should have a considerable impact on the resistivity of $Ca_3Ru_2O_7$.

The other big influence on resistivity comes from the carrier concentra-
tions, which correspond to the sizes of Fermi surface pockets, estimated in
Figure 5.15 for the two temperature regimes. Given the difficulty of exactly
judging the sizes of the Fermi pockets in the low-temperature phase due to
their small size and low intensity, I make a rough estimate from the mea-
sured Fermi surface maps. In Figure 5.15a, the electron pockets around M_x
were approximated as circles with a surface area of ≈ 0.0013 Å^{-2}, or 0.09 %
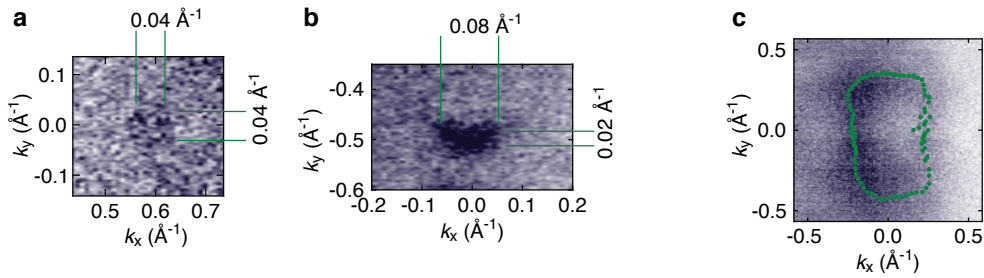of the Brillouin zone, while in Figure 5.15b, the boomerang-shaped hole

Figure 5.15: **Carrier density estimates for the two temperature regimes. a,b** Rough estimates of the sizes of the small Fermi pockets in the low-temperature phase: **a** the electron pocket, **b** one "boomerang"-shaped hole pocket. **c** The high-temperature Fermi surface with the green points indicating the position of radial Lorentzian peak fits, estimating the size and shape of the large Fermi pocket.

pockets were approximated as rectangles with a surface area of 0.0016 $Å^{-2}$, or 0.12 % of the Brillouin zone each. It is particularly difficult to make this estimate for the hole Fermi pockets since the linewidth measured at the Fermi level is greater than the width of the pocket itself. Thus our estimate only represents a crude upper bound. Still, it is in good agreement with the low measured frequencies of the Shubnikov-de Haas quantum oscillations [252, 269], which led to an estimate of the size of the Fermi surface to be 0.2 % of the BZ [247, 249, 269]. The high temperature Fermi surface is much larger, and in order to determine its size I employ Lorentzian lineshape fits to MDCs in the radial directions of the Brillouin zone, as discussed in Section 3.1.4. By integrating the area enclosed by the fitted peak positions, I arrive at the value of 0.33 $Å^{-2}$, corresponding to approximately 25 % of the Brillouin zone size.

Using Luttinger's theorem [125, 126], we can relate the size of the measured Fermi surface pockets to the filling of the bands crossing the Fermi level. In the low-temperature phase, the sizes of electron and hole Fermi pockets are nearly the same, indicating an integer filling. Using the DFT calculations to obtain the number of occupied bands in the Ru t_{2g} manifold (Figure 5.11c), we see that this filling corresponds to 4 occupied t_{2g} electrons per Ru atom, as is expected for Ru^{4+} ions (Figure 5.4a). I use the same method on the high-temperature Fermi surface, i.e. measure the size of the pocket from the experiment and obtain the degeneracy of the hole-like bands that form it from the DFT calculations. This leads to a conclusion that the large Fermi surface which develops above T_S contributes one hole

per unit cell (Figure 5.2d). If the valence of the Ru ions doesn't change at the transition, another change of the Fermi surface is expected, which compensates the electron count by adding one electron per unit cell. A possible way to achieve this would be a shallow electron pocket of the same size, centred at the Γ point, which could be difficult to detect experimentally. This possibility is also suggested by the DFT calculation, which I will discuss further below.

These extracted values of the carrier density, however, allow me to make at least rough estimates of the Hall coefficients in the two temperature regimes. Following Yoshida *et al.* [256], I estimate the Hall coefficients using the weak-field formula for a two-dimensional system with isotropic scattering rate:

$$R_{\mathrm{H}} = \frac{(2\pi)^3 (c/2) \sum_i (\pm 1)^i}{e \sum_i l_i^2},$$

where $c/2$ is the distance between the perovskite bilayers which constitute the 2D conductive sheets, c being the out-of-plane lattice parameter, $(\pm 1)^i$ is the sign of the charge of the carriers for the ith Fermi pocket, and l_i is its circumference. The assumption of isotropic scattering is expected to hold better at low temperatures, where the scattering processes are dominated by impurities, however it provides us with a rough estimate. From our measured Fermi surfaces I obtain $R_{\mathrm{H}}(8K) = -2 \cdot 10^{-7}$ m^3/C and $R_{\mathrm{H}}(52K) = 3 \cdot 10^{-9}$ m^3/C. The agreement with the values in Figure 5.5b is remarkably good, with the measured Hall coefficient values well within the uncertainty of our estimates of the sizes of the Fermi surface pockets. The sharp change of the Hall coefficient at T_{S} can therefore be explained by the sudden appearance/disappearance of the large Fermi surface.

Within the Drude model, the resistivity depends on the ratio of the carrier density and scattering rate [48]. In $Ca_3Ru_2O_7$, the magnitude of the changes across the phase transition at T_{S} in either of those properties individually, would each cause much larger changes to the resistivity than observed in Figure 5.5a. However, occurring coincidentally their effects largely cancel, resulting in a relatively modest resistivity step at T_{S}.

5.7   Magnetic moment orientation dependent band hybridisation

We have seen in the previous Section that the phase transition at T_{S}, along with being an isostructural and spin-reorientation transition, also has a dra-

matic effect on the electronic structure of $Ca_3Ru_2O_7$. In order to see how the changes in the electronic structure relate to the other aspects of the phase transition it is important to understand the origins of those changes, i.e. what causes the band hybridisation which destroys the large Fermi surface upon cooling through T_S. To this end I have performed DFT calculations based on the experimentally determined crystal structures for $Ca_3Ru_2O_7$ at different temperatures [217], as described earlier in Section 5.4.

I have already demonstrated good agreement of the electronic structure calculated for the low-temperature phase with the experiment in Figure 5.8. That calculation uses the experimental crystal structure measured at 8 K, and the magnetic moment fixed along the crystal b axis, modelling the low-temperature AFM-b state as illustrated in Figure 5.16a. The results are reproduced in Figure 5.16b. The inset of Figure 5.16b shows the same calculation without spin-orbit coupling. It demonstrates that the electron and hole bands at Γ belong to minority- and majority-spin manifolds, respectively, which means that the hybridisation gap which creates the M-shaped top of the hole-like band below E_F is spin-orbit derived.

To calculate the band structure above T_S I use the experimental crystal structure measured at 50 K and the magnetic moment fixed along the crystal a axis, illustrated in Figure 5.16c, modelling the AFM-a state for the intermediate ($T_S < T < T_N$) temperature range. In this configuration, Figure 5.16d shows that the spin-orbit hybridisation of the hole-like and electron-like bands at the zone centre is strongly suppressed, and the bands cross through each other and through the Fermi level. This is in agreement with the creation of a large Fermi surface around the Γ point seen in the ARPES measurements in Figure 5.12. However, there is a potential discrepancy with the measured results in the binding energy of the electron-like band minimum at Γ. The calculations predict an electron pocket reaching well below the Fermi level, for which there is no evidence in the measured ARPES data in Figures 5.12 and 5.13. That said, we cannot exclude the possibility of a shallow electron-like band existing very close to the Fermi level above T_S, especially given the large linewidths and the Fermi broadening effects at high temperatures. As mentioned before, the Luttinger count and charge compensation would indeed suggest that might be the case. Another contributing factor lies in the choice of the exchange-correlation functional for the DFT calculation, and is discussed further below. Either way, there is sufficient evidence to indicate that this band hybridisation is
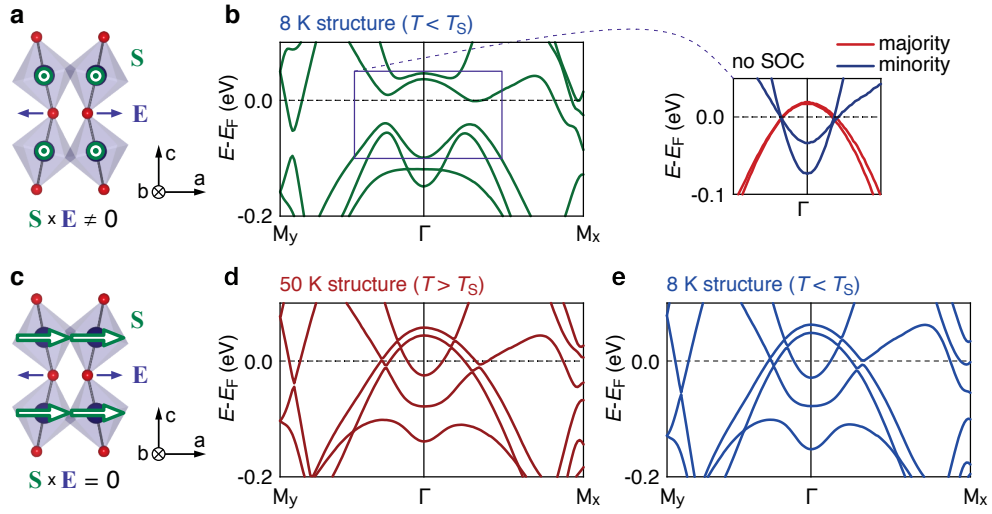
Figure 5.16: **Spin-orbit hybridisation of bands at T_S. a** Schematic of a single bilayer below T_S. Arrows indicate the spin orientation on Ru (green, **S**), and the direction of the local symmetry-breaking potential induced at bilayer sites by the X_3^- octahedral tilt mode (purple, **E**). **b** The corresponding DFT band structure calculations along the $M_y - \Gamma - M_x$ path in the Brillouin zone: using the 8 K experimental structure and the magnetic moment oriented along the b-axis. The inset shows the same calculation, but without SOC, and with colour indicating spin direction. **c** Schematic of the bilayer structure above T_S. **d** The DFT calculation for the $T_S < T < T_N$ phase - using the 50 K experimental structure and the magnetic moment oriented along the a-axis. **e** A DFT calculation using the 8 K experimental structure, but with the magnetic moment oriented along the a-axis.

not present above T_S, whether the electron band minimum is occupied or is indeed just above the Fermi level.

We have seen that two other aspects of the transition occur concurrently with the change in the Fermi surface: the isostructural change in unit cell volume, and the reorientation of the magnetic moment within the ab plane. Seeing how the electronic structure shows no appreciable change at the Nèel ordering temperature (Figure 5.12a), one might expect that the band hybridisation at T_S is dictated by the structural aspect of the transition described in Figure 5.3. For example, it could be thought to result from a change in relative energies of relevant bands due to a distortion in the octahedra. In order to test this, I have performed a calculation using the experimental crystal structure measured at 8 K, i.e. the low-temperature structure, but with the magnetic moment fixed along the crystal a axis, as in the intermediate-temperature AFM-a magnetic phase. The resulting

band structure shows no hybridisation between the bands at Γ, indicating that it is in fact the direction of the magnetic moment which determines whether the gap will form.

In order to better understand what effect the orientation of the magnetic moment has on the development of band hybridisation at the zone centre, I performed a series of DFT calculations with different magnetic moment orientations. I used the same experimental structure (8 K) as a basis and varied the spin direction in 15° increments in the *ab*, *bc*, and *ac* planes. The results, presented in Figure 5.17a–d, reveal that the spin-orbit hybridisation gap between the electron- and hole-like bands crossing at the Brillouin zone centre, Δ, is in fact only closed when the magnetic moment is orientated along the *a* axis. It gradually opens as $\mathbf{S}$ moves away from the *a* axis in either the *ab* or the *ac* plane, and stays relatively constant at any angle in the *bc* plane.

Because of the small numerical problems in my calculations mentioned before, I was concerned about the reliability of precisely extracting small gap values, and so I asked our DFT collaborator to reproduce the calculations on a denser $\mathbf{k}$-mesh, shown in Figure 5.17e. They show the same qualitative behaviour, but a smoother evolution of the gap value with the angle. Furthermore, the functional dependence of the gap opening in the *ab* and *ac* planes can be more reliably shown to be consistent with $\sin^2(\theta)$, where θ is measured from the *a* axis, as illustrated by the fitted curves in Figure 5.17e.

This functional dependence of the gap size on the angle of the spin moment from the *a* axis points to the relevant term in the Hamiltonian which mediates the band hybridisation having an $\mathbf{S} \times \mathbf{a}$ form. This would be proportional to $\sin(\theta)$, making the gap $\Delta \propto \sin^2(\theta)$, as observed in the experiment. Knowing that this gap comes from spin-orbit coupling, two questions present themselves: which type of spin-orbit coupling has this functional form, and what makes the *a* direction special for that spin-orbit coupling?

In itinerant-electron systems, it is the Rashba spin-orbit coupling term that carries this form, as described in Section 2.2. It is only present in a polar environment and is proportional to the cross product of the electronic spin and the effective electric field representing the local symmetry breaking potential, $\mathbf{S} \times \mathbf{E}_{\text{eff}}$. This implies that inversion symmetry should be broken on the Ru site with a polar axis along the *a* direction, so that
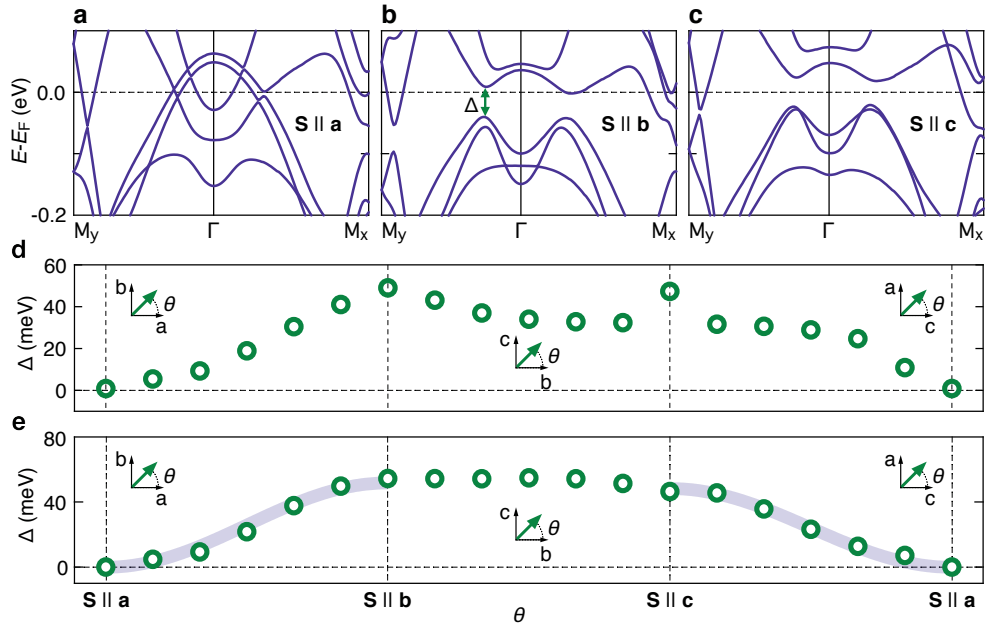
Figure 5.17: **Dependence of the gap on the orientation of the magnetic moment. a,b,c** The three band structures are calculated for the 8 K experimental crystal structure, but the magnetic moment oriented along the three principal crystal axes: **a** a, **b** b and **c** c. **d,e** Calculations performed by varying the direction of the magnetic moment in 15° increments in the ab, bc, and ac planes: **d** my results, and **e** Dr. Helge Rosner's results on a dense **k**-mesh. The $\sin^2$ curve is fit to the data in **e** for the magnetic moment rotating away from the a crystal axis in the ab or ac plane.

$\mathbf{E}_{\text{eff}} \parallel \mathbf{a}$. In fact, the local inversion symmetry breaking caused by the octahedral tilt mode, X_3^-, described in Section 5.1, provides precisely such an environment. It establishes local polar distortions of the lattice at the octahedral bilayer sites, enabling the Rashba-type spin-orbit coupling for electrons at those sites. When the spins of the electrons are parallel to the local polar distortion, i.e. at temperatures above T_S, the Rashba-type term is vanishing and no hybridisation can occur, as depicted in Figure 5.16c. At low temperatures, however, the magnetic moment reorients to the b direction, perpendicular to the local polar distortion, giving a finite Rashba term (Figure 5.16a) and a consequent gap opening at the Fermi level. One might ask why the same scenario does not work for the global polar distortion of $Ca_3Ru_2O_7$ (Figure 5.2c), given by the Γ_5^- mode, which provides an effective symmetry breaking field along the b axis. That structural distortion affects primarily the Ca atoms. Since the states at the Fermi level show minimal Ca character in Figure 5.7a, those electrons do very little hopping
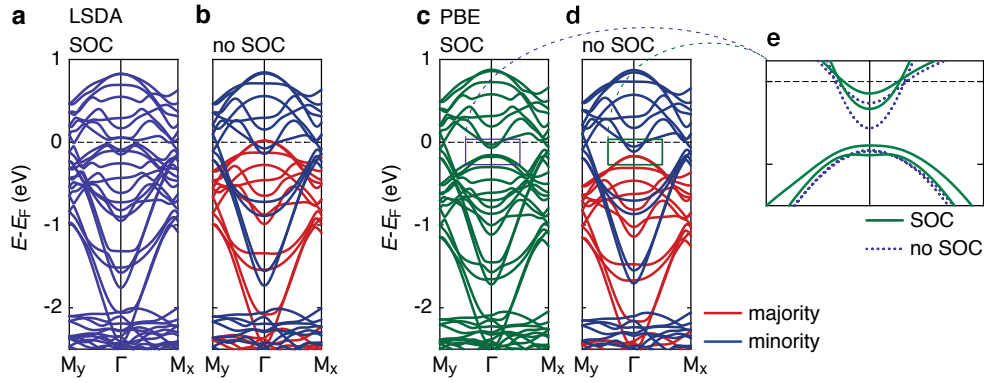
Figure 5.18: **Impact of different exchange-correlation functionals on the DFT band structure.** DFT calculated band structures along the M_y–Γ–M_x path using LSDA (**a,b**) and PBE (**c,d**) functionals, with (**a,c**) and without (**b,d**) including spin-orbit coupling. **e** A closer look at the relevant bands at Γ near the Fermi level for the PBE calculations shows that the bands hybridise with SOC, even without a direct band overlap. All the results shown here are from the calculations of Dr. Helge Rosner.

over Ca sites, and therefore do not experience the effects of the global polar distortion via the asymmetry of the hopping parameters.

There remains one problem with the comparison of our DFT calculations with the measured ARPES dispersions that I should address. As I have already mentioned above, the calculations for **S** ∥ **a** feature a relatively large band overlap of the electron- and hole-like bands at Γ (Figure 5.16d,e), with the bottom of the electron-like band reaching well below the Fermi level. This is supported by the Luttinger theorem [125, 126], and the expectation of 4 occupied electrons in the t_{2g} manifold of Ru^{4+} ions (Figure 5.4a), as described above. However, it is somewhat in contrast with the experimental situation where we do not see any evidence of a band being present at the Brillouin zone centre (Figure 5.12a). We can investigate the possible cause for the lack of a prominent electron pocket at Γ further by performing our calculations using a different exchange-correlation functional.

Figure 5.18 demonstrates differences in the calculated band structure using LSDA and PBE functionals, with and without spin-orbit coupling. The calculations are done for the low-temperature phase in order to show the effect on the hybridisation. As is commonly observed for the GGA-type functionals, our PBE calculations exhibit a more pronounced exchange splitting of the majority- and minority-spin bands as opposed to the LDA ones. This causes the bands, which cross near the Fermi level at Γ in

the LSDA calculations, to separate fully in energy when using the PBE functional, even when neglecting SOC. However, the bands still remain close enough in energy that they can hybridise via spin-orbit coupling, which is evident in the closer view in Figure 5.18e. The same physical phenomenon is therefore predicted by the PBE calculations as by the LSDA ones, but with the possibility of observing just the hole-like band in the unhybridised state, given an appropriate shift of the Fermi level in the calculation. We expect that the physical reality lies somewhere in between the pictures generated by the two different functionals. There is most likely a finite, but shallow band overlap occurring when there is no hybridisation. When hybridisation is switched on, the level repulsion induced by it pushes the M-shaped band top below E_{F}.

5.8   Electronically driven spin-reorientation transition

With the insight obtained above into the interplay of the magnetic moment orientation and the electronic structure at the Fermi level, we can reexamine our understanding of the T_{S} phase transitions in $Ca_3Ru_2O_7$. At temperatures above the transition, magnetocrystalline anisotropy prefers the magnetic moment to be oriented along the a crystal axis. As this aligns with the local polar axis at the bilayer sites, the Rashba term in the Hamiltonian cannot hybridise the electron- and hole-like bands overlapping at the Brillouin zone centre, resulting in the presence of the large Fermi surface. The thermal occupation of electronic states above the Fermi level is large enough that the energy gain from a spin-orbit gap Δ which would open if the spins were along b is outweighed by the magnetocrystalline costs of re-orienting the spins. The easy magnetic axis at this temperature is therefore set by magnetocrystalline anisotropy terms in the free energy.

Lowering the temperature further, the width of the Fermi function narrows. This causes smaller occupation of the states above the Fermi level, as schematically shown in Figure 5.19b, and the electronic energy gain from opening a gap at the Fermi level increases. At T_{S} it overcomes the magnetocrystalline anisotropy and the energy cost of the unit cell volume increase dictated by magnetoelastic coupling. At this point the lowest energy state becomes the one where the Rashba-type Hamiltonian hybridises the states at the Fermi level and gaps out the large Fermi surface by rotating the ordered magnetic moments into the b direction. As a result, only the small Fermi pockets remain, accompanied by an increase in the quasiparticle life-
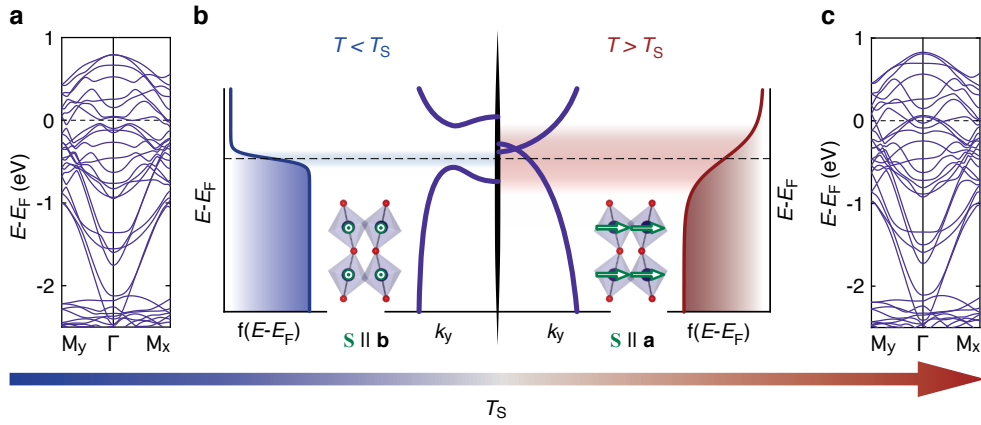
Figure 5.19: **Model of the T_S phase transition. a,c** Band structures calculated by DFT for the $Ca_3Ru_2O_7$: **a** above, and **c** below T_S. **b** Diagrammatic illustration of the thermal occupation of the bands above and below T_S demonstrating the source of the electronic energy gain at the transition.

times. This turns the material into a low-carrier density semimetal with multiple carrier types, and accounts for the changes at T_S observed in transport properties. The magnetic order in the low-temperature phase becomes AFM-*b*. As a result, the system must pay the energy cost of the magnetoelastic coupling term, changing the lattice parameters and increasing the unit cell volume.

5.9   Conclusion

In this Chapter, I have provided novel insights into the electronic structure and phase transitions of $Ca_3Ru_2O_7$, a strongly interacting system hosting intertwined electronic, magnetic and lattice degrees of freedom. Our determination of the low-temperature electronic structure provides an improvement in the understanding of the structure of the Fermi surface. The large anisotropy of the boomerang shape of the hole Fermi pockets, and the involvement of all three t_{2g} orbitals at the Fermi level, point to the Ru $4d_{xy}$ orbital not being completely occupied as is the case in the single-layer compound, Ca_2RuO_4.

We have observed a dramatic change in the low-energy electronic structure upon crossing the known isostructural and spin-reorientation phase transition at $T_S = 48$ K. The sudden increase in the number of carriers above T_S, with the concurrent decrease in the quasiparticle lifetimes, provide

a good explanation for the complex temperature dependence of resistivity and the Hall coefficient in this system.

The ARPES measurements reveal that the band structure transition at T_S, which mediates the above mentioned changes in the physical properties of $Ca_3Ru_2O_7$, comes from a band hybridisation which gaps a large Fermi surface at low temperatures. Our *ab initio* calculations point to that hybridisation being the result of a bulk Rashba-type spin-orbit coupling term enabled by the octahedral tilt distortion and activated by the magnetic moment aligning perpendicular to the local symmetry breaking potential at the Ru sites. This suggests the mechanism for the phase transition in which the electronic energy gain from opening a gap increases with decreasing temperature, and at T_S outweighs the magnetocrystalline costs to reorienting the spins, necessary for the hybridisation to occur.

This mechanism reveals a new source of magnetic anisotropy in metallic materials, whereby the easy axis of the material can be altered by spin-orientation dependent hybridisations at the Fermi level. It is plausible to imagine this mechanism becoming relevant in various materials where inversion symmetry is broken, whether in the bulk of the crystal, via heterostructuring approaches, or at surfaces and interfaces, allowing for a Rashba-type spin-orbit coupling term to develop.

One could also look to control the electronic transport properties via external manipulation of the magnetic moment orientation. One way to do this would be by applying an external magnetic field to reorient the spins. However, if there is a considerable magnetoelastic component to the transition as in $Ca_3Ru_2O_7$, this should also be achievable with application of pressure or strain, using the magnetoelastic energy to drive the transition, as indicated by early magnetostriction experiments [250]. If a material could be designed with these properties, but where the affected pocket comprises the whole Fermi surface, this would constitute a novel type of a metal-insulator transition in correlated magnets.

6 | Conclusion

During my PhD I employed experimental, i.e. spin- and angle-resolved photoemission spectroscopy, and theoretical, i.e. density-functional theory and tight-binding modelling, approaches to study the electronic structure of materials. My focus was on materials in which the combination of strong spin-orbit coupling and particular crystal symmetries results in novel features of the electronic structure. This thesis details my results on two such quantum materials in strongly differing regimes of the electronic interaction strength: NbGeSb, which is a weakly interacting system, and $Ca_3Ru_2O_7$, which hosts strong electronic interactions. For both materials I first established and described the main properties of their electronic structure near the Fermi level, before focusing on a particular feature where specific interplays of crystal symmetries and spin-orbit coupling lead to novel phenomena in the electronic sector.

Spin-orbit coupling has been shown to play a crucial role in developing topological features of the band structure in non-interacting electron systems. In Chapter 4, NbGeSb, a member of a bulk Dirac nodal line semimetal family, was found to host protected band crossings of topologically trivial spin-split surface states appearing along a high-symmetry line of the surface projected Brillouin zone. The surface states in question are created by the breaking of the bulk nonsymmorphic symmetry at the surface of the crystal, where they develop orbital angular momentum, and significant spin-splitting as a result of a Rashba-type mechanism. Two such spin-split pairs of surface states are inverted along the Brillouin zone boundary, which coincides with a mirror plane of the system. The mirror symmetry, along with time-reversal and global fourfold rotational symmetries, strongly constrains the allowed projections, as well as mixings, of the spin and orbital angular momenta of the inverted bands. This results in a quartet of band crossings, two of which remain protected while two develop highly asymmetric gaps. Such crossing structure was shown to be understandable in terms of a two-level model in both angular momentum sectors, causing the crossing of bands with the same spin to be protected, while the crossings of bands with opposite spin develop a pronounced hybridisation asymme-

try. Our tight-binding model shows non-trivial winding of orbital angular momentum which forms a chiral pseudospin, and we found the low-energy description of the band structure around the crossing is topologically equivalent to two dimensional analogues of Weyl points.

In contrast to NbGeSb, $Ca_3Ru_2O_7$ is a strongly interacting system, and one where crystal, magnetic and electronic structures all significantly influence each other. The interdependence of all these degrees of freedom is evident in a phase transition where pronounced change in the electronic structure at the Fermi level occurs simultaneously with an isostructural change in the unit cell and a spin reorientation of the established antiferromagnetic order. I have demonstrated in Chapter 5 how this phase transition arises due to an electronic energy gain from the opening a spin-orbit gap in the electronic structure at the Fermi level. The hybridisation was shown to come from a Rashba-type spin-orbit term which develops due to an antipolar distortion present in the crystal structure, and is unlocked by the reorientation of the antiferromagnetic order perpendicular to the polar axis of that distortion. Via this mechanism, spin-orbit coupling effectively imposes a novel, "magneto-electronic" anisotropy dictating the details of the magnetic structure.

The underlying feature is that the allowed orientations of angular momenta in the presence of spin-orbit coupling are dictated by the details of the crystal symmetry, as well as the allowed spin-orbit band hybridisations in the presence of magnetism. In NbGeSb this interplay leads to the emergence of two-dimensional analogues of Weyl points and creates winding textures of spin and orbital angular momenta in the surface electronic structure around them. In $Ca_3Ru_2O_7$ it causes the spin-orbit coupling bootstrapped with strong electron interactions to manifest in a phase transition where the preexisting magnetic moments reorient into a direction set by the crystal symmetry. These two materials represent very disparate electronic systems, yet I have demonstrated how the novel phenomena that I describe in them originate from the same underlying idea of the interplay between the spin-orbit coupling and the crystal symmetries. This interplay can be seen as ubiquitous in spin-orbit coupled quantum materials, and an important source of novel phenomena in their electronic structure.

| Bibliography

[1] Keimer, B. & Moore, J. E. The physics of quantum materials. *Nature Physics* **13**, 1045–1055 (2017).

[2] Basov, D. N., Averitt, R. D. & Hsieh, D. Towards properties on demand in quantum materials. *Nature Materials* **16**, 1077–1088 (2017).

[3] Samarth, N. Quantum materials discovery from a synthesis perspective. *Nature Materials* **16**, 1068–1076 (2017).

[4] Tokura, Y., Kawasaki, M. & Nagaosa, N. Emergent functions of quantum materials. *Nature Physics* **13**, 1056–1068 (2017).

[5] Han, W., Otani, Y. & Maekawa, S. Quantum materials for spin and charge conversion. *npj Quantum Materials* **3**, 1–16 (2018).

[6] Shen, K. M. & Davis, J. C. S. Cuprate high-T_{C} superconductors. *Materials Today* **11**, 14–21 (2008).

[7] Chubukov, A. & Hirschfeld, P. J. Iron-based superconductors, seven years later. *Physics Today* **68**, 46 (2015).

[8] Hosono, H., Yamamoto, A., Hiramatsu, H. & Ma, Y. Recent advances in iron-based superconductors toward applications. *Materials Today* **21**, 278–302 (2018).

[9] Hasan, M. Z. & Kane, C. L. Colloquium: Topological insulators. *Reviews of Modern Physics* **82**, 3045–3067 (2010).

[10] Qi, X.-L. & Zhang, S.-C. Topological insulators and superconductors. *Reviews of Modern Physics* **83**, 1057–1110 (2011).

[11] Armitage, N. P., Mele, E. J. & Vishwanath, A. Weyl and Dirac semimetals in three-dimensional solids. *Reviews of Modern Physics* **90**, 015001 (2018).

[12] Turner, A. M. & Vishwanath, A. Beyond band insulators: Topology of semimetals and interacting phases. In *Topological Insulators* (Elsevier, 2013).

[13] Sandratskii, L. M. Noncollinear magnetism in itinerant-electron systems: Theory and applications. *Advances in Physics* **47**, 91–160 (1998).

[14] Kimura, T. Spiral magnets as magnetoelectrics. *Annual Review of Materials Research* **37**, 387–413 (2007).

[15] Fert, A., Reyren, N. & Cros, V. Magnetic skyrmions: Advances in physics and potential applications. *Nature Reviews Materials* **2**, 1–15 (2017).

[16] Garst, M., Waizner, J. & Grundler, D. Collective spin excitations of helices and magnetic skyrmions: Review and perspectives of magnonics in non-centrosymmetric magnets. *Journal of Physics D: Applied Physics* **50**, 293002 (2017).

[17] Huang, B. *et al.* Layer-dependent ferromagnetism in a van der Waals crystal down to the monolayer limit. *Nature* **546**, 270–273 (2017).

[18] Wang, Z. *et al.* Electric-field control of magnetism in a few-layered van der Waals ferromagnetic semiconductor. *Nature* **13**, 554–559 (2018).

[19] Li, H., Ruan, S. & Zeng, Y.-J. Intrinsic van der Waals magnetic materials from bulk to the 2D limit: New frontiers of spintronics. *Advanced Materials* **31**, 1900065 (2019).

[20] Savary, L. & Balents, L. Quantum spin liquids: a review. *Reports on Progress in Physics* **80**, 016502 (2016).

[21] Gingras, M. J. P. & McClarty, P. A. Quantum spin ice: a search for gapless quantum spin liquids in pyrochlore magnets. *Reports on Progress in Physics* **77**, 056501 (2014).

[22] Bader, S. D. & Parkin, S. S. P. Spintronics. *Annual Review of Condensed Matter Physics* **1**, 71–88 (2010).

[23] Hirohata, A. *et al.* Review on spintronics: Principles and device applications. *Journal of Magnetism and Magnetic Materials* 166711 (2020).

[24] Schaibley, J. R. *et al.* Valleytronics in 2D materials. *Nature Reviews Materials* **1**, 1–15 (2016).

[25] Carr, S. *et al.* Twistronics: Manipulating the electronic properties of two-dimensional layered structures through their twist angle. *Physical Review B* **95**, 075420 (2017).

[26] Sarma, S. D., Freedman, M. & Nayak, C. Majorana zero modes and topological quantum computation. *npj Quantum Information* **1**, 1–13 (2015).

[27] Witczak-Krempa, W., Chen, G., Kim, Y. B. & Balents, L. Correlated quantum phenomena in the strong spin-orbit regime. *Annual Review of Condensed Matter Physics* **5**, 57–82 (2014).

[28] Rau, J. G., Lee, E. K.-H. & Kee, H.-Y. Spin-orbit physics giving rise to novel phases in correlated systems: Iridates and related materials. *Annual Review of Condensed Matter Physics* **7**, 195–221 (2016).

[29] Bercioux, D. & Lucignano, P. Quantum transport in Rashba spin–orbit materials: a review. *Reports on Progress in Physics* **78**, 106001 (2015).

[30] Krasovskii, E. E. Spin–orbit coupling at surfaces and 2D materials. *Journal of Physics: Condensed Matter* **27**, 493001 (2015).

[31] Manchon, A., Koo, H. C., Nitta, J., Frolov, S. M. & Duine, R. A. New perspectives for Rashba spin–orbit coupling. *Nature Materials* **14**, 871–882 (2015).

[32] Santini, P. *et al.* Multipolar interactions in f-electron systems: The paradigm of actinide dioxides. *Reviews of Modern Physics* **81**, 807–863 (2009).

[33] Rashba, E. I. & Sheka, V. I. Symmetry of energy bands in crystals of wurtzite type: II. Symmetry of bands including spin-orbit interaction. *Fizika Tverdogo Tela* **2**, 162–176 (1959).

[34] Dresselhaus, G. Spin-orbit coupling effects in zinc blende structures. *Physical Review* **100**, 580–586 (1955).

[35] Bychkov, Y. & Rashba, E. I. Properties of a 2D electron gas with lifted spectral degeneracy. *JETP Letters* **39** (1984).

[36] Zhang, X., Liu, Q., Luo, J.-W., Freeman, A. J. & Zunger, A. Hidden spin polarization in inversion-symmetric bulk crystals. *Nature Physics* **10**, 387–393 (2014).

[37] Dzyaloshinsky, I. A thermodynamic theory of "weak" ferromagnetism of antiferromagnetics. *Journal of Physics and Chemistry of Solids* **4**, 241–255 (1958).

[38] Moriya, T. Anisotropic superexchange interaction and weak ferromagnetism. *Physical Review* **120**, 91–98 (1960).

[39] Imada, M., Fujimori, A. & Tokura, Y. Metal-insulator transitions. *Reviews of Modern Physics* **70**, 225 (1998).

[40] Georges, A., de' Medici, L. & Mravlje, J. Strong correlations from Hund's coupling. *Annual Review of Condensed Matter Physics* **4**, 137–178 (2013).

[41] Mott, N. F. Metal-insulator transition. *Reviews of Modern Physics* **40**, 677–683 (1968).

[42] Pesin, D. & Balents, L. Mott physics and band topology in materials with strong spin–orbit interaction. *Nature Physics* **6**, 376–381 (2010).

[43] Schaffer, R., Lee, E. K.-H., Yang, B.-J. & Kim, Y. B. Recent progress on correlated electron systems with strong spin–orbit coupling. *Reports on Progress in Physics* **79**, 094504 (2016).

[44] Damascelli, A., Hussain, Z. & Shen, Z.-X. Angle-resolved photoemission studies of the cuprate superconductors. *Reviews of Modern Physics* **75**, 473–541 (2003).

[45] Damascelli, A. Probing the electronic structure of complex systems by ARPES. *Physica Scripta* **2004**, 61 (2004).

[46] Lu, D. H. *et al.* Angle-resolved photoemission studies of quantum materials. *Annual Review of Condensed Matter Physics* **3**, 129–167 (2012).

[47] Gedik, N. & Vishik, I. Photoemission of quantum materials. *Nature Physics* **13**, 1029–1033 (2017).

[48] Ashcroft, N. W. & Mermin, N. D. *Solid State Physics* (BROOKS/COLE, 1976).

[49] Singleton, J. *Band Theory and Electronic Properties of Solids* (Oxford University Press, 2001).

[50] Simon, S. H. *The Oxford Solid State Basics* (Oxford University Press, 2013).

[51] Hoffmann, R. How chemistry and physics meet in the solid state. *Angewandte Chemie International Edition in English* **26**, 846–878 (1987).

[52] Goringe, C. M., Bowler, D. R. & Hernández, E. Tight-binding modelling of materials. *Reports on Progress in Physics* **60**, 1447–1512 (1997).

[53] Hoffmann, R. *Solids and Surfaces: A Chemist's View of Bonding in Extended Structures* (Wiley-VCH, 1989).

[54] Slater, J. C. & Koster, G. F. Simplified LCAO method for the periodic potential problem. *Physical Review* **94**, 1498–1524 (1954).

[55] Kuneš, J. Wannier functions and construction of model Hamiltonians. In *The LDA+DMFT approach to strongly correlated matter*, Jülich Autumn School on Correlated Electrons (2011).

[56] Mackenzie, A. P. The properties of ultrapure delafossite metals. *Reports on Progress in Physics* **80**, 032501 (2017).

[57] Kugel', K. I. & Khomskii, D. I. The Jahn-Teller effect and magnetism: transition metal compounds. *Soviet Physics Uspekhi* **25**, 231 (1982).

[58] Griffiths, D. J. & Schroeter, D. F. *Introduction to Quantum Mechanics* (Cambridge University Press, 2018).

[59] Sakurai, J. J. & Napolitano, J. *Modern quantum mechanics* (Addison-Wesley, 2011), 2 edn.

[60] Herman, F. & Skillman, S. *Atomic Structure Calculations* (Prentice-Hall, 1963).

[61] Watson, M. D. *et al.* Direct observation of the energy gain underpinning ferromagnetic superexchange in the electronic structure of CrGeTe$_3$. *arXiv:1912.11314 [cond-mat]* (2019).

[62] Elliott, R. J. Spin-orbit coupling in band theory - character tables for some "double" space groups. *Physical Review* **96**, 280–287 (1954).

[63] Petersen, L. & Hedegård, P. A simple tight-binding model of spin–orbit splitting of *sp*-derived surface states. *Surface Science* **459**, 49–56 (2000).

[64] Hopster, H. *et al.* Temperature dependence of the exchange splitting in Ni studied by spin-polarized photoemission. *Physical Review Letters* **51**, 829–832 (1983).

[65] LaShell, S., McDougall, B. A. & Jensen, E. Spin splitting of an Au(111) surface state band observed with angle resolved photoelectron spectroscopy. *Physical Review Letters* **77**, 3419–3422 (1996).

[66] Hoesch, M. *et al.* Spin structure of the Shockley surface state on Au(111). *Physical Review B* **69**, 241401 (2004).

[67] Tamai, A. *et al.* Spin-orbit splitting of the Shockley surface state on Cu(111). *Physical Review B* **87**, 075113 (2013).

[68] Bihlmayer, G., Rader, O. & Winkler, R. Focus on the Rashba effect. *New Journal of Physics* **17**, 050202 (2015).

[69] Varignon, J., Santamaria, J. & Bibes, M. Electrically switchable and tunable Rashba-type spin splitting in covalent perovskite oxides. *Physical Review Letters* **122**, 116401 (2019).

[70] Pfeffer, P. & Zawadzki, W. Spin splitting of conduction subbands in III-V heterostructures due to inversion asymmetry. *Physical Review B* **59**, R5312–R5315 (1999).

[71] Konschuh, S., Gmitra, M. & Fabian, J. Tight-binding theory of the spin-orbit coupling in graphene. *Physical Review B* **82**, 245412 (2010).

[72] Ast, C. R. & Gierz, I. *sp*-band tight-binding model for the Bychkov-Rashba effect in a two-dimensional electron system including nearest-neighbor contributions from an electric field. *Physical Review B* **86**, 085105 (2012).

[73] Park, S. R. & Kim, C. Microscopic mechanism for the Rashba spin-band splitting: Perspective from formation of local orbital angular momentum. *Journal of Electron Spectroscopy and Related Phenomena* **201**, 6–17 (2015).

[74] Riley, J. M. *et al.* Direct observation of spin-polarized bulk bands in an inversion-symmetric semiconductor. *Nature Physics* **10**, 835–839 (2014).

[75] Razzoli, E. *et al.* Selective probing of hidden spin-polarized states in inversion-symmetric bulk MoS_2. *Physical Review Letters* **118**, 086402 (2017).

[76] Tinkham, M. *Group Theory and Quantum Mechanics* (McGraw-Hill, 1964).

[77] Dresselhaus, M. S., Dresselhaus, G. & Jorio, A. *Group Theory - Application to the Physics of Condensed Matter* (Springer, 2008).

[78] Schofield, A. J. Non-Fermi liquids. *Contemporary Physics* **40**, 95–115 (1999).

[79] Nozières, P. & Pines, D. *Theory Of Quantum Liquids* (Avalon Publishing, 1999).

[80] Hooley, C. A. Modern topics in condensed matter physics - lecture notes (2018).

[81] Landau, L. D. The theory of a Fermi liquid. *Soviet Physics JETP* **3**, 920 (1957).

[82] Landau, L. D. Oscillations in a Fermi liquid. *Soviet Physics JETP* **5**, 101 (1957).

[83] Landau, L. D. On the theory of the Fermi liquid. *Soviet Physics JETP* **8**, 70 (1959).

[84] Mahan, G. D. *Many-Particle Physics* (Springer, 2000), 3 edn.

[85] Hüfner, S. *Photoelectron Spectroscopy - Principles and Applications* (Springer, 2003), 3 edn.

[86] Hüfner, S. (ed.) *Very High Resolution Photoelectron Spectroscopy* (Springer, 2007).

[87] Kittel, C. *Introduction to solid state physics* (Wiley, 2005).

[88] Hertz, H. Über einen Einfluss des ultravioletten Lichtes auf die electrische Entladung. *Annalen der Physik* **267**, 983–1000 (1887).

[89] Einstein, A. On heuristic point of view about the creation and conversion of light. *Ann. Physik* **17** (1905).

[90] Minár, J. Theoretical description of ARPES: The one-step model. In *DMFT at 25: Infinite Dimensions*, Jülich Autumn School on Correlated Electrons (2014).

[91] Mahan, G. D. Theory of photoemission in simple metals. *Physical Review B* **2**, 4334–4350 (1970).

[92] Berglund, C. N. & Spicer, W. E. Photoemission studies of copper and silver: Theory. *Physical Review* **136**, A1030–A1044 (1964).

[93] Wang, X.-P. *et al.* Orbital characters determined from Fermi surface intensity patterns using angle-resolved photoemission spectroscopy. *Physical Review B* **85**, 214518 (2012).

[94] Day, R. P., Zwartsenberg, B., Elfimov, I. S. & Damascelli, A. Computational framework chinook for angle-resolved photoemission spectroscopy. *npj Quantum Materials* **4**, 54 (2019).

[95] Park, J.-H., Kim, C. H., Rhim, J.-W. & Han, J. H. Orbital Rashba effect and its detection by circular dichroism angle-resolved photoemission spectroscopy. *Physical Review B* **85**, 195401 (2012).

[96] Cao, Y. *et al.* Mapping the orbital wavefunction of the surface states in three-dimensional topological insulators. *Nature Physics* **9**, 499–504 (2013).

[97] Bawden, L. *et al.* Hierarchical spin-orbital polarization of a giant Rashba system. *Science Advances* **1**, e1500495 (2015).

[98] Seah, M. P. & Dench, W. A. Quantitative electron spectroscopy of surfaces: A standard data base for electron inelastic mean free paths in solids. *Surface and Interface Analysis* **1**, 2–11 (1979).

[99] Strocov, V. N. Intrinsic accuracy in 3-dimensional photoemission band mapping. *Journal of Electron Spectroscopy and Related Phenomena* **130**, 65–78 (2003).

[100] Shirley, D. A. High-resolution x-ray photoemission spectrum of the valence bands of gold. *Physical Review B* **5**, 4709–4714 (1972).

[101] Proctor, A. & Sherwood, P. M. A. Data analysis techniques in x-ray photoelectron spectroscopy. *Analytical Chemistry* **54**, 13–19 (1982).

[102] Sherwood, P. M. A. Curve fitting in surface analysis and the effect of background inclusion in the fitting process. *Journal of Vacuum Science & Technology A: Vacuum, Surfaces, and Films* **14**, 1424–1432 (1996).

[103] Tougaard, S. Universality classes of inelastic electron scattering cross-sections. *Surface and Interface Analysis* **25**, 137–154 (1997).

[104] Ishida, Y. & Shin, S. Functions to map photoelectron distributions in a variety of setups in angle-resolved photoemission spectroscopy. *Review of Scientific Instruments* **89**, 043903 (2018).

[105] Smith, N. V., Thiry, P. & Petroff, Y. Photoemission linewidths and quasiparticle lifetimes. *Physical Review B* **47**, 15476–15481 (1993).

[106] Osterwalder, J. Spin-polarized photoemission. In Beaurepaire, E., Bulou, H., Scheurer, F. & Kappler, J.-P. (eds.) *Magnetism: A Synchrotron Radiation Approach*, 95–120 (Springer, 2006).

[107] Dil, J. H. Spin and angle resolved photoemission on non-magnetic low-dimensional systems. *Journal of Physics: Condensed Matter* **21**, 403001 (2009).

[108] Okuda, T. *et al.* Efficient spin resolved spectroscopy observation machine at Hiroshima Synchrotron Radiation Center. *Review of Scientific Instruments* **82**, 103302 (2011).

[109] Okuda, T., Miyamoto, K., Kimura, A., Namatame, H. & Taniguchi, M. A double VLEED spin detector for high-resolution three dimensional spin vectorial analysis of anisotropic Rashba spin splitting. *Journal of Electron Spectroscopy and Related Phenomena* **201**, 23–29 (2015).

[110] Bigi, C. *et al.* Very efficient spin polarization analysis (VESPA): new exchange scattering-based setup for spin-resolved ARPES at APE-NFFA beamline at Elettra. *Journal of Synchrotron Radiation* **24**, 750–756 (2017).

[111] Okuda, T. *et al.* A new spin-polarized photoemission spectrometer with very high efficiency and energy resolution. *Review of Scientific Instruments* **79**, 123117 (2008).

[112] Sherman, N. Coulomb scattering of relativistic electrons by point nuclei. *Physical Review* **103**, 1601–1607 (1956).

[113] Hoesch, M. *et al.* Spin-polarized Fermi surface mapping. *Journal of Electron Spectroscopy and Related Phenomena* **124**, 263–279 (2002).

[114] Iwasawa, H. *et al.* Development of laser-based scanning μ-ARPES system with ultimate energy and momentum resolutions. *Ultramicroscopy* **182**, 85–91 (2017).

[115] He, Y. *et al.* High resolution angle resolved photoemission with table-top 11 eV laser. *Review of Scientific Instruments* **87**, 011301 (2016).

[116] Tamai, A. *et al.* High-resolution photoemission on Sr_2RuO_4 reveals correlation-enhanced effective spin-orbit coupling and dominantly local self-energies. *Physical Review X* **9**, 021048 (2019).

[117] Willmott, P. *An Introduction to Synchrotron Radiation: Techniques and Applications* (John Wiley & Sons, 2011).

[118] Hoesch, M. *et al.* A facility for the analysis of the electronic structures of solids and their surfaces by synchrotron radiation photoelectron spectroscopy. *Review of Scientific Instruments* **88**, 013106 (2017).

[119] BLOCH beamline – MAX IV synchrotron. URL `https://www.maxiv.lu.se/accelerators-beamlines/beamlines/bloch/bloch-beamline-optics/`.

[120] CASSIOPEE beamline - SOLEIL synchrotron. URL `https://www.synchrotron-soleil.fr/en/beamlines/cassiopee`.

[121] SIS X09LA beamline - Swiss Light Source synchrotron. URL `https://www.psi.ch/en/sls/sis`.

[122] Panaccione, G. *et al.* Advanced photoelectric effect experiment beamline at Elettra: A surface science laboratory coupled with synchrotron radiation. *Review of Scientific Instruments* **80**, 043105 (2009).

[123] BL-9B beamline - Hiroshima Synchrotron Radiation Center. URL `http://www.hsrc.hiroshima-u.ac.jp/english/storagering_beamlines/beamlines.html`.

[124] Lüth, H. *Solid Surfaces, Interfaces and Thin Films* (Springer, 2010).

[125] Luttinger, J. M. & Ward, J. C. Ground-state energy of a many-fermion system. II. *Physical Review* **118**, 1417–1427 (1960).

[126] Luttinger, J. M. Fermi surface and some simple equilibrium properties of a system of interacting fermions. *Physical Review* **119**, 1153–1163 (1960).

[127] Capelle, K. A bird's-eye view of density-functional theory. *arXiv:cond-mat/0211443* (2006).

[128] Hohenberg, P. & Kohn, W. Inhomogeneous electron gas. *Physical Review* **136**, B864–B871 (1964).

[129] Kohn, W. & Sham, L. J. Self-consistent equations including exchange and correlation effects. *Physical Review* **140**, A1133–A1138 (1965).

[130] Slater, J. C. Wave functions in a periodic potential. *Physical Review* **51**, 846–851 (1937).

[131] Slater, J. C. Energy band calculations by the augmented plane wave method. In *Advances in Quantum Chemistry*, vol. 1, 35–58 (Elsevier, 1964).

[132] Perdew, J. P., Burke, K. & Ernzerhof, M. Generalized gradient approximation made simple. *Physical Review Letters* **77**, 3865–3868 (1996).

[133] Blaha, P., Schwarz, K., Sorantin, P. & Trickey, S. B. Full-potential, linearized augmented plane wave programs for crystalline systems. *Computer Physics Communications* **59**, 399–415 (1990).

[134] Blaha, P. *et al.* WIEN2k: An APW+lo program for calculating the properties of solids. *The Journal of Chemical Physics* **152**, 074101 (2020).

[135] Blaha, P. *et al.* *WIEN2k User's guide* (2019).

[136] Koepernik, K. & Eschrig, H. Full-potential nonorthogonal local-orbital minimum-basis band-structure scheme. *Physical Review B* **59**, 1743–1757 (1999).

[137] Kresse, G. & Furthmüller, J. Efficient iterative schemes for ab initio total-energy calculations using a plane-wave basis set. *Physical Review B* **54**, 11169–11186 (1996).

[138] Sholl, D. S. & Steckel, J. A. DFT calculations for surfaces of solids. In *Density Functional Theory: A Practical Introduction*, 83–112 (John Wiley & Sons, Ltd, 2009).

[139] Wilczek, F. Why are there analogies between condensed matter and particle theory? *Physics Today* **51**, 11–13 (1998).

[140] Vafek, O. & Vishwanath, A. Dirac fermions in solids: From high-T_C cuprates and graphene to topological insulators and Weyl semimetals. *Annual Review of Condensed Matter Physics* **5**, 83–112 (2014).

[141] Yan, B. & Felser, C. Topological materials: Weyl semimetals. *Annual Review of Condensed Matter Physics* **8**, 337–354 (2017).

[142] Dirac, P. A. M. The quantum theory of the electron. *Proceedings of the Royal Society of London. Series A* **117**, 610–624 (1928).

[143] Dirac, P. A. M. A theory of electrons and protons. *Proceedings of the Royal Society of London. Series A* **126**, 360–365 (1930).

[144] Weyl, H. Elektron und Gravitation. I. *Zeitschrift für Physik* **56**, 330–352 (1929).

[145] von Neuman, J. & Wigner, E. Über merkwürdige diskrete Eigenwerte. Über das Verhalten von Eigenwerten bei adiabatischen Prozessen. *Physikalische Zeitschrift* **30**, 467–470 (1929).

[146] Herring, C. Accidental degeneracy in the energy bands of crystals. *Physical Review* **52**, 365–373 (1937).

[147] Berry, M. V. Aspects of degeneracy. In Casati, G. (ed.) *Chaotic Behavior in Quantum Systems: Theory and Applications*, 123–140 (Springer, 1985).

[148] Liu, Z. K. *et al.* Discovery of a three-dimensional topological Dirac semimetal, Na_3Bi. *Science* **343**, 864–867 (2014).

[149] Wang, Z., Weng, H., Wu, Q., Dai, X. & Fang, Z. Three-dimensional Dirac semimetal and quantum transport in Cd_3As_2. *Physical Review B* **88**, 125427 (2013).

[150] Borisenko, S. *et al.* Experimental realization of a three-dimensional Dirac semimetal. *Physical Review Letters* **113**, 027603 (2014).

[151] Neupane, M. *et al.* Observation of a three-dimensional topological Dirac semimetal phase in high-mobility Cd_3As_2. *Nature Communications* **5**, ncomms4786 (2014).

[152] Fu, L., Kane, C. L. & Mele, E. J. Topological insulators in three dimensions. *Physical Review Letters* **98**, 106803 (2007).

[153] Fu, L. & Kane, C. L. Topological insulators with inversion symmetry. *Physical Review B* **76**, 045302 (2007).

[154] Witten, E. Three lectures on topological phases of matter. *La Rivista del Nuovo Cimento* **39**, 313–370 (2016).

[155] Kariyado, T. & Ogata, M. Three-dimensional Dirac electrons at the Fermi energy in cubic inverse perovskites: Ca_3PbO and its family. *Journal of the Physical Society of Japan* **80**, 083704 (2011).

[156] Kariyado, T. & Ogata, M. Low-energy effective Hamiltonian and the surface states of Ca_3PbO. *Journal of the Physical Society of Japan* **81**, 064701 (2012).

[157] Michel, L. & Zak, J. Connectivity of energy bands in crystals. *Physical Review B* **59**, 5998–6001 (1999).

[158] Yang, S.-Y. *et al.* Symmetry demanded topological nodal-line materials. *Advances in Physics: X* **3**, 1414631 (2018).

[159] Bradley, C. & Cracknell, A. *The Mathematical Theory of Symmetry in Solids: Representation Theory for Point Groups and Space Groups* (Oxford University Press, 2009).

[160] Tremel, W. & Hoffmann, R. Square nets of main-group elements in solid-state materials. *Journal of the American Chemical Society* **109**, 124–140 (1987).

[161] Young, S. M. & Kane, C. L. Dirac semimetals in two dimensions. *Physical Review Letters* **115**, 126803 (2015).

[162] von Schnering, H. G. Homoatomic bonding of main group elements. *Angewandte Chemie International Edition in English* **20**, 33–51 (1981).

[163] Atkins, P., Overton, T., Rourke, J., Weller, M. & Armstrong, F. *Shriver and Atkins' Inorganic Chemistry* (W. H. Freeman and Company, 2010).

[164] Haneveld, A. J. K. & Jellinek, F. Zirconium silicide and germanide chalcogenides preparation and crystal structures. *Recueil des Travaux Chimiques des Pays-Bas* **83**, 776–783 (1964).

[165] Johnson, V. & Jeitschko, W. PbFCl-type pnictides of niobium with silicon or germanium. *Journal of Solid State Chemistry* **6**, 306–309 (1973).

[166] Klemenz, S., Lei, S. & Schoop, L. M. Topological semimetals in square-net materials. *Annual Review of Materials Research* **49**, 185–206 (2019).

[167] Chen, C. *et al.* Dirac line nodes and effect of spin-orbit coupling in the nonsymmorphic critical semimetals MSiS (M=Hf,Zr). *Physical Review B* **95**, 125126 (2017).

[168] Su, C.-C. *et al.* Surface termination dependent quasiparticle scattering interference and magneto-transport study on ZrSiS. *New Journal of Physics* **20**, 103025 (2018).

[169] Schoop, L. M. *et al.* Dirac cone protected by non-symmorphic symmetry and three-dimensional Dirac line node in ZrSiS. *Nature Communications* **7**, 11696 (2016).

[170] Neupane, M. *et al.* Observation of topological nodal fermion semimetal phase in ZrSiS. *Physical Review B* **93**, 201104 (2016).

[171] Lv, Y.-Y. *et al.* Extremely large and significantly anisotropic magnetoresistance in ZrSiS single crystals. *Applied Physics Letters* **108**, 244101 (2016).

[172] Hu, J. *et al.* Evidence of topological nodal-line fermions in ZrSiSe and ZrSiTe. *Physical Review Letters* **117**, 016602 (2016).

[173] Wang, X. *et al.* Evidence of both surface and bulk Dirac bands and anisotropic nonsaturating magnetoresistance in ZrSiS. *Advanced Electronic Materials* **2**, 1600228 (2016).

[174] Ali, M. N. *et al.* Butterfly magnetoresistance, quasi-2D Dirac Fermi surface and topological phase transition in ZrSiS. *Science Advances* **2**, e1601742 (2016).

[175] Hu, J. *et al.* Nearly massless Dirac fermions and strong Zeeman splitting in the nodal-line semimetal ZrSiS probed by de Haas–van Alphen quantum oscillations. *Physical Review B* **96**, 045127 (2017).

[176] Singha, R., Pariari, A. K., Satpati, B. & Mandal, P. Large nonsaturating magnetoresistance and signature of nondegenerate Dirac nodes in ZrSiS. *Proceedings of the National Academy of Sciences* **114**, 2468–2473 (2017).

[177] Pezzini, S. *et al.* Unconventional mass enhancement around the Dirac nodal loop in ZrSiS. *Nature Physics* **14**, 178 (2018).

[178] Topp, A. *et al.* Surface floating 2D bands in layered nonsymmorphic semimetals: ZrSiS and related compounds. *Physical Review X* **7**, 041073 (2017).

[179] Sankar, R. *et al.* Crystal growth of Dirac semimetal ZrSiS with high magnetoresistance and mobility. *Scientific Reports* **7** (2017).

[180] Takane, D. *et al.* Dirac-node arc in the topological line-node semimetal HfSiS. *Physical Review B* **94**, 121108 (2016).

[181] Cacho, C. M. *et al.* Absolute spin calibration of an electron spin polarimeter by spin-resolved photoemission from the Au(111) surface states. *Review of Scientific Instruments* **80**, 043904 (2009).

[182] Steiner, S., Khmelevskyi, S., Marsmann, M. & Kresse, G. Calculation of the magnetic anisotropy with projected-augmented-wave methodology and the case study of disordered $Fe_{1-x}Co_x$ alloys. *Physical Review B* **93**, 224425 (2016).

[183] Adams, E. N. Magnetic susceptibility of a diamagnetic electron gas—the role of small effective electron mass. *Physical Review* **89**, 633–648 (1953).

[184] Arpiainen, V. & Lindroos, M. Effect of symmetry distortions on photoelectron selection rules and spectra of $Bi_2Sr_2CaCu_2O_{8+\delta}$. *Physical Review Letters* **97**, 037601 (2006).

[185] Hahn, T. International tables for crystallography, vol. A: Space-group symmetry (2005).

[186] Park, S. R., Kim, C. H., Yu, J., Han, J. H. & Kim, C. Orbital-angular-momentum based origin of Rashba-type surface band splitting. *Physical Review Letters* **107**, 156803 (2011).

[187] Kim, B. *et al.* Microscopic mechanism for asymmetric charge distribution in Rashba-type surface states and the origin of the energy splitting scale. *Physical Review B* **88**, 205408 (2013).

[188] Sunko, V. *et al.* Maximal Rashba-like spin splitting via kinetic-energy-coupled inversion-symmetry breaking. *Nature* **549**, 492–496 (2017).

[189] Wittel, K. & Manne, R. Atomic spin-orbit interaction parameters from spectral data for 19 elements. *Theoretica chimica acta* **33**, 347–349 (1974).

[190] Soluyanov, A. A. *et al.* Type-II Weyl semimetals. *Nature* **527**, 495–498 (2015).

[191] Schindler, F. *et al.* Higher-order topological insulators. *Science Advances* **4**, eaat0346 (2018).

[192] Benalcazar, W. A., Bernevig, B. A. & Hughes, T. L. Quantized electric multipole insulators. *Science* **357**, 61–66 (2017).

[193] Song, Z., Fang, Z. & Fang, C. (*d*-2) - dimensional edge states of rotation symmetry protected topological states. *Physical Review Letters* **119**, 246402 (2017).

[194] Greene, L. H., Thompson, J. & Schmalian, J. Strongly correlated electron systems—reports on the progress of the field. *Reports on Progress in Physics* **80**, 030401 (2017).

[195] Fulde, P., Thalmeier, P. & Zwicknagl, G. Strongly correlated electrons. *arXiv:cond-mat/0607165* (2006).

[196] Ramirez, A. P. Colossal magnetoresistance. *Journal of Physics: Condensed Matter* **9**, 8171–8199 (1997).

[197] Stewart, G. R. Heavy-fermion systems. *Reviews of Modern Physics* **56**, 755–787 (1984).

[198] Si, Q. & Steglich, F. Heavy fermions and quantum phase transitions. *Science* **329**, 1161–1166 (2010).

[199] de' Medici, L. Hund's metals, explained. *arXiv:1707.03282 [cond-mat]* (2017).

[200] Ruddlesden, S. N. & Popper, P. New compounds of the K_2NiF_4 type. *Acta Crystallographica* **10**, 538–539 (1957).

[201] Ruddlesden, S. N. & Popper, P. The compound $Ca_3Ti_2O_7$ and its structure. *Acta Crystallographica* **11**, 54–55 (1958).

[202] Sharma, I. B. & Singh, D. Solid state chemistry of Ruddlesden-Popper type complex oxides. *Bulletin of Materials Science* **21**, 363–374 (1998).

[203] Brese, N. E. & O'Keeffe, M. Bond-valence parameters for solids. *Acta Crystallographica Section B Structural Science* **47**, 192–197 (1991).

[204] O'Keeffe, M. The bond valence method in crystal chemistry. In Parthé, E. (ed.) *Modern Perspectives in Inorganic Crystal Chemistry*, 163–175 (Springer, 1992).

[205] Brown, I. D. Modelling the structures of La_2NiO_4. *Zeitschrift für Kristallographie - Crystalline Materials* **199**, 255–272 (1992).

[206] Johnsson, M. & Lemmens, P. Crystallography and chemistry of perovskites. *arXiv:cond-mat/0506606* (2005).

[207] Glazer, A. M. The classification of tilted octahedra in perovskites. *Acta Crystallographica Section B* **28**, 3384–3392 (1972).

[208] Jahn, H. A., Teller, E. & Donnan, F. G. Stability of polyatomic molecules in degenerate electronic states I—Orbital degeneracy. *Proceedings of the Royal Society of London. Series A - Mathematical and Physical Sciences* **161**, 220–235 (1937).

[209] Jahn, H. A. & Bragg, W. H. Stability of polyatomic molecules in degenerate electronic states II-Spin degeneracy. *Proceedings of the Royal Society of London. Series A - Mathematical and Physical Sciences* **164**, 117–131 (1938).

[210] Pavarini, E., Koch, E., Anders, F. & Jarrell, M. Crystal-field theory, tight-binding method and Jahn-Teller effect. In *Correlated Electrons: From Models to Materials*, vol. 2 - Modeling and Simulation (Forschunszentrum Jülich, 2012).

[211] Cohen, R. E. Origin of ferroelectricity in perovskites: The principal problems from a theoretical perspective. *Ferroelectrics* **150**, 1–12 (1993).

[212] Benedek, N. A., Rondinelli, J. M., Djani, H., Ghosez, P. & Lightfoot, P. Understanding ferroelectricity in layered perovskites: New ideas and insights from theory and experiments. *Dalton transactions* **44**, 10543–10558 (2015).

[213] Sigrist, M. Ruthenates: Unconventional superconductivity and magnetic properties. In Hewson, A. C. & Zlatić, V. (eds.) *Concepts in Electron Correlation*, 27–34 (Springer Netherlands, 2003).

[214] Maeno, Y. *et al.* Superconductivity in a layered perovskite without copper. *Nature* **372**, 532–534 (1994).

[215] Williams, T., Lichtenberg, F., Reller, A. & Bednorz, G. New layered perovskites in the Sr-Ru-O system: A transmission electron microscope study. *Materials Research Bulletin* **26**, 763–770 (1991).

[216] Braden, M., André, G., Nakatsuji, S. & Maeno, Y. Crystal and magnetic structure of Ca_2RuO_4: Magnetoelastic coupling and the metal-insulator transition. *Physical Review B* **58**, 847–861 (1998).

[217] Yoshida, Y. *et al.* Crystal and magnetic structure of $Ca_3Ru_2O_7$. *Physical Review B* **72**, 054412 (2005).

[218] Koster, G. *et al.* Structure, physical properties, and applications of SrRuO$_3$ thin films. *Reviews of Modern Physics* **84**, 253–298 (2012).

[219] Capogna, L. *et al.* Sensitivity to disorder of the metallic state in the ruthenates. *Physical Review Letters* **88**, 076602 (2002).

[220] Mackenzie, A. P. & Maeno, Y. The superconductivity of Sr$_2$RuO$_4$ and the physics of spin-triplet pairing. *Reviews of Modern Physics* **75**, 657–712 (2003).

[221] Bergemann, C., Mackenzie, A. P., Julian, S. R., Forsythe, D. & Ohmichi, E. Quasi-two-dimensional Fermi liquid properties of the unconventional superconductor Sr$_2$RuO$_4$. *Advances in Physics* **52**, 639–725 (2003).

[222] Mackenzie, A. P., Scaffidi, T., Hicks, C. W. & Maeno, Y. Even odder after twenty-three years: The superconducting order parameter puzzle of Sr$_2$RuO$_4$. *npj Quantum Materials* **2**, 1–9 (2017).

[223] Grigera, S. A. *et al.* Magnetic field-tuned quantum criticality in the metallic ruthenate Sr$_3$Ru$_2$O$_7$. *Science* **294**, 329–332 (2001).

[224] Fradkin, E., Kivelson, S. A., Lawler, M. J., Eisenstein, J. P. & Mackenzie, A. P. Nematic Fermi fluids in condensed matter physics. *Annual Review of Condensed Matter Physics* **1**, 153–178 (2010).

[225] Nakatsuji, S., Ikeda, S.-I. & Maeno, Y. Ca$_2$RuO$_4$: New Mott insulators of layered ruthenate. *Journal of the Physical Society of Japan* **66**, 1868–1871 (1997).

[226] Gorelov, E. *et al.* Nature of the Mott transition in Ca$_2$RuO$_4$. *Physical Review Letters* **104**, 226401 (2010).

[227] Sutter, D. *et al.* Hallmarks of Hunds coupling in the Mott insulator Ca$_3$Ru$_2$O$_7$. *Nature Communications* **8**, 15176 (2017).

[228] Sow, C. *et al.* Current-induced strong diamagnetism in the Mott insulator Ca$_2$RuO$_4$. *Science* **358**, 1084–1087 (2017).

[229] Miller, S. C. & Love, W. F. *Tables of irreducible representations of space groups and co-representations of magnetic space groups* (Pruett Press, 1967).

[230] Benedek, N. A. & Fennie, C. J. Hybrid improper ferroelectricity: A mechanism for controllable polarization-magnetization coupling. *Physical Review Letters* **106**, 107204 (2011).

[231] Nowadnick, E. A. & Fennie, C. J. Domains and ferroelectric switching pathways in $Ca_3Ti_2O_7$ from first principles. *Physical Review B* **94**, 104105 (2016).

[232] Harris, A. B. Symmetry analysis for the Ruddlesden-Popper systems $Ca_3Mn_2O_7$ and $Ca_3Ti_2O_7$. *Physical Review B* **84**, 064116 (2011).

[233] Campbell, B. J., Stokes, H. T., Tanner, D. E. & Hatch, D. M. ISODIS-PLACE: a web-based tool for exploring structural distortions. *Journal of Applied Crystallography* **39**, 607–614 (2006).

[234] Anderson, P. W. & Blount, E. I. Symmetry considerations on martensitic transformations: "Ferroelectric" metals? *Physical Review Letters* **14**, 217–219 (1965).

[235] Shi, Y. *et al.* A ferroelectric-like structural transition in a metal. *Nature Materials* **12**, 1024–1027 (2013).

[236] Puggioni, D. & Rondinelli, J. M. Designing a robustly metallic noncenstrosymmetric ruthenate oxide with large thermopower anisotropy. *Nature Communications* **5**, 1–9 (2014).

[237] Benedek, N. A. & Birol, T. 'Ferroelectric' metals reexamined: fundamental mechanisms and design considerations for new materials. *Journal of Materials Chemistry C* **4**, 4000–4015 (2016).

[238] Kim, T. H. *et al.* Polar metals by geometric design. *Nature* **533**, 68–72 (2016).

[239] Laurita, N. J. *et al.* Evidence for the weakly coupled electron mechanism in an Anderson-Blount polar metal. *Nature Communications* **10**, 1–7 (2019).

[240] Lobanov, M. V. *et al.* Crystal and magnetic structure of the $Ca_3Mn_2O_7$ Ruddlesden–Popper phase: neutron and synchrotron x-ray diffraction study. *Journal of Physics: Condensed Matter* **16**, 5339–5348 (2004).

[241] McCall, S., Cao, G. & Crow, J. E. Impact of magnetic fields on anisotropy in $Ca_3Ru_2O_7$. *Physical Review B* **67**, 094427 (2003).

[242] Bao, W., Mao, Z. Q., Qu, Z. & Lynn, J. W. Spin valve effect and magnetoresistivity in single crystalline $Ca_3Ru_2O_7$. *Physical Review Letters* **100**, 247203 (2008).

[243] Sokolov, D. A. *et al.* Metamagnetic texture in a polar antiferromagnet. *Nature Physics* **15**, 671–677 (2019).

[244] Aroyo, M. I. *et al.* Crystallography online: Bilbao crystallographic server. *Bulgarian Chemical Communications* **43**, 183–197 (2011).

[245] Blundell, S. *Magnetism in Condensed Matter* (Oxford University Press, 2001).

[246] Steffens, P. C. Magnetism in layered ruthenates (2008).

[247] Cao, G. *et al.* Orbitally driven behaviour: Mott transition, quantum oscillations and colossal magnetoresistance in bilayered $Ca_3Ru_2O_7$. *New Journal of Physics* **6**, 159–159 (2004).

[248] Cao, G., McCall, S., Crow, J. E. & Guertin, R. P. Observation of a metallic antiferromagnetic phase and metal to nonmetal transition in $Ca_3Ru_2O_7$. *Physical Review Letters* **78**, 1751–1754 (1997).

[249] Cao, G., Balicas, L., Xin, Y., Crow, J. E. & Nelson, C. S. Quantum oscillations, colossal magnetoresistance, and the magnetoelastic interaction in bilayered $Ca_3Ru_2O_7$. *Physical Review B* **67**, 184405 (2003).

[250] Ohmichi, E., Yoshida, Y., Ikeda, S.-I., Shirakawa, N. & Osada, T. Colossal magnetoresistance accompanying a structural transition in a highly two-dimensional metallic state of $Ca_3Ru_2O_7$. *Physical Review B* **70**, 104414 (2004).

[251] Yoshida, Y. *et al.* Quasi-two-dimensional metallic ground state of $Ca_3Ru_2O_7$. *Physical Review B* **69**, 220411 (2004).

[252] Kikugawa, N., Rost, A. W., Hicks, C. W., Schofield, A. J. & Mackenzie, A. P. $Ca_3Ru_2O_7$: Density wave formation and quantum oscillations in the Hall resistivity **79**, 024704 (2010).

[253] Zaanen, J. Why the temperature is high. *Nature* **430**, 512–513 (2004).

[254] Cooper, R. A. *et al.* Anomalous criticality in the electrical resistivity of $La_{2-x}Sr_xCuO_4$. *Science* **323**, 603–607 (2009).

[255] Bruin, J. A. N., Sakai, H., Perry, R. S. & Mackenzie, A. P. Similarity of scattering rates in metals showing T-linear resistivity. *Science* **339**, 804–807 (2013).

[256] Yoshida, Y., Ikeda, S.-I. & Shirakawa, N. Hall effect in $Ca_3Ru_2O_7$. *Journal of the Physical Society of Japan* **76**, 085002 (2007).

[257] Snow, C. S. *et al.* Pressure-tuned collapse of the Mott-like state in $Ca_{n+1}Ru_nO_{3n+1}$ (n=1,2): Raman spectroscopic studies. *Physical Review Letters* **89**, 226401 (2002).

[258] Liu, G.-Q. Mott transition and magnetic anisotropy in $Ca_3Ru_2O_7$. *Physical Review B* **84**, 235137 (2011).

[259] Thöle, F. & Spaldin, N. A. Magnetoelectric multipoles in metals. *Philosophical Transactions of the Royal Society A: Mathematical, Physical and Engineering Sciences* **376**, 20170450 (2018).

[260] Baumberger, F. *et al.* Nested Fermi surface and electronic instability in $Ca_3Ru_2O_7$. *Physical Review Letters* **96** (2006).

[261] Xing, H. *et al.* Existence of electron and hole pockets and partial gap opening in the correlated semimetal $Ca_3Ru_2O_7$. *Physical Review B* **97** (2018).

[262] Yuan, Y. *et al.* Ultrafast quasiparticle dynamics in correlated semimetal $Ca_3Ru_2O_7$. *arXiv:1901.02512 [cond-mat]* (2019).

[263] Horio, M. *et al.* Electron-driven C_2-symmetric Dirac semimetal uncovered in $Ca_3Ru_2O_7$. *arXiv:1911.12163 [cond-mat]* (2019).

[264] Perry, R. S. & Maeno, Y. Systematic approach to the growth of high-quality single crystals of $Sr_3Ru_2O_7$. *Journal of Crystal Growth* **271**, 134–141 (2004).

[265] Kikugawa, N. *et al.* $Ca_3Ru_2O_7$: Electronic instability and extremely strong quasiparticle renormalisation. *Journal of Magnetism and Magnetic Materials* **310**, 1027–1029 (2007).

[266] Lei, S. *et al.* Observation of quasi-two-dimensional polar domains and ferroelastic switching in a metal, $Ca_3Ru_2O_7$. *Nano Letters* **18**, 3088–3095 (2018).

[267] Singh, D. J. & Auluck, S. Electronic structure and bulk spin-valve behavior in $Ca_3Ru_2O_7$. *Physical Review Letters* **96** (2006).

[268] Acharya, S. *et al.* Evening out the spin and charge parity to increase T_C in Sr_2RuO_4. *Communications Physics* **2**, 1–8 (2019).

[269] Cao, G. *et al.* Tunneling magnetoresistance and quantum oscillations in bilayered $Ca_3Ru_2O_7$. *Physical Review B* **67**, 060406 (2003).

[270] Liebsch, A. & Ishida, H. Subband filling and Mott transition in $Ca_{2-x}Sr_xRuO_4$. *Physical Review Letters* **98**, 216403 (2007).